

UNIVERSITY OF OKLAHOMA
GRADUATE COLLEGE

INVESTIGATION OF POLYURETHANE SHAPE MEMORY POLYMER FOR
POTENTIAL APPLICATIONS IN BRAIN ANEURYSM TREATMENT

A THESIS

SUBMITTED TO THE GRADUATE FACULTY

In partial fulfillment of the requirements for the

Degree of

MASTER OF SCIENCE

By

ROBERT PAUL KUNKEL
Norman, Oklahoma
2019

INVESTIGATION OF POLYURETHANE SHAPE MEMORY POLYMER FOR
POTENTIAL APPLICATIONS IN BRAIN ANEURYSM TREATMENT

A THESIS APPROVED FOR THE
SCHOOL OF AEROSPACE AND MECHANICAL ENGINEERING

BY

Dr. Chung-Hao Lee, Chair

Dr. Yingtao Liu

Dr. Ramkumar Parthasarathy

© Copyright by ROBERT PAUL KUNKEL 2019
All Rights Reserved.

Dedications

I dedicate this thesis to my girlfriend, Christiane Phillips, who rejoiced with me in my successes and comforted me in my failures. Also, to my family, who have never stopped believing in me and will forever be my greatest source of motivation.

In loving memory of Robert Hyde, a scientist in the true sense of the word. – 73

Table of Contents

Dedications	iv
Table of Contents	v
List of Figures	xi
List of Tables	xix
Acknowledgements.....	xx
Abstract of the Thesis	xxi
CHAPTER 1: Introduction	1
1.1 Motivation.....	1
1.2 Objective and Scope.....	2
CHAPTER 2: Literature Review	7
2.1 Intracranial Aneurysms – An Overview.....	7
2.1.1 Intracranial Aneurysm Prevalence and Epidemiology	7
2.1.2 Growth Mechanisms of Intracranial Aneurysms.....	11
2.2 Clinical Treatments for ICAs – Advantages and Shortcomings	14
2.2.1 Surgical Clip Ligation	15
2.2.2 Endovascular Coil Embolization	17
2.3 Shape Memory Materials – Types and Functions.....	21
2.3.1 Shape Memory Alloys	21
2.3.2 Shape Memory Polymers.....	22

2.3.4 Shape Memory Polymer Foams	25
2.5 Shape Memory Polymers – Applications in Medicine.....	29
2.5.1 Treatment of Ischemic Stroke.....	30
2.5.2 Self-Deploying Stents.....	32
2.5.3 Aneurysm Treatment and Vessel Occlusion	33
CHAPTER 3: Pristine Shape Memory Polymer Synthesis and Characterization	38
3.1 Introduction	38
3.2 Methods.....	41
3.2.1 Materials and SMP synthesis.....	41
3.2.2 SMP synthesis procedure.....	42
3.2.3 Thermomechanical Characterization of the synthesized SMPs	45
Dynamic mechanical analysis (DMA)	45
Thermogravimetric analysis (TGA) and differential scanning calorimetry (DSC)...	45
3.2.4 Mechanical testing for the synthesized SMPs	46
3.2.5 Quantification of shape recovery capability.....	48
3.3 Results	48
3.3.1 DMA results	48
3.3.2 TGA results.....	49
3.3.3 DSC results.....	51
3.3.4 Uniaxial tensile testing results	52

3.3.5 Shape recovery capability.....	56
3.4 Discussion	58
3.4.1 Overall findings and relevance to endovascular embolization treatment for ICAs.....	58
3.4.2 Study limitations.....	61
3.5 Concluding Remarks	63
CHAPTER 4: Shape Memory Polymer Foam Synthesis and Characterization	65
4.1 Introduction	65
4.2 Materials and Methods	69
4.2.1. Materials	69
4.2.2. Preparation of solid and porous SMP materials	69
4.2.3. Shape Recovery Characterization.....	71
4.2.4 Investigations of Microstructural Morphology.....	71
4.2.5 Electrical Resistance Deployment Investigation	73
4.3 Results and Discussions	75
4.3.1 Shape memory and recovery features of the synthesized SMPs	75
4.3.2 Microstructural analysis	77
4.3.3 Electrical resistance heating-based SMP triggering method	79
4.3.4 Mechanical characterization of SMP foam under compressive load	82
4.4 Concluding Remarks and Study Limitations	84

CHAPTER 5: Additive Manufacturing Using Polyurethane Shape Memory Polymers ..	88
5.1 Introduction	88
5.2 Materials and Methods	95
5.2.1 SMP Synthesis and Composition Selection.....	95
5.2.2 Pre-Cure Hand Extrusion Testing.....	96
5.2.3 Pre-Cure Hand Extrusion Testing – Salt Inclusion	97
5.2.4 Rapid Cure Testing.....	98
5.2.5 Printer Design and Construction.....	99
5.2.6 SMP Printing Procedures.....	101
5.2.7 Extrusion Volume Calibration.....	101
5.3 Results and Discussion.....	103
5.3.1 Pre-Cure Hand Extrusion Testing.....	103
5.3.2 Pre-Cure Hand Extrusion Testing – Salt Inclusion	105
5.3.3 Rapid Cure Testing.....	107
5.3.4 Extrusion Volume Calibration.....	109
5.3.5 Printing Parameter Refinement	109
5.4 Concluding Remarks	112
5.4.1 Summary of Findings	112
5.4.2 Future Extensions	113
CHAPTER 6: Conclusions and Future Studies	114

6.1 Summary of Findings	114
6.2 Future Investigations	116
6.2.1 Investigate the biocompatibility of solid SMP and SMP foam materials. 116	
6.2.2 Identify a suitable SMP triggering mechanism and evaluate its efficacy. 117	
6.2.3 Design a micro-catheter delivery system that incorporates a shape recovery triggering mechanism for SMP deployment.....	117
6.2.4 Develop an in-vitro testing environment to evaluate device performance in a simulated aneurysm	118
6.2.5 Develop and validate a computational simulation framework for blood flow within an aneurysm to aid in device design.....	121
Appendix 1: SMP Foam Synthesis Procedures	123
A1.1 System Setup	123
A1.2 SMP Synthesis.....	124
A1.3 Casting a solid sugar block.....	127
A1.4 Solid SMP Casting (For thermo-mechanical testing).....	128
A1.5 SMP Foam Casting (Sugar Block)	130
A1.6 SMP Foam Casting (Loose Sugar).....	133
Appendix 2: Standard Operating Procedures for Prototype SMP 3D Printer.....	136
A2.1 Preparing the 3D Printer.....	136
Leveling the Bed.....	136

Heating the Bed	137
Loading and Verifying the G-Code	137
A2.2 Preparing the LVE.....	138
LVE Geometry	138
Assembly	140
A2.3 SMP Synthesis.....	141
A2.4 Printing	141
Loading the LVE	141
Starting the Print	142
Verifying Proper Printing	142
A2.5 Removing the Print.....	143
A2.6 Preparing for Another Print.....	144
Printer Cleaning.....	144
References.....	145

List of Figures

Figure 2.1: Progression of an intracranial aneurysm from initiation to rupture [11].....	8
Figure 2.2: a) Saccular vs. b) fusiform aneurysm general geometries. Image courtesy of: https://www.bcm.edu/healthcare/care-centers/neurosurgery/conditions/brain-aneurysms	9
Figure 2.3: Schematic of the Circle of Willis illustrating some of the most common aneurysm initiation sites. Image courtesy of:	10
Figure 2.4: a) One fusiform and b) one saccular aneurysm showing highly varying wall shear stress values. (1) Indicates growth in an area of low wall shear stress, (2) identifies a secondary aneurysm, or bleb, forming in an area of high wall shear stress while the main aneurysm (3) exhibits low wall shear stress [12].	13
Figure 2.5: Angiographic view before and after treatment of an intracranial aneurysm using surgical clip ligation [20].	16
Figure 2.6: (1) Guide catheter is in place, and micro-catheter positions the tip of the coils in the aneurysm sac. (2) Coils are fed into the aneurysm sac. (3) Coil placement continues and a balloon is inflated to prevent coil migration into the parent artery. (4) The coils successfully occlude the saccular aneurysm. Images courtesy of Mentice:	18
Figure 2.7: The modified Raymond-Roy occlusion scale, which includes two subdivisions of Class III as proposed by Mascitelli <i>et al.</i> (2015) [24].	20
Figure 2.8: The cyclic changes in crystalline state that drive shape recovery in SMAs [27].	22

Figure 2.9: A graphical representation of the shape recovery behavior exhibited by SMPs.	23
Figure 2.10: Demonstration of multiple shape memory behavior associated with discrete temperature thresholds. The green plot shows three distinct deformations that take place at three distinct temperatures (represented in blue). The polymer recovers each deformation when heated to the temperature at which the deformation occurred [29]......	24
Figure 2.11: Microscopic images of an ultra-low-density polyurethane SMP foam synthesized using chemical blowing techniques [30]......	26
Figure 2.12: Particle leaching procedures. Visualization inspired by Janik <i>et al.</i> (2015) [31]......	27
Figure 2.13: Thermally-induced phase separation (TIPS) procedures. Visualization inspired by Janik <i>et al.</i> (2015) [31]......	28
Figure 2.14: Emulsion freeze-drying procedure. Visualization inspired by Janik <i>et al.</i> (2015) [31].	29
Figure 2.15: The thrombectomy device designed by Metzger <i>et al.</i> (2002) in a) its deformed configuration and b) its coiled home configuration [4]......	31
Figure 2.16: Thrombectomy device designed by Small <i>et al.</i> (2007): (a) shown in its home configuration, and (b) magnified to show nitinol coils [5].	32
Figure 2.17: SMP foam-coated coils designed by Boyle <i>et al.</i> (2017): A) before compression, B) after compression, and C) after immersion in warm water (37 °C) for 30 minutes [46]......	34

Figure 2.18: Results from *in vivo* porcine studies using aliphatic SMP foam (B.0) response after 30 minutes of implantation, (B.30) response and partial endothelialization after 30 days of implantation, and (B.90) total endothelialization after 90 days of implantation [35]..... 35

Figure 2.19: Laser-deployed SMP foam embolization device designed by Maitland *et al.* (2007): (a) uncompressed SMP foam sphere, (b) box indicates light diffuser tip, below is the compressed SMP foam crimped around the light diffuser, and (c) heated crimping device used for SMP compression [47]. 36

Figure 2.20: Resistively heated SMP foam embolization device designed by Hwang *et al.* (2013): (a) undeformed SMP spheres, (b) crimped SMP devices, top containing tungsten particles for visibility, and (c) schematic diagram of heating element [49] 37

Figure 3.1: (a) Top-view schematic of the in-house equipment used in the shape memory polymer synthesis. (b) An illustration of the synthesis procedure showing specifically (i) the measurement of each monomer, (ii) the mixture of monomers to form the polymer, (iii) the deposition of the mixture into previously cast molds, and (iv) the curing of the mixture in a vacuum oven..... 42

Figure 3.2: (a) Shear storage modulus of all the twelve SMP compositions as directly measured from the DMA tests, and (b) $\tan(\delta)$ curves as derived from the DMA testing results for determining the T_g of each SMP composition..... 49

Figure 3.3: TGA results showing the decomposition of the SMP with increasing temperature. 50

Figure 3.4: DSC results used for determinations of the T_g for each SMP composition. . 51

Figure 3.5: Mean \pm SEM of the failure stress (blue filled squares) and failure strain (red filled circles) for all the twelve SMP compositions (n=2) under uniaxial tension testing ($T_g + 10$ °C). 53

Figure 3.6: Representative cyclic mechanical testing results (SMP3) when tested at 50% of the observed failure strain ($T_g + 10$ °C) showing: (a) the relaxation trend in the peak stress with an increasing number of cycles, (b) the increase in the cumulative stress reduction and (c) the convergence of the elastic modulus with an increasing number of cycles. 55

Figure 3.7: Mean \pm SEM of the recovery testing time for a representative SMP composition (SMP3, n=3) showing the consistent trend of reduced recovery time with an increased temperature. 57

Figure 3.8: Experimental photos of the recovery testing for three representative SMP compositions (SMP3, SMP7, and SMP11) at defined time increments ($t = 0$ sec, $t = 2$ sec, $t = 4$ sec, and $t = 6$ sec), showing the observed trend of a decreasing recovery time with an increasing TEA content..... 58

Figure 4.1: Schematic of the sugar particle leaching method for fabrication of the porous SMP foam. 71

Figure 4.2: (a) Experimental photo of the electrically heated procedure to activate the shape recovery of the SMP foam using carbon fiber wires. (2) Image of the experimental setup in thermal chamber for mechanical characterization of the SMP foam. 74

Figure 4.3: Progression of the shape recovery process of the compressed porous SMP foam in response to direct heating above the SMP's T_g 76

Figure 4.4: Shape recovery of the bent solid SMP beam (temporary shape) into the originally programmed straight shape after heating above the SMP's T_g 76

Figure 4.5: SEM images taken from the top layer and the middle layer of the porous SMP foam fabricated using the sugar particle leaching method, showing the open-cell structure of the foam. 78

Figure 4.6: μ -CT images showing the microstructure of SMP foam: (a) 2D image slices on orthogonal planes, (b) zoomed-in area of the 2D image slice on the x - y plane, demonstrating the typical pore sizes of the SMP foam, and (c) the visualization of the reconstructed 3D geometry of the cubic SMP foam (10 mm by 10 mm by 10 mm). 79

Figure 4.7: Surface temperature of the SMP foam specimen at various applied electric current magnitudes during electrical resistance heating. 81

Figure 4.8: Experimental photos of the shape recovery process of the compressed SMP foam under 0.15 A DC, along with the measured surface temperature profile via an IR camera at 140 seconds after the applied electric current. 81

Figure 4.9: Mechanical characterization of the fabricated SMP foam under cyclic compressive load conditions: (a) typical mechanical response of the SMP foam at room temperature, (b) representative mechanical response of the SMP foam at T_g and $T_g + 10\text{ }^\circ\text{C}$ under cyclic compressive loading, and (c) comparison of the maximum stress at 35% strain for various loading cycles at T_g and $T_g + 10\text{ }^\circ\text{C}$. Values are reported as mean \pm SEM (standard error of the mean; $n=3$)..... 84

Figure 5.1: Schematic representation of an FDM 3D printer, as adapted from [120]. 90

Figure 5.2: Schematic representation of a bottom-up SLA printer. Image courtesy of Formlabs. https://formlabs.com/blog/ultimate-guide-to-stereolithography-sla-3d-printing/	91
Figure 5.3: Schematic representation of different DIW extrusion methods, as adapted from [123].....	92
Figure 5.4: Shape recovery demonstrations for fine-resolution SMP objects printed using a viscous oligomer melt and SLA techniques, as adapted from [124].....	93
Figure 5.5: Schematic representation of hand extrusion testing protocols. Image courtesy of Ryan Bodlak.	97
Figure 5.6: Schematic representation of rapid cure testing protocols. Image courtesy of Ryan Bodlak.....	99
Figure 5.7: Wiring diagram for a solid-state relay. In this scenario, the wall outlet is the power source, the input signal is received from the Creality temperature control board, and the load is the KEENOVO silicone heated bed. Image courtesy of:	100
Figure 5.8: CAD rendering of the prototype DIW printer (<i>left</i>), and photo of completed prototype DIW printer (<i>right</i>).	100
Figure 5.9: Flow chart representation of extrusion speed calibration process. Image courtesy of Ryan Bodlak.....	102
Figure 5.10: Hand extrusion testing results.	105
Figure 5.11: Hand extrusion - salt inclusion results. Samples shown were extruded at $t = 60$ minutes.....	107
Figure 5.12: a) Plot of cure time as a function of plate temperature, showing a sharp decrease in cure time which levels out near 150 °C. b) Numerical values for cure	

time as a function of plate temperature. c) SMP samples synthesized during rapid cure testing. Note that the SMP at 180 °C and 190 °C show yellowing due to prolonged exposure to high heat. Distance between long marks = 10 mm. 108

Figure 5.13: Comparison between an early SMP test print and a refined SMP test print. a) First successful test print using DIW printer, showing signs of un-calibrated extrusion speed and slow SMP curing. b) Later multi-layer SMP print with refined extrusion speed and proper cure temperature. 110

Figure 5.14: Messy print showcasing many persistent shortcomings of the printer. a) Inconsistency at the upper layers of the print and material slump are clear from a side view. b) Poor extrusion control (due to residual pressure after the extrusion ends) can be seen between these individual rings..... 111

Figure 6.1: First iteration of the PIV flow loop design, created from the Spring 2018 Capstone project..... 119

Figure 6.2: Schematic for the revised flow loop design, currently in development. 120

Figure A1.1: Workspace layout for SMP synthesis procedures. 123

Figure A1.2: Example of proper sugar crystal texture and adhesion..... 127

Figure A1.3: Finished sugar block..... 128

Figure A1.4: a) Beam specimens synthesized without the degassing procedure b) Dog bone specimens synthesized using the degassing procedure. 129

Figure A1.5: Cured SMP cast around a sugar scaffold in the shape of a weigh boat.... 131

Figure A1.6: Same SMP blocks from **Fig. A1.5** with all excess polymer trimmed away. 132

Figure A1.7: Same SMP block from Fig. A1.6 showing partial sugar dissolution. Note that the dark shading in the center indicates the presence of remaining sugar.	132
Figure A1.8: SMP molds filled with varying Sugar-to-SMP ratios.	133
Figure A1.9: Well-packed sugar/SMP mixture in a 1.5 x 1.5 x 0.4 in. mold.	134
Figure A2.1: Location of the SD card slot on the printer control box.	138
Figure A2.2: 3D model of the full LVE system.	139
Figure A2.3: LVE system (a) fully retracted and (b) fully extended.	140
Figure A2.4: Degraded SMP with a distinctive amber tint.	143

List of Tables

Table 3.1: Percent monomer content, monomer-mixture stirring time, and the curing heating rate for all the twelve SMP compositions.	41
Table 3.2: Glass transition temperature (T_g) and storage modulus from the DMA tests (cf. Fig. 3.2), T_g from the DSC tests (cf. Fig. 3.4), and the temperature levels associated with 90% and 50% remaining weights of the SMPs from the TGA tests (cf. Fig. 3.3).	52
Table 3.3: P-values from 1-way analysis of variance comparing SMP failure strain values (green shading indicates statistically significant).	53
Table 3.4: P-values from 1-way analysis of variance comparing SMP failure stress values (green shading indicates statistically significant).	54
Table 3.5: Failure stresses and failure strains from the uniaxial tensile failure testing (cf. Fig. 3.5) and the stress reductions and the calculated elastic modulus from the uniaxial cyclic tensile testing (cf. Fig. 3.6) for all the twelve SMP compositions. Tensile tests conducted at $T_g + 10$ °C.	56
Table 5.1: Hand extrusion testing - salt inclusion results. Red cells indicate an inability to extrude material.	106

Acknowledgements

This research was not a task that I could have accomplished alone. My mentor, Dr. Chung-Hao Lee dedicated countless hours educating me not only about my research topics, but also about navigating the academic world through participation in conferences and the preparation of manuscripts. Dr. Lee never wavered in his willingness to help me succeed in my pursuits, and rather than simply preparing me to earn a degree, he challenged me to grow in all aspects of my life. I also extend my sincere thanks to our collaborator Dr. Yingtao Liu, whose expertise in the field of materials science was critical to the success of our SMP investigations. Without the facilities, equipment, and procedures he so generously shared, most of this research would not have been completed. This recognition is also extended to Jingyu Wang, Jishan Luo, and Wenyuan Luo—Dr. Liu’s graduate students who were kind to share their experience and lab space with me during this study.

After spending more than two years in the Biomechanics and Biomaterials Design Lab (BBDL), my colleagues have become my family. Colton Ross, Ryan Bodlak, Wyatt Maney, Luke Whitney, and Robert Beem worked countless hours to bring the prototype SMP 3D printer to life as a part of the 2019 Spring Capstone. Devin Laurence and Samuel Jett, my fellow graduate students, walked beside me through every step of my research career and provided the best support network I could have ever asked for.

Abstract of the Thesis

INVESTIGATION OF POLYURETHANE SHAPE MEMORY POLYMER FOR
POTENTIAL APPLICATIONS IN BRAIN ANEURYSM TREATMENT

By

Robert Paul Kunkel

Master of Science in Mechanical Engineering

University of Oklahoma, 2019

Professor Chung-Hao Lee, Chair

The objective of this research is to investigate a variety of synthesis and manufacturing procedures for a polyurethane shape memory polymer (SMP) produced from the reaction of Hexamethylene Diisocyanate (HDI), N,N,N',N'-Tetrakis-2(Hydroxypropyl)ethylenediamine (HPED), and Triethanolamine (TEA), and monomers. The mechanical properties and shape memory behavior of each resulting material are presented in the context of their potential applications in the treatment of intracranial aneurysms via endovascular embolization.

In this thesis, different compositions of the polyurethane SMP are synthesized based on varying ratios between TEA and HPED monomers to create solid beams and dog bone samples. The resulting twelve compositions are mechanically characterized using uniaxial tensile loading with both failure and cyclic protocols to determine the materials' failure stress and strain, elastic modulus, and stress relaxation behavior. The thermomechanical properties of the twelve compositions are investigated using both differential scanning calorimetry (DSC) and dynamic mechanical analysis (DMA) to investigate the storage modulus, loss modulus, and glass transition temperature (T_g) of the materials. A single composition is selected based on its suitability for use in the design of an implantable medical device, and this composition is used by default in the following studies.

A sugar particle leaching method is used to synthesize the selected SMP composition in the form of an open-celled highly porous foam. The porosity and pore size of the foam are characterized using both scanning electron microscopy (SEM) and micro-computed tomography (μ -CT) imaging techniques. The mechanical properties of the foam are characterized using uniaxial cyclic compression both above and below the T_g of the material. Elastic modulus values above and below T_g are compared with similar SMP foam materials designed for use in the human body. The shape memory properties of the material are demonstrated, and a prototype deployment mechanism based on electrical resistance heating is employed to trigger shape recovery in a compressed foam sample.

The curing behavior of the polyurethane SMP material is observed and investigated, and this information is used to design and construct a prototype direct ink writing (DIW) 3D printer. The liquid pre-cure SMP mixture is shown to have a working

life approaching 150 minutes when kept at 40 °C and a rapid-curing time of less than 30 seconds when heated above 150 °C. The printer takes advantage of the rapid curing using a high-temperature build plate to solidify the liquid SMP after extrusion. Test prints are conducted, resulting in complex geometries that retain the characteristic shape recovery behavior of the SMP, validating the printing method. Advantages and disadvantages of the initial prototype device are identified, and recommendations are made for modifications to be included in the next iteration of the design.

The findings presented in this research encompass a diverse set of material fabrication techniques that can be used to tailor the mechanical and thermomechanical properties of this polyurethane SMP. By reporting the changes in mechanical properties and differences in structure that can be created using the above methods, this thesis lays the groundwork for future investigations into the design of an SMP-based endovascular aneurysm occlusion device.

CHAPTER 1: Introduction

1.1 Motivation

Intracranial aneurysms are deformations in the arteries of the brain that carry the potential to rupture, causing cranial bleeding, swelling, and stroke. Although the mechanisms by which aneurysms form, grow, and eventually rupture are still a hotly contested area of study, recent findings suggest that hemodynamics play a crucial role in this process. Because of this, most aneurysms treatments focus on preventing blood from leaving the parent artery and entering the aneurysm space. Current treatments include surgical clip ligation, which clamps the boundary between the aneurysm and the parent artery from the outside of the vessel, endovascular coil embolization, which fills the aneurysm with a mass of coils that promote clotting inside the aneurysm, and flow diversion stenting, which uses a fine mesh stent placed within the parent artery to direct blood flow away from the diseased area. Although these treatments are effective in their treatment of simple aneurysm geometries, giant aneurysms and aneurysms with complex geometries continue to present challenges including aneurysm recurrence, rupture during treatment, and difficulty of delivery.

In the field of medical device design, shape memory polymers (SMPs) have gained popularity thanks to their biocompatibility, reconfigurable geometries, and wide variety of obtainable mechanical properties. One area in particular where SMPs have gained traction is the design of scaffolds for tissue engineering. Multiple studies have investigated the cell adhesion properties of polyurethane SMP in the interest of developing active scaffold

materials [1-3]. Another area in which SMPs are showing promise is the field of endovascular surgery and implantation. The self-actuation behavior of SMPs allows for the creation of simple moving components for operations that take place at the end of a catheter that replace the need for small-scale actuators. One such application is the treatment of ischemic stroke, in which the SMP is used as a deployable anchor for dislodging thrombi [4, 5].

Another application that has captured the interest of the Biomechanics and Biomaterials Design Laboratory at the University of Oklahoma is a patient-specific aneurysm occlusion device. SMPs could help address the shortcomings of other endovascular aneurysm treatments by allowing the development of a deployable foam-like device modeled based on angiographic data from an aneurysm patient. In the proposed novel treatment, 3-dimensional patient's medical image data would be used to fabricate a foam device in the exact shape of a patient's aneurysm. The device would then be compressed around an activation device at the tip of a catheter and delivered in a manner similar to coil embolization. The activation device would stimulate shape recovery in the polymer and perfectly fill the aneurysm with an open-cell foam structure. Taking advantage of the same cell adhesion properties that make SMPs desirable for tissue engineering, the foam would promote healthy thrombus formation and eventually fill the aneurysm completely with a solid mass, preventing further rupture.

1.2 Objective and Scope

The objective of this research is to synthesize and characterize an aliphatic polyurethane SMP, then evaluate its potential for use in the design of a novel aneurysm

treatment device. We first focus on synthesizing the SMP in a solid form using the full range of monomer combinations available without fundamentally changing the nature of the polymer. We investigate the mechanical and thermomechanical properties of each polymer composition to assess the range of possible mechanical characteristics and operating temperatures for the aliphatic polyurethane. Based on this data, we select a single composition that we expect to perform best in the aneurysm treatment application and use it in the creation of an open cell foam by means of a sugar particle leaching procedure. We investigate the mechanical properties, pore structure, and shape memory properties of this foam and compare our results with other SMP foams that have been developed for medical applications. Finally, we develop an additive manufacturing technique that is compatible with this specific SMP, a task that is made difficult by the fact that the SMP is a thermoset polymer. The specific contributions presented as a part of this document are detailed as follows:

(1) Synthesis and Characterization of Solid Aliphatic Polyurethane SMPs

Twelve different SMP compositions have been synthesized based on the monomers Hexamethylene Diisocyanate (HDI), Triethanolamine (TEA), and N,N,N',N'-Tetrakis-2(Hydroxypropyl)ethylenediamine (HPED). By varying the amounts of HPED and TEA present in the SMP, we achieved glass transition temperature values (the threshold at which the shape memory effect is activated) that ranged from 33 °C to 87 °C. The shape memory effect was demonstrated in each of the synthesized polymers, and the mechanical properties of each polymer were characterized using uniaxial failure and cyclic testing protocols. We demonstrated that the SMP behaves as a rigid, glassy material below its T_g and becomes rubbery

and deformable when heated above its T_g . The polymer was observed to recover its shape within 1 minute of heating above T_g . This rapid recovery paired with the potential for a T_g situated between body temperature (37 °C) and the threshold for tissue damage (45 °C) suggests that this material had very good potential for applications in medical device design.

(2) Synthesis and Characterization of Aliphatic Polyurethane SMP Foams

An open-cell porous SMP foam has been synthesized using a sugar particle leaching procedure in combination with the synthesis procedures used to produce solid polyurethane SMP. To produce the foam, liquid SMP is poured over a compressed sugar scaffold and allowed to cure. After curing, the block is submerged in water and the gains of sugar dissolve to create uniform and interconnected pores. The pore size and open-cell structure are verified using μ -CT and SEM imaging. The mechanical properties of the material are investigated using uniaxial cyclic compression both above and below the transition temperature of the material. Compared to other SMP foams being developed for medical use, this foam possesses similar elastic modulus values both above and below T_g . Shape recovery behavior is demonstrated for this material both using exposure to ambient heat and using an internal electric heating element. The SMP foam shares the shape recovery characteristics demonstrated during solid SMP characterization but has a much higher compressibility and a much lower elastic modulus, making it well suited for aneurysm treatment, which requires significant material expansion in an easily damaged environment.

(3) Development of a Thermally-Curing Direct Ink Writing (DIW) 3D Printer for Use with Shape Memory Polyurethane Materials

A prototype DIW 3D printer has been constructed and tuned to produce prints up to 5 mm tall using polyurethane SMP material. The working life of the SMP has been determined and is used to inform the maximum length of print that can be produced. A rapid curing behavior has been identified for the polyurethane SMP, and the behavior has been implemented in the printing process to achieve total curing within 30 seconds of polymer deposition. A constant governing volume extrusion was identified and calibrated to accommodate the addition of a large volume syringe extruder in place of the stock filament extruder on a Creality CR-10s printer. A variety of test geometries have been produced using the prototype printer, and several shortcomings have been identified along with potential remedies. A height limit on printed objects has become apparent, as heat is unable to transfer reliably from the heated printing surface through a part taller than 5mm. A print time limit has been identified as a result of material working life studies and has been confirmed during testing prints. Strategies for avoiding these issues in future iterations of the device are discussed.

This thesis is organized as described below. Chapter 2 introduces intracranial aneurysms and gives an overview of the initiation, growth, and rupture of the pathology. Current clinical treatments for intracranial aneurysms are discussed along with their associated advantages and shortcomings. The shape memory effect is introduced and its variations in different kinds of materials are discussed. Different manufacturing techniques for shape memory polymers are introduced, and the applications of shape memory polymers in the

medical industry are evaluated. Chapter 3 provides detailed procedures for the synthesis of solid shape memory polymer using HDI, TEA, and HPED. The thermo-mechanical properties of the resulting materials are characterized and discussed. In Chapter 4, the procedures for synthesizing polyurethane SMP foam using a sugar scaffold are given. The mechanical properties of the foam are characterized and discussed, and a basic electrical resistance heating method is applied to trigger shape recovery. A variety of properties relating to the curing behavior of the SMP are investigated in Chapter 5, and a prototype 3D printer is constructed based on the results. The procedures for operating the printer and the mechanism by which objects are printed are discussed. Recommendations are made about future iterations of the printing device based on limitations observed during test prints. Chapter 6 presents conclusions from the body of work as a whole and discusses the future of the project as it moves toward the development of a novel medical device.

CHAPTER 2: Literature Review

2.1 Intracranial Aneurysms – An Overview

2.1.1 Intracranial Aneurysm Prevalence and Epidemiology

An intracranial aneurysm (ICA) is a focal dilation of one of the many arteries in the brain. The aneurysm often takes the form of a roughly spherical pocket protruding from the artery wall as illustrated in **Figure 2.1**, although the size and the shape of ICAs have been shown to vary greatly between patients [6, 7]. ICAs have a prevalence of roughly 2.3%, and are often asymptomatic for the majority of a patient's lifetime [7]. The most immediate danger that aneurysms present to a patient is their potential rupture. Depending on the size of the aneurysm, the likelihood of a rupture event can vary from 0.7% to 4.0% per year [7]. When an ICA ruptures, the artery begins releasing blood into the surrounding brain tissue, resulting in a condition known as *subarachnoid hemorrhage* (SAH). ICA rupture accounts for 80% of all the SAH cases not associated with cranial trauma, and SAH cases account for 5-8% of all strokes [8, 9]. SAH resulting from the rupture of an aneurysm is associated with a mortality rate approaching 40% within a week of the incident [10]. Due to the severe consequences of an ICA rupture, physicians and researchers have dedicated significant efforts to understanding the mechanisms that underly aneurysm formation, growth, and eventual rupture to prevent patients from ever reaching the point of SAH in the first place.

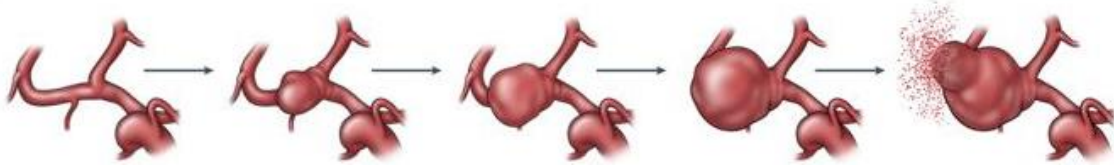


Figure 2.1: Progression of an intracranial aneurysm from initiation to rupture [11].

One factor that plays a large role in determining a physician’s ability to treat an aneurysm is the shape of the dilation and its location with respect to the parent artery and other surrounding structures. ICAs can be separated into two categories based on the way they grow in relation to their parent artery. The first category of ICA, known as a *saccular aneurysm*, is an ICA that extends from a single wall of the parent artery. As shown in **Figure 2.2a**, these aneurysms typically resemble a bud (the aneurysm) attached to a stem (the parent artery). This type of ICA is called “saccular” because the dilation forms a well-defined ‘sac’ region that is attached to the parent artery via a ‘neck’ region. Aneurysms of this type are typically described with respect to the width of their neck region and the height and width of the sac region.

The second type of ICA, known as a fusiform aneurysm, occurs when an ICA is distributed around the entire wall of the parent artery as seen in **Figure 2.2b**. In this case, there is rarely any sort of ‘neck’ region. Instead, the walls of the artery deform outward as if that section of the vessel was being inflated. Fusiform aneurysms are much less common than saccular aneurysms and are suspected to develop via different mechanisms. There is much less information about fusiform aneurysms since more than 80% of all aneurysms are saccular [12]. However, fusiform aneurysms present a significantly greater challenge

for treatment since the diseased area involves the entirety of the parent artery near the dilation rather than an offshoot on only one side.

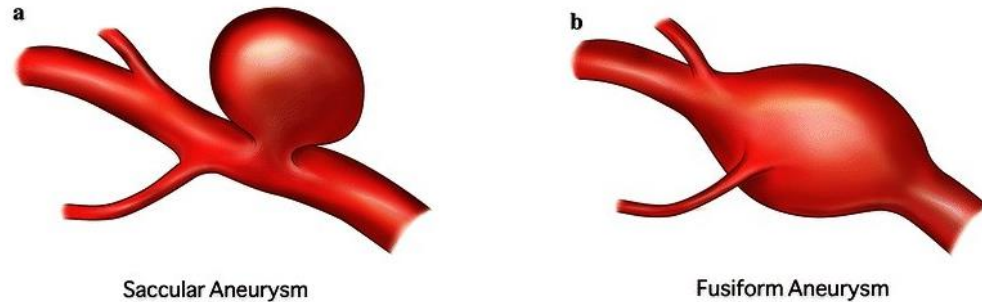


Figure 2.2: a) Saccular vs. b) fusiform aneurysm general geometries. Image courtesy of: <https://www.bcm.edu/healthcare/care-centers/neurosurgery/conditions/brain-aneurysms>.

ICAs are almost exclusively located in the Circle of Willis—a ring of highly interconnected arteries at the base of the brain [7]. As illustrated in **Figure 2.3**, this structure consists of the major arteries tasked with supplying blood to the rest of the brain, and it handles a high volume of blood flow through its multitude of branches. The location of ICAs within this structure is relatively evenly dispersed between four major artery groups. In the International Study of Unruptured Intracranial Aneurysms, one of the largest studies of the natural history and clinical treatment of intracranial aneurysms (4,060 aneurysms recorded), 29.0% of ICAs were located in the middle cerebral artery (n=1,179), 12.3% of ICAs were located in the anterior communicating or anterior cerebral artery (n=500), 38.2% of ICAs were located in the internal carotid artery (n=1,550), and 20.4% of ICAs were located in the posterior circulation region, which includes the vertebral arteries, basilar artery, and posterior communicating artery (n=828) [6].

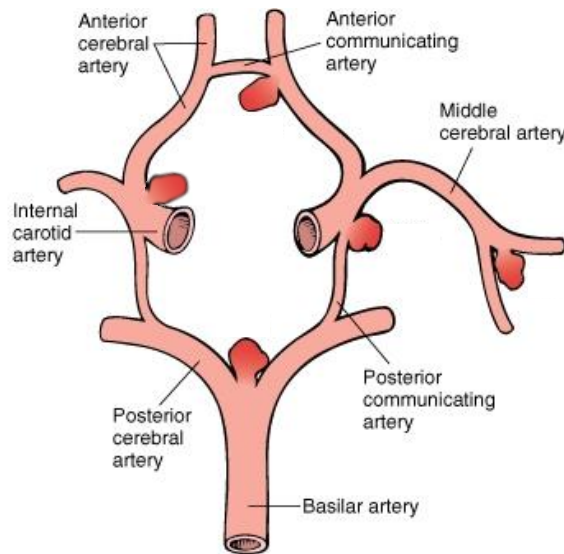


Figure 2.3: Schematic of the Circle of Willis illustrating some of the most common aneurysm initiation sites. Image courtesy of:

<https://www.grepmed.com/images/206/circleofwillis-epidemiology-frequency-location-aneurysm-anatomy-willis>.

The initiation of new intracranial aneurysms is a process that is still poorly understood. In the absence of a definitive initiation mechanism, many studies with the goal of identifying aneurysm risk factors have been conducted to help inform selective screening procedures and preventative treatments for at-risk patients. Factors that have shown a high correlation with aneurysm occurrence include a familial history of the ICAs and either the presence of autosomal dominant polycystic kidney disease (ADPKD) or a family history of ADPKD [8, 13-15].

Many studies have provided evidence that the formation of ICAs involves some sort of a genetic component. Angiographic screening of first-degree relatives of patients who suffered from SAH showed a prevalence of 4%, which is small but presents a marked

increase from the occurrence rate for the general population (2.3%) [7, 8]. The chance of aneurysm detection increases for individuals with two or more family members who have suffered from SAH. Angiographic screening from these individuals reveals an incidence of 9.2% [8]. Results from the International Study of Unruptured Intracranial Aneurysms showed that 18.3% of ICA patients had a family history of aneurysms, and 32.7% had a family history of stroke [6]. Although evidence suggests a genetic component to aneurysm formation, the mechanisms by which this component manifests are not fully understood, limiting all discussions about the inheritability of aneurysms to simple analyses of trends in the medical history of patients [13].

While the inherited propensity for ICAs is not well understood, researchers have uncovered a mechanism linking ADPKD to the formation of ICAs. The formations of lesions associated with ADPKD can be attributed to a deficiency of the PKD1 and PKD2 genes—proteins associated with maintenance of epithelial cells lining the vasculature surrounding the kidneys [8]. Trials utilizing mice with a reduced expression of PKD1 showed that a deficiency in the protein caused lesion formation not only within the kidneys of the mouse, but also in the aorta. The aortic aneurysms that formed in the deficient animal models resulted in death before the mice reached 2 weeks of age [15]. In human patients with both ADPKD and a family history of ICAs, the risk of aneurysm development reaches 16%, a major increase from the baseline risk in a healthy population [8].

2.1.2 Growth Mechanisms of Intracranial Aneurysms

After their initial formation, aneurysms grow and develop due to a combination of biological and mechanical stimuli. The primary mechanism of growth is thought to be a remodeling response regulated by the mechanical stresses on the vessel wall. More

specifically, the wall shear stress has been shown to have a profound effect on the growth and rupture risks of ICAs [12, 16]. The wall shear stress is a mechanical stimulus that can be easily studied with the use of computational fluid dynamics (CFD) simulations. The problem that arises from using wall shear stress to predict aneurysm development is that both high and low wall shear stress values can be tied to different types of aneurysm development, both of which lead to eventual rupture.

Studies have shown that wall shear stress values exceeding a certain threshold can elicit elastin loss, vessel wall thinning, and bulge formation, all of which are pathologies typically associated with early aneurysm development [12]. The sites at which many ICAs develop also suggest the role of the high wall shear stress in the early development of aneurysms. Regions with high incidence of ICA formation include bifurcations in arteries, bends and curves in vessels, and areas with a high volume flow rate [17]. All these areas share a natural propensity for high wall shear stresses. Additional studies in more developed aneurysms have shown that smaller dilations which stem from the main aneurysm sac known as blebs (**Fig. 2.4b**), are most likely to form in areas where the wall shear stress is the highest [16]. Abnormal mechanical stresses can trigger a tissue remodeling response through a process known as mechanotransduction. The exact mechanisms that guide this process are not well understood, but certain tissue responses can be reliably correlated with mechanical stresses. The tissue responses associated with the high wall shear stress in cerebral arteries include endothelial cell damage and turnover, extracellular matrix degradation, cell death, and tissue thinning in the artery wall [12].

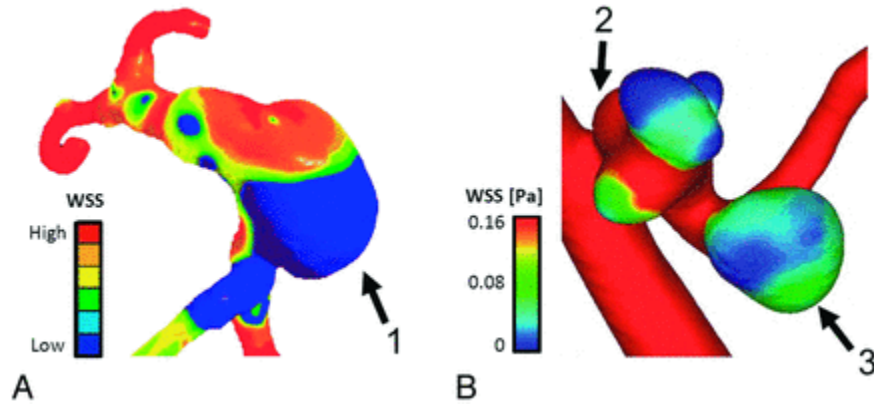


Figure 2.4: a) One fusiform and b) one saccular aneurysm showing highly varying wall shear stress values. (1) Indicates growth in an area of low wall shear stress, (2) identifies a secondary aneurysm, or bleb, forming in an area of high wall shear stress while the main aneurysm (3) exhibits low wall shear stress [12].

This information would likely suggest that the high stress is attributed to the ICA growth. However, developed aneurysms such as those in **Figure 2.4** have been shown to possess up to 3 times lower wall shear stresses in the sac region than those observed in the parent artery [16]. Additionally, ruptured aneurysms were found to have a larger surface area exposed to the low wall shear stress when compared to their unruptured counterparts [16]. The remodeling responses in the vascular tissue that emerge in environments of low wall shear stresses are very different from those observed in environments with high wall shear stresses. In a low stress environment, endothelial cells demonstrate an inflammatory response. This response allows fluid to permeate the vessel wall, recruits leukocytes to infiltrate the vessel wall, and prompts smooth muscle cells in the wall to multiply [12]. The result is a wall structure that is much thicker, but less mechanically stable. The infiltration of inflammatory cells is commonly observed in larger ICAs, suggesting that low wall shear

stress-related remodeling plays an important role in the late development of the aneurysms [16].

The natural progression of aneurysm growth is thought to include the effects of both high and low wall shear stress. High wall shear stresses are thought to play a major role in the initiation of ICAs, where the natural remodeling response expands the tissue and relieves a localized stress concentration in the vessel wall. The expansion of the vessel creates a pocket of low wall shear stresses. The low wall shear stress then prompts an immune response and a slow, but constant remodeling process. The remodeling process gradually weakens the vessel wall and expands the pocket outward due to its increased compliance. Some groups have ventured as far as to suggest two distinct phenotypes of ICA. One is characterized by a small diameter and thin, nearly rigid wall that is devoid of most living cells. This aneurysm type would be mediated almost entirely by the high wall shear stress response. On the other end of the spectrum is the category of large ICAs that exhibit thick vessel walls and a high immune cell count within their tissue. Both phenotypes are observed in clinical practice; in fact most ICAs contain regions that display some characteristics from each phenotype [12, 16].

2.2 Clinical Treatments for ICAs – Advantages and Shortcomings

Since ICAs are often discovered in the event of SAH, indicating that a rupture has already occurred, most treatment strategies focus on blocking blood flow into the ICA [18]. By stemming the flow of blood through the ruptured aneurysm, surgeons can limit the damage caused by the SAH and increase the patient's chances of recovery. As imaging

technologies have significantly advanced in the past decade, more and more aneurysms are being identified before rupture. Even though treatments for unruptured ICAs are no longer rushing to limit the effects of an actively bleeding artery, the goals of the treatment still focus on inhibiting blood flow and sealing the aneurysm off from the parent artery. The treatment philosophy of this approach is the large role that blood flow plays in ICA growth; if a treatment can stop the flow of blood into an unruptured ICA, the hemodynamically-driven progression toward rupture is halted [16]. In the long term, these types of flow restricting treatments initiate thrombus formation as the blood flow within the aneurysm stagnates. With the formation of a healthy thrombus, an aneurysm becomes a solid mass, impeding aneurysm recurrence and rupture. This state in which blood flow is entirely blocked from entering the aneurysm is known as *occlusion*. The devices and procedures used to accomplish aneurysmal occlusion vary in both their design and their implementation. Modern aneurysm treatment options have become more diverse with improvements to endovascular surgical procedures, and surgeons will often decide which of the available treatments is ideal on a patient-by-patient basis.

2.2.1 Surgical Clip Ligation

The first treatment that focused specifically on the ICA, rather than the affected artery, was surgical clip ligation. This technique was first documented in 1911 by Harvey Cushing, who described a clamping device made from silver. The clipping devices were first implemented by Walter Edward Dandy in 1937 to successfully treat a 43-year-old patient with a “pea-sized” aneurysm [19]. The surgical clipping treatment relies on a mechanical clamp to constrict the neck of the aneurysm (**Fig. 2.5**) and prevent any blood from flowing into the aneurysm. Eventually, the blood that is trapped in the aneurysm clots

and forms a solid mass, eliminating the risk of rupture. The clip is delivered from outside the artery, meaning that the patient must undergo a craniotomy in which a section of the skull is cut away to allow access to brain tissue. The treatment is most effective for saccular aneurysms with a well-defined neck region, since the clip must be able to completely seal the connection between the aneurysm sac and the parent artery. The clipping device has been significantly altered and refined since its initial conception and is still widely used in modern aneurysm treatments.

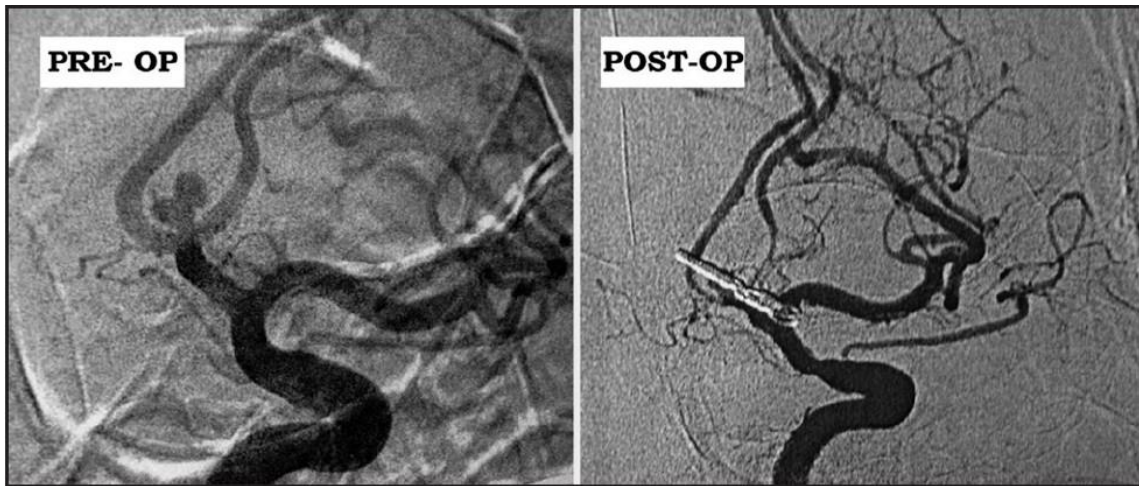


Figure 2.5: Angiographic view before and after treatment of an intracranial aneurysm using surgical clip ligation [20].

In a large-scale randomized study (n=1055), surgical clip ligation procedures performed in patients with subarachnoid hemorrhage resulted in a 69.1% success rate, defined as an absence of death or significant cognitive impairment 1 year after treatment. Although this number is low, it is important to remember that patients who received the treatment were already suffering from subarachnoid hemorrhage caused by aneurysm rupture, and that the clipping procedure was implemented to stem the bleeding [21]. When

used for the treatment of unruptured aneurysms, surgical clip ligation resulted in an 87.4% success rate (no significant mortality or morbidity) [6]. These studies reinforce the common-sense notion that early identification and preemptive treatment of aneurysms is a critical step to improve the treatment outcomes.

2.2.2 Endovascular Coil Embolization

A revolutionary, new type of aneurysm treatment known as endovascular coil embolization emerged in the 1990s, allowing surgeons to treat ICAs without requiring a craniotomy procedure. The technique was first performed in 1990 by *Dowd et al.*, who used platinum coils as the embolic agent. A safer version of the procedure that allowed more control over the coil deployment was introduced by Guido Guglielmi in 1991 [22]. The device, known as a Guglielmi Detachable Coil, provided the foundation for modern endovascular coil embolization. It contained a steel guide wire that allowed the surgeon to fine-tune the positioning of the coils before release. When the position was satisfactory, the wire could be detached via an electrolytic connector component. Guglielmi's design was so effective that it continues to be used in modern aneurysm therapeutics.

Endovascular coil embolization utilizes a much less invasive procedure to stabilize aneurysms from within the intracranial artery. This technique begins with a small incision on the patient's inner thigh that provides access to the femoral artery. The surgeon deploys a catheter into the artery and guides it from the patient's thigh to the affected artery in the brain (**Fig. 2.6-1**). The first catheter that is deployed is known as the guide catheter, and it is equipped to release a radiopaque pigment into the bloodstream. The entire endovascular procedure is conducted under fluoroscopy, a form of real-time X-ray imaging that allows the surgeon to visualize the position of the catheter as it travels. The radiopaque dye allows

the surgeon to visualize the arteries and target aneurysm as a part of the fluoroscopy image. The process of releasing dye to visualize vascular geometries is known as angiography and is considered one of the most effective tools for performing aneurysm treatments and evaluating their effectiveness during follow-up screenings.

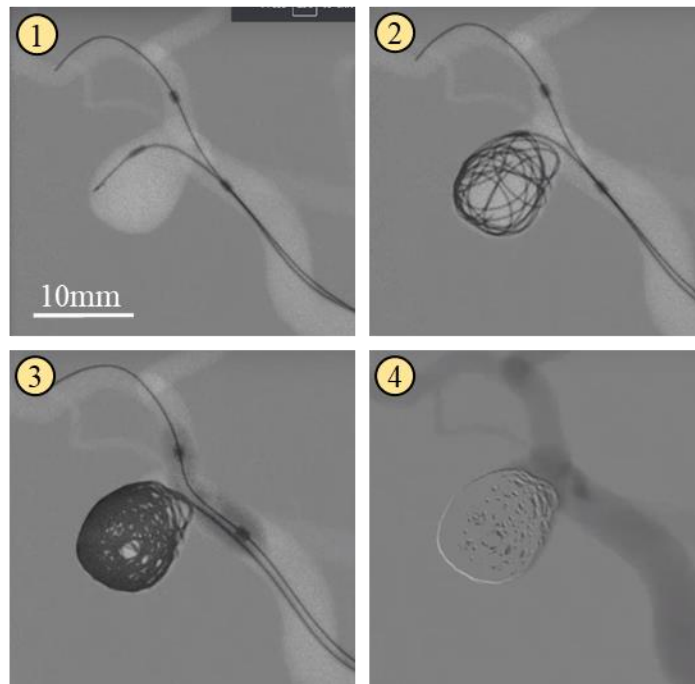


Figure 2.6: (1) Guide catheter is in place, and micro-catheter positions the tip of the coils in the aneurysm sac. (2) Coils are fed into the aneurysm sac. (3) Coil placement continues and a balloon is inflated to prevent coil migration into the parent artery. (4) The coils successfully occlude the saccular aneurysm. Images courtesy of Mentice:

<https://www.youtube.com/watch?v=BpPYaBwrbT8>.

Once the surgeon has positioned the guide catheter near the aneurysm, they introduce a smaller microcatheter containing a thin wire of shape memory alloy with a platinum coating. The shape memory alloy causes the wire to form tight coils as it is

deployed into the aneurysm sac, which allows the surgeon to achieve a relatively high packing density (**Fig. 2.6-3**). The aneurysm is filled with coils until little to no dye from angiographic imaging enters the aneurysm space (**Fig. 2.6-4**). This point is known as occlusion. Shortly after deployment, the coils recruit thrombus forming agents from the blood to create a fibrin dense clot within the aneurysm sac. This clot ideally achieves the same end as surgical clipping and diverts blood flow away from the aneurysm and back into the parent artery. Eventually, the body's natural immune response encapsulates the coils and deposits a layer of endothelial cells over the aneurysm neck.

In a large-scale randomized study (n=1,063), endovascular coil embolization procedures performed in patients with subarachnoid hemorrhage resulted in a 76.5% success rate, defined as an absence of death or significant cognitive impairment 1 year after treatment. Compared with surgical clipping, the endovascular coil embolization reduced patient risk of death/dependence by 23.9% relative to the risk associated with surgical clipping. This corresponds to an absolute risk reduction of 7.4% for the treatment of subarachnoid hemorrhage [21]. For the treatment of unruptured ICAs, the success rate of endovascular coil embolization achieved a success rate of 90.2%. This corresponds to a relative risk reduction of 22.2% relative to the risk posed by surgical clipping and an absolute risk reduction of 2.8% for unruptured aneurysm treatment [6].

One drawback of endovascular coil embolization, however, is the possibility for aneurysm recurrence. One method of classification is the Raymond-Roy occlusion scale (**Fig. 2.7**), which assigns a numerical score to the angiographic occlusion results of coil embolization. This method defines Class I as an entirely occluded aneurysm. Class II is assigned to an aneurysm with blood flow into the neck region. Finally, Class III is assigned

to an aneurysm with blood flow into the sac region. A Class III aneurysm on this scale is considered unsatisfactory, and often indicates a case that will require re-treatment. One study that used angiographic imaging to assess the degree of aneurysm occlusion in the months following treatment with detachable coils, showed satisfactory angiographic occlusion (Class I or II on the Raymond-Roy scale) in 82.2% of cases immediately after treatment. However, follow-up studies reported an aneurysm recurrence rate as high as 33.6% within the first three months of treatment. In 20.7% of cases studied, the recurrence was large enough to warrant re-treatment of the aneurysm with additional coils [23].

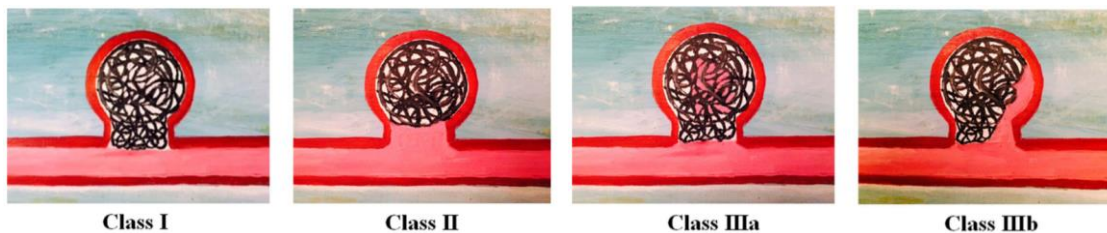


Figure 2.7: The modified Raymond-Roy occlusion scale, which includes two subdivisions of Class III as proposed by Mascitelli *et al.* (2015) [24].

Much of the recurrence that takes place after coil embolization is related to the rearrangement of coils within the aneurysm sac. While the shape memory properties of the detachable coils allow for relatively dense packing, the treatment method is still only able to achieve a 20-30% volume fill ratio and relies on the formation of a healthy thrombus to stabilize the aneurysm in the long-term [25, 26]. This means that coils can potentially rearrange because of blood flow. A modified version of the Raymond-Roy scale proposed by Mascitelli *et al.* (2015) introduces a refined definition of Class III aneurysms, separating them into Class 3a or Class 3b subcategories. Class 3a aneurysms were defined by the presence of dye in the center of the saccular region, whereas Class 3b aneurysms were

defined by the presence of dye in between the coils and the aneurysm wall. Mascitelli *et al.* (2015) showed that Class 3a aneurysms had a 52.78% chance to improve to Class 1 and a 30.56% chance to improve to Class 2 between initial treatment and the first follow-up screening (~8 months). In contrast, Class 3b aneurysms had a 6.38% chance and an 8.51% chance to improve to Class 1 or Class 2 respectively [24]. These results suggest that a void in the center of a group of coils can stabilize due to coil compaction while a void along the aneurysm wall is more likely to cause compaction of coils away from the wall, leading to a renewed risk of rupture.

2.3 Shape Memory Materials – Types and Functions

2.3.1 Shape Memory Alloys

Shape memory materials include a diverse collection of different materials including alloys, polymers, and hydrogels that all can undergo significant deformation before returning to their original shape with the application of an external stimulus. This stimulus-driven automatic recovery from large strains is known as the shape memory effect, and manifests differently in different types of materials. Shape memory alloys (SMAs) consist of two different crystalline structures (martensite and austenite), and the transition between these structures (**Fig. 2.8**) drives the shape recovery. An SMA is heat treated to fix a “memorized” shape, and once they cool from the heat treatment they become easily deformable. An SMA can be thoroughly manipulated, bent, and stretched at low temperatures in its martensitic state, but once it is heated above a temperature threshold,

known as the transition temperature, the material shifts to its austenitic state and returns to the shape set with heat treating.

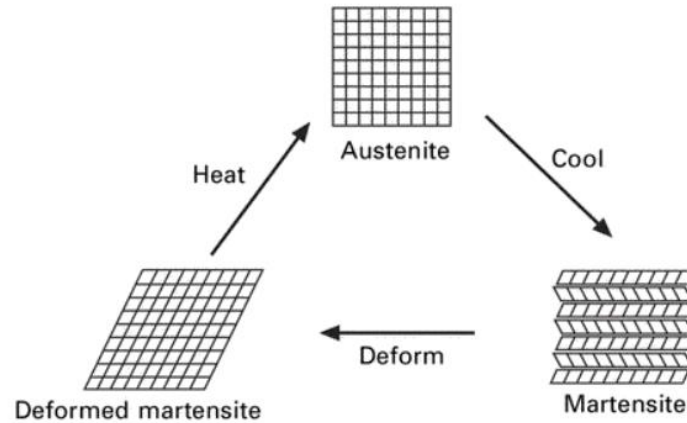


Figure 2.8: The cyclic changes in crystalline state that drive shape recovery in SMAs [27].

2.3.2 Shape Memory Polymers

While SMAs are soft and deformable at low temperatures and harden at high temperatures, shape memory polymers (SMPs) soften when heated and become rigid and glassy when cooled below their transition temperature, as illustrated in **Figure 2.9**. SMPs generally consist of hard and soft segments, which are often highly crosslinked. When the SMP is cured, the polymer gains its “memorized” shape. The polymer remains rigid in a glassy state until heated above its glass transition temperature (T_g). Once heated above T_g , the polymer becomes rubbery and deformable. If the SMP is deformed and then cooled below its T_g once more, any deformations will be preserved due to the re-formation of crosslinking bonds between the polymer chains. The SMP can retain this deformed, rigid state almost indefinitely until it is heated again to a temperature above its T_g . Upon this

thermal trigger, the internal stresses stored in the polymer backbone will return the material to its “memorized” shape [27].

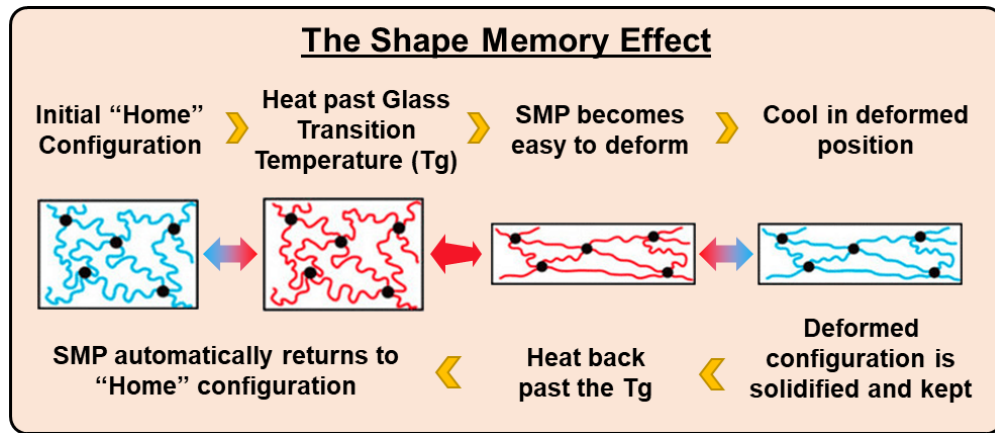


Figure 2.9: A graphical representation of the shape recovery behavior exhibited by SMPs.

Thermoplastic SMP materials can utilize the shape memory effect based on the melting points of the hard and soft polymer segments rather than the crosslinking bonds between polymer chains. These materials are rigid until heated above the melting temperature of their soft segment (T_{ms}), which makes the material rubbery and deformable. The shape memory effect progresses in the same way for these materials as it does for materials using T_g . One unique feature of thermoplastic SMPs, however, is the ability to reconfigure their “memorized” shape. If the material is heated above the melting temperature of the hard segment (T_{mh}), the material melts and can be processed identically to other thermoplastics. Upon cooling, the hard segments are re-formed, and the new shape becomes the “memorized” shape [28].

One final type of shape memory effect has been demonstrated by Xie *et al.* (2010) using perfluorosulfonic acid ionomer (PFSA) [29]. This material exhibited a broad transition temperature, allowing it to store shapes based on the thermomechanical history

of its deformation within the band of transition temperatures. The material could be deformed at a high temperature, then cooled to a lower temperature within the same transition band and deformed again before cooling fully. The resulting shape memory effect for these loading states would reach a peak recovery rate for the second transition at a point very near the temperature at which it was deformed. The recovery would then halt and would reach a new peak recovery rate for the first deformation once it reached the initial deformation temperature. **Figure 2.10** shows this behavior for a specimen that is programmed at three different temperatures before being incrementally heated to recover its original shape. This type of multiple shape memory effect has the potential to allow for materials with multifunctional shape recovery behaviors depending on the type of trigger they are given.

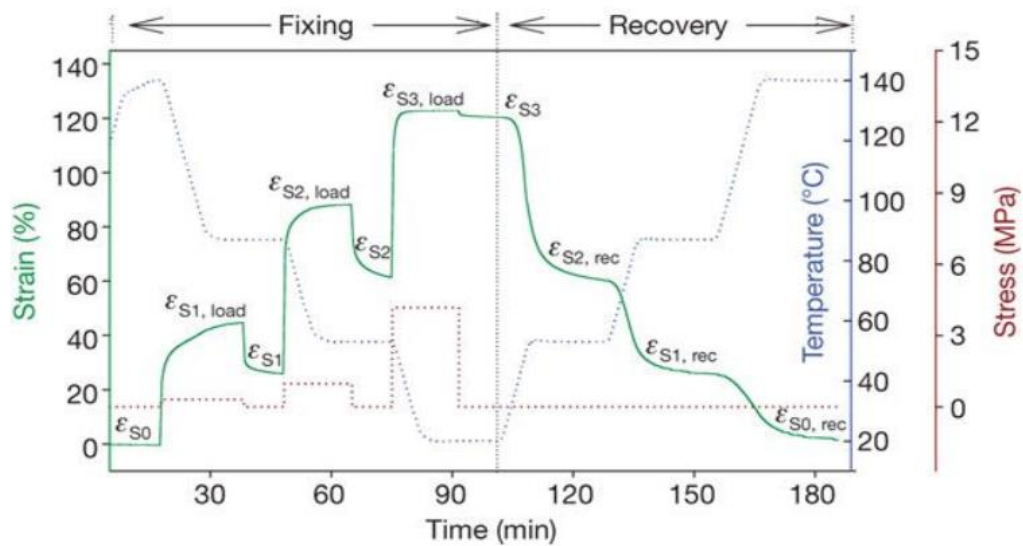


Figure 2.10: Demonstration of multiple shape memory behavior associated with discrete temperature thresholds. The green plot shows three distinct deformations that take place at three distinct temperatures (represented in blue). The polymer recovers each deformation when heated to the temperature at which the deformation occurred [29].

2.3.4 Shape Memory Polymer Foams

The function of an SMP can be drastically altered even in circumstances where the chemical composition of the polymer remains relatively unchanged. The use of SMP foams, which often possesses the same transition temperature and shape recovery properties as its solid counterpart, opens new possibilities for the use of SMP materials. Synthesis techniques used in the production of SMP foam fall into many different categories. One SMP material that lends itself particularly well to foam fabrication is polyurethane. Mitsubishi Heavy Industries produces many different types of polyurethanes with shape memory properties, but still lend themselves to well-established polyurethane foam fabrication techniques [27].

The first of these techniques is chemical blowing, which takes advantage of a gas-producing reaction that occurs during the polymer curing process to form closed-cell pores of variable size. This method had been used with great success in the synthesis of ultra-low-density foam structures from polyurethane SMP materials. Singhal *et al.* (2012) succeeded in using this method to create a polyurethane foam with a porosity of 98% (**Fig. 2.11**) and the ability to theoretically compress a size 64 times smaller than its original volume [30]. A popular application for this type of foam is the creation of bone cell scaffolds, since these do not have a stringent requirement for a uniform pore size [31-33]. Gas blowing can be performed without the use of chemical reactions if the liquid polymer is pressurized and mixed with inert gasses before solidifying. As the pressure is lowered, the gas expands and creates closed pores in a similar manner to the chemical blowing method.

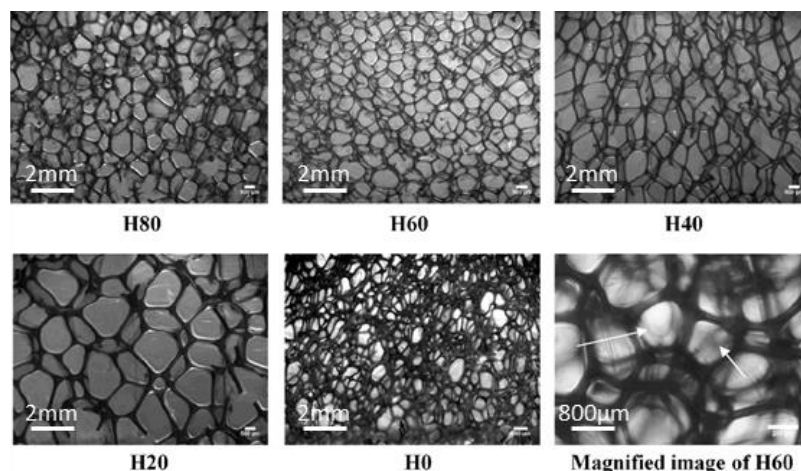


Figure 2.11: Microscopic images of an ultra-low-density polyurethane SMP foam synthesized using chemical blowing techniques [30].

The second technique is known as particulate leaching, in which particles of a uniform size are introduced into the polymer mixture as it cures. After the curing process has finished, the particles are dissolved from the solid using an appropriate solvent to leave interconnected pores that match the size of the particles used to create them. Particulates can be introduced to the polymer in a variety of ways. One method known as *Solvent casting/particulate leaching* (**Fig. 2.12**) uses a solvent to suspend the polymer in solution [34]. The solution is then cast over the top of a scaffold of particles. When the solvent is evaporated out of the solution and the polymer solidifies, the particles are dissolved, leaving regular and interconnected pores. De Nardo *et al.* (2012) demonstrated that a polyurethane SMP foam synthesized using this technique showed promising characteristics for use as a scaffold material for tissue engineering [34]. The foam was synthesized with uniform spherical pores ranging in size from 150-400 μm and a porosity as high as 90%. In addition, the group demonstrated that the foam supported the growth of human osteosarcoma cells without indicating any cytotoxic effects [3]. Another method of particle

dispersion, known as *melt molding*, operates similarly to solvent casting, except the polymer is heated and melted before being cast around the particle scaffold [31]. Another variant of the melt molding method uses an extruder filled with melted polymer in a viscous state with loose particles. Assuming the polymer is viscous enough to hold the particles in suspension, this method creates uniform beams with dissolvable particles mixed throughout [34].

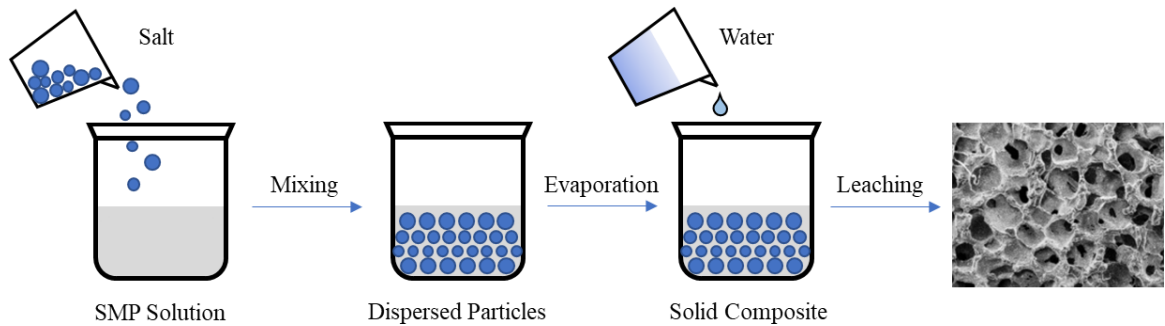


Figure 2.12: Particle leaching procedures. Visualization inspired by Janik *et al.* (2015) [31].

A more complicated method of synthesizing SMP foams uses thermally-induced phase separation (TIPS) to separate the solvent from a polymer solution (**Fig. 2.13**). In this method, the polymer is dissolved in a solvent before being lowered to a temperature below the solvent’s freezing point. At this temperature, the solution separates into “polymer-rich” and “polymer-poor” phases. The “polymer-rich” phase solidifies, while the “polymer-poor” phase forms crystals that can then be removed from the solid. The freezing technique can be modified to alter the number of solvent crystals that form as well as their size, therefore altering the porous characteristics of the resulting foam. Similar to the previous

foam synthesis techniques, this method has drawn interest because of its potential for the creation of soft tissue scaffolds [2].

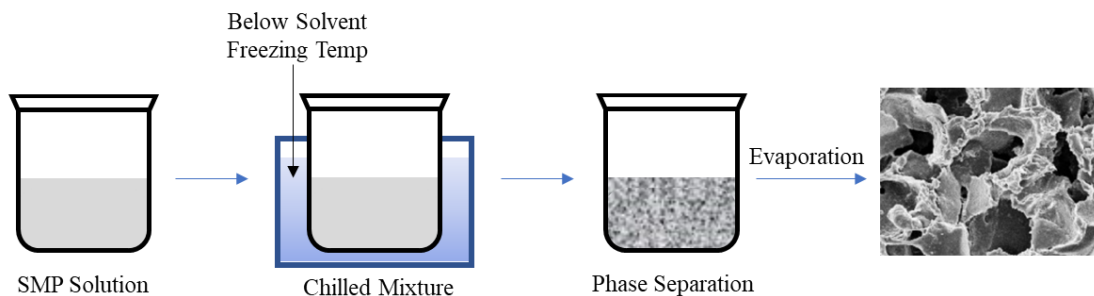


Figure 2.13: Thermally-induced phase separation (TIPS) procedures. Visualization inspired by Janik *et al.* (2015) [31].

The final SMP foam synthesis technique is called *emulsion freeze-drying* (**Fig. 2.14**) [31]. In this method, two immiscible liquids are vigorously mixed to create an emulsion. The first liquid (*continuous phase*) is usually a solution containing the polymer, while the second (*dispersed phase*) is usually water. Once the emulsion is created, it is rapidly frozen with liquid nitrogen and then freeze-dried to remove the solvent and water from the polymer. This method creates a foam with a pore size that varies between 20 and 200 micrometers and a porosity greater than 90%, placing it on even footing with other foaming techniques. The emulsion method has desirable qualities for tissue scaffold preparation since it can potentially circumvent the use of toxic solvents or surfactants.

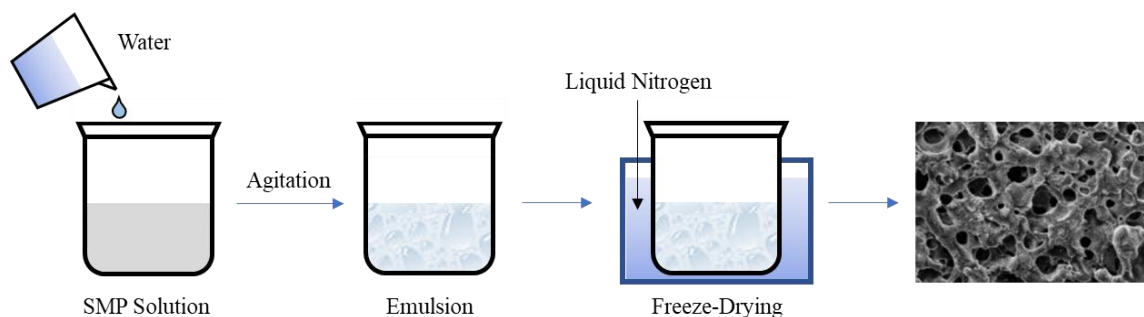


Figure 2.14: Emulsion freeze-drying procedure. Visualization inspired by Janik *et al.* (2015) [31].

A clear trend among emerging SMP fabrication techniques is a focus on biomedical applications, specifically in areas such as tissue engineering. Many SMP formulations fall under the polyurethane family, which tends to exhibit a high degree of biocompatibility [27, 35-37]. Polyurethanes already see wide use in medical applications for this reason, so it is unsurprising that the study of shape memory polyurethanes would trend in the direction of medical device design.

2.5 Shape Memory Polymers – Applications in Medicine

The versatility of SMPs coupled with their unique reconfigurability makes them very promising for use in the development of new medical devices and treatments. Biocompatibility is always a major concern during the development of medical devices, and in recent years a multitude of SMPs have been developed that have minimal impact when implanted in a biological system [35, 36]. In addition to biocompatible SMPs, some researchers have begun to develop biodegradable SMPs for use in scaffolds and *in vivo*

repair structures [38, 39]. An added benefit that comes from the use of SMPs in medical devices is their lack of complexity. Ge *et al.* (2016) demonstrated an SMP-based actuator that used a thermal trigger to grasp small objects [40]. The design was created entirely from SMP and required no additional components assuming that its operating environment was at or above the material's T_g . Reduced complexity in a medical device can correspond to lower production costs and a reduced risk of component failure during use.

2.5.1 Treatment of Ischemic Stroke

One application for which SMPs are being investigated is the treatment of ischemic stroke. Ischemic stroke is caused by the formation of a thrombus in one of the cranial arteries or the migration of a thrombus from elsewhere in the body to a smaller vessel in the brain where it becomes lodged. Patient mortality and morbidity often result from a lack of blood flow, and therefore oxygen delivery, downstream of the effected vessel. One treatment of this condition, known as a thrombectomy, uses a catheter-mounted device to dislodge and ideally collect the thrombus. Metzger *et al.* (2002) utilized polyurethane shape memory polymers from Mitsubishi Heavy Incorporated (MP4510 and MP5510) to create a coiled actuator that could pierce and ideally dislodge a thrombus (**Fig. 2.15**) [4]. The device had a coiled shape that was created using injection molding techniques. With this shape as the “memorized” configuration, the device was heated and deformed into a straight wire shape then cooled to fix the deformed configuration.

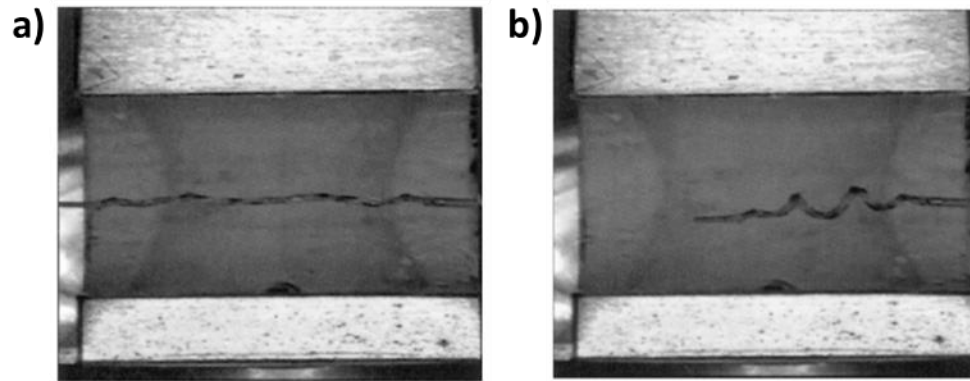


Figure 2.15: The thrombectomy device designed by Metzger *et al.* (2002) in a) its deformed configuration and b) its coiled home configuration [4].

During treatment, the device would be inserted through the thrombus in its straight configuration, then given a thermal stimulus to revert to their coiled shape, anchoring the thrombus between the coils and the delivery catheter. An evolution of this design was produced by Small *et al.* (2007) (**Fig. 2.16**) [5]. The modified device takes the same form of a coiled actuator for piercing and anchoring the targeted thrombus. The major difference with this device was the inclusion of a nitinol wire within the case SMP. The nitinol wire was formed on a mandrel, then suspended in an aliphatic polyurethane SMP material to provide additional rigidity in the device's straightened form.

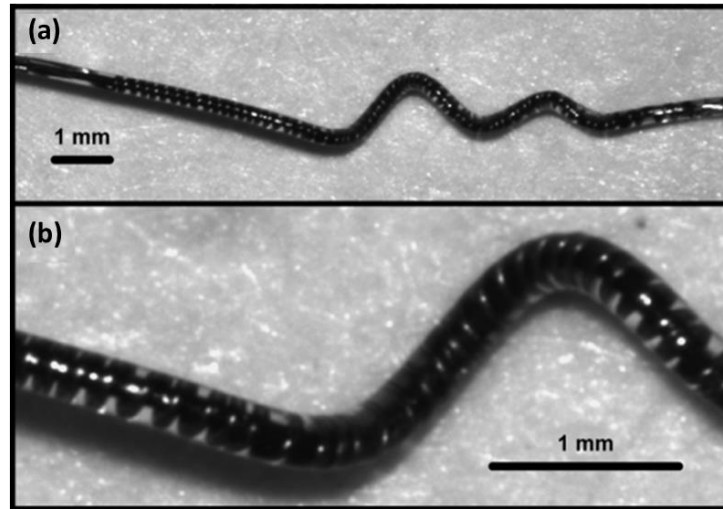


Figure 2.16: Thrombectomy device designed by Small *et al.* (2007): (a) shown in its home configuration, and (b) magnified to show nitinol coils [5].

2.5.2 Self-Deploying Stents

Another promising application of SMP materials is in the deployment of polymer stents. Most metallic stents used in current medical treatments are deployed using balloons at the end of the delivery catheter. One of the most common uses of metallic stents is the widening of clogged blood vessels in a procedure known as angioplasty. However, a shortcoming of metallic stents in this application is the biological response to the stress caused by the device. Long-term remodeling reactions can encase the device in fibrous tissue and lead to the recurrence of blood vessel narrowing, or restenosis, in 15-20% of healthy patients [41]. Modern stents have begun incorporating polymer coatings that are impregnated with slow-releasing drugs to suppress the remodeling response in the vessel walls. SMP materials could not only simplify the deployment process during stent delivery but could also become entirely infused with the same drugs that are deposited on the surface

of modern drug eluting stents. Multiple groups have investigated this application for SMP materials, although no devices have seen clinical use [38, 39, 42].

2.5.3 Aneurysm Treatment and Vessel Occlusion

One of the most promising applications for SMP materials is the improvement of endovascular aneurysm treatments. Despite the success of endovascular coil embolization in general ICA treatment cases, the treatment method results in high rates of recanalization and aneurysm recurrence in cases where the aneurysm size exceeded 10 mm [43]. One study reported the recurrence rate of aneurysms larger than 10 mm was as high as 50.6% when coils alone were used [23]. Another study investigating a combination of all variations of coiling techniques (coils, stent assisted coiling, parent vessel occlusion, and embolic glue) reported a recurrence rate of 26.9% [44]. The use of porous SMP materials as a coating for endovascular coils has been investigated as a way to improve the volume fill rate and stability of the treatment. Coils with a nitinol backbone and an aliphatic polyurethane SMP foam coating were demonstrated by Boyle *et al.* (2017) with successful, albeit slow, deployment in an *in vitro* aneurysm environment [45]. The coils were designed to deploy upon contact with water, which takes 30 minutes to expand from a diameter of 0.5 mm to 0.68 mm (**Fig. 2.17**). While this design could improve the efficiency of coil embolization, other SMP-based aneurysm treatments may allow for more rapid deployment and more efficient occlusion.

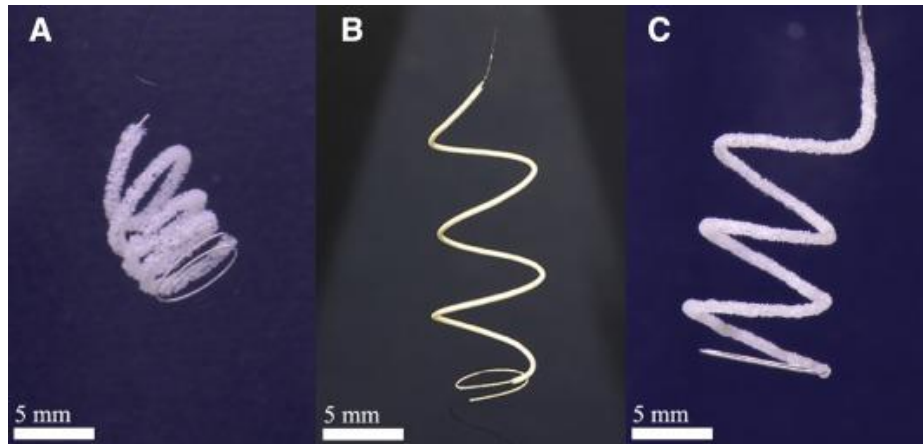


Figure 2.17: SMP foam-coated coils designed by Boyle *et al.* (2017): A) before compression, B) after compression, and C) after immersion in warm water (37 °C) for 30 minutes [46].

Instead of simply modifying coil embolization procedures, porous SMP materials have been investigated by a multitude of research groups as a total replacement for endovascular coils in ICA embolization treatments. Metcalfe *et al.* (2003) proposed the use of a material known as cold hibernated elastic memory foam (CHEM), a material previously investigated by NASA for deployable space structures, coupled with a catheter delivery system to occlude the aneurysm space [36]. The SMP foam in this treatment would be delivered in a compressed state through the narrow cranial arteries before undergoing a large volume expansion upon arrival at the aneurysm location. The potential of CHEM foam was supported by an *in vivo* canine study using artificially created aneurysms. The foam showed a minimal inflammatory response and desirable endothelial cell growth across the neck of the aneurysm.

Similar devices using aliphatic polyurethane SMPs have been developed with equally promising results. Another *in vivo* study performed by Rodriguez *et al.* (2014) in artificially

created porcine aneurysms indicated minimal inflammatory response and an evenly distributed infiltration of fibroblasts [35]. Histology revealed healthy thrombus formation throughout the entirety of the SMP plug and complete endothelialization of the aneurysm neck, which is illustrated in **Figure 2.18**.

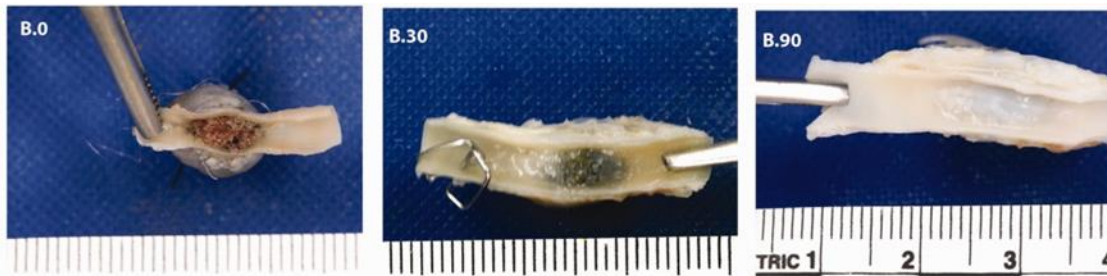


Figure 2.18: Results from *in vivo* porcine studies using aliphatic SMP foam (B.0) response after 30 minutes of implantation, (B.30) response and partial endothelialization after 30 days of implantation, and (B.90) total endothelialization after 90 days of implantation [35].

Using the same foam material, Maitland *et al.* (2007) demonstrated a novel laser activated device design in an in-vitro aneurysm environment (**Fig. 2.19**) [47]. The design used an embolization plug that was machined from a larger block of SMP foam before being crimped onto a cylindrical light diffusion device made from the same material. The diffusion device was attached to the end of a fiber optic cable that ran through a catheter. A laser was directed through the fiber optic cable and diffused at the end of the catheter, heating the SMP foam and deploying the device.

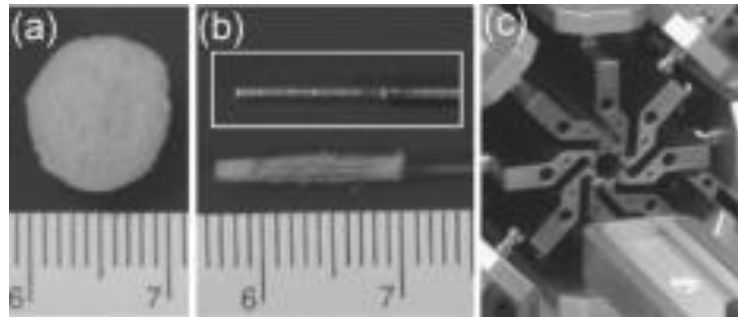


Figure 2.19: Laser-deployed SMP foam embolization device designed by Maitland *et al.* (2007): (a) uncompressed SMP foam sphere, (b) box indicates light diffuser tip, below is the compressed SMP foam crimped around the light diffuser, and (c) heated crimping device used for SMP compression [47].

Although the prototype faced issues related to convective cooling from fluid flow, the design convincingly illustrated a novel treatment technique that utilized SMP foam for aneurysm occlusion. Another later study from Hwang *et al.* (2013) used a bundle of heated wire in place of a laser diffuser to initiate deployment at the center of a device made from the same SMP foam (**Fig. 2.20**) [48]. In addition to the new heating method, this new design included tungsten particles within the SMP foam, which enabled the use of fluoroscopy to position and deliver the foam. All parts of the device functioned as planned except the SMP foam, which deployed automatically at body temperature, roughly 20 °C too low, when it was introduced into the flow loop.

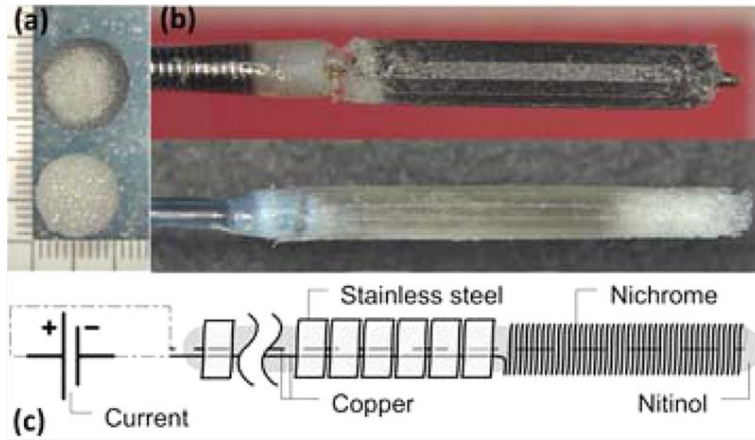


Figure 2.20: Resistively heated SMP foam embolization device designed by Hwang et al. (2013): (a) undeformed SMP spheres, (b) crimped SMP devices, top containing tungsten particles for visibility, and (c) schematic diagram of heating element [49]

CHAPTER 3: Pristine Shape Memory Polymer Synthesis and Characterization

3.1 Introduction

An intracranial aneurysm (ICA), or a cerebral aneurysm, is an abnormal focal dilation and weakening of an arterial blood vessel in the brain with a prevalence of 0.5-6% in adults [49, 50]. Although most aneurysms are asymptomatic and do not rupture, they can grow unpredictably, and even small aneurysms (size ≤ 5.0 mm) carry a risk of rupture. Incidental rupture of an ICA is most common between age 40 and 65, associated with 50-80% of the subarachnoid hemorrhage (SAH) cases, which causes individual's death before receiving medical attention associated with a mortality rate as high as 40% within the first week, and accounts for about 5-8% of all strokes, [9, 10, 51-55].

Currently, surgical clipping and endovascular coil embolization are the two most common treatment methods for intracranial aneurysms. Clipping of intracranial aneurysms requires craniotomy and neurosurgeon places a clip across the neck of the treated aneurysm to block it from the normal circulation [56]. In contrast, micro-catheter delivery-based endovascular therapy with Guglielmi detachable coils (GDCs) [21, 23, 57] is a minimally invasive surgical technique, which aims at excluding the aneurysmal sac and neck from intracranial circulation by means of complete and lasting occlusion. Although GDC-based coil embolization therapy has been considered as an alternative to surgical clip ligation that is associated with higher procedural mortality [58-60], recent studies [44, 61-63] have shown that unsatisfying rates of aneurysmal recanalization and incomplete occlusion are still emerging challenges in endovascular coil embolization. Therefore, development of

novel biomedical devices for the use in minimally invasive surgical procedures as tailored to patient's complex aneurysm geometry is essential to improve the long-term therapeutic outcomes of current endovascular techniques and to overcome the above-mentioned clinical challenges.

As the first logical step towards the attainment of this research objective, we, in this study, comprehensively characterize the thermomechanical properties and the shape recovery capability of aliphatic urethane shape memory polymers (SMPs) and investigate its potential applications to manufacturing individualized embolic devices for treating intracranial aneurysms. Shape memory polymers, such as polyurethane [64, 65], have aroused great attention from scientists and engineers owing to their excellent shape memory behavior, high biocompatibility, fast shape recovery speed, and low synthesis cost. This type of polymer is synthesized using hexamethylene diisocyanate (HDI), N,N,N',N'-tetrakis (hydroxypropyl) ethylenediamine (HPED), and Triethanolamine (TEA), and consists of two segments at the molecular level: (1) the rigid and glassy segments determining the permanent shape and (2) the amorphous segments controlling the temporary shape. Currently, most of the biocompatible SMPs used for biomedical applications are thermally induced. When heated above its glass transition temperature (T_g), the amorphous segments of the SMP transition from a glassy state to a rubbery state, allowing the polymer to deform under an external load [66]. After cooling below T_g and subsequent releasing of the external loading, the temporary shape is obtained. The polymer can autonomously return to this programmed shape without external mechanical stimuli when polymer temperature increases above T_g again.

Biomedical devices fabricated using SMPs can potentially be introduced into a patient's body in a temporary, compressed shape and then be expanded on demand to their programmed shape as required. Since the shape recovery can be facilitated with a certain triggering mechanism, such as increasing temperature, the release of medical devices can be completed without additional complex surgical operations, but rather through the micro-catheter. Many biomedical devices and applications have been developed for SMPs that allow triggered responses, including self-tightened biodegradable sutures [67], a micro-actuator for blood removal [68], and stents [69].

In this study, we aim to develop a detailed experimental procedure for the synthesis of aliphatic urethane based SMPs and perform comprehensive thermomechanical characterization on a range of SMP compositions to investigate connections between the working temperature of the polymers and their mechanical behavior. Specifically, we identify the glass transition temperatures of each composition using both dynamic mechanical analysis (DMA) and differential scanning calorimetry (DSC) tests, and we determine the threshold for thermal degradation of each composition using thermogravimetric analysis (TGA). We also report the results of uniaxial cyclic and failure testing and analyze the differences in behavior between different compositions. We conduct this research with the goal of eventually designing an advanced individualized endovascular embolization device using aliphatic urethane SMPs as the primary material. Consequentially, we discuss the results in terms of the desirable physical qualities such an implantable material that would need to possess.

3.2 Methods

3.2.1 Materials and SMP synthesis

In this work, (i) hexamethylene diisocyanate (HDI, $\geq 99.0\%$), (ii) N,N,N',N'-tetrakis (hydroxypropyl) ethylenediamine (HPED, $\geq 98.0\%$), and (iii) Triethanolamine (TEA, $\geq 99.0\%$) were purchased from Sigma-Aldrich. All the above materials were used as received for synthesizing aliphatic urethane shape memory polymers. Twelve combinations of these three monomers were synthesized, with their respective SMP formulations given in **Table 3.1**.

Table 3.1: Percent monomer content, monomer-mixture stirring time, and the curing heating rate for all the twelve SMP compositions.

	Monomer Content (% by weight)			Stirring Time (seconds)	Heating Rate ($^{\circ}\text{C}/\text{hour}$)
	HDI	HPED	TEA		
SMP1	53.5	46.5	0.0	150	30.0*
SMP2	53.9	44.5	1.6	170	29.6
SMP3	54.3	42.5	3.2	200	29.2
SMP4	55.1	38.4	6.5	225	26.4
SMP5	56.0	34.1	9.9	240	25.2
SMP6	56.9	29.7	13.4	255	23.6
SMP7	57.8	25.1	17.1	270	21.1
SMP8	58.8	20.4	20.8	285	18.5
SMP9	59.7	15.6	24.7	310	15.9
SMP10	60.7	10.6	28.7	330	12.5
SMP11	61.8	5.4	32.8	350	9.6
SMP12	62.3	2.7	35.0	445	8.5

*Suggested same heating rate for SMP curing in Wilson *et al.* (2007) [70].

3.2.2 SMP synthesis procedure

Various SMPs were synthesized by mixing different ratios of HPED, TEA, and HDI. The molar ratios for each batch were sourced from the previous study by Wilson *et al.* (2007) [70] with modifications to the second and last compositions (**Table 3.1**). All measurement and mixing procedures occurred within a nitrogen-filled glovebox to avoid moisture contamination of the monomers (**Fig. 3.1a**). The glovebox received a steady flow of nitrogen through an inlet at the top of the rear panel and vented gas into a fume hood from an outlet at the bottom of the rear panel. This prevented air from entering the work space and removed any undesired moisture prior to the synthesis. Nitrogen flow could be redirected to the vacuum oven used later during synthesis via a set of ball valves.

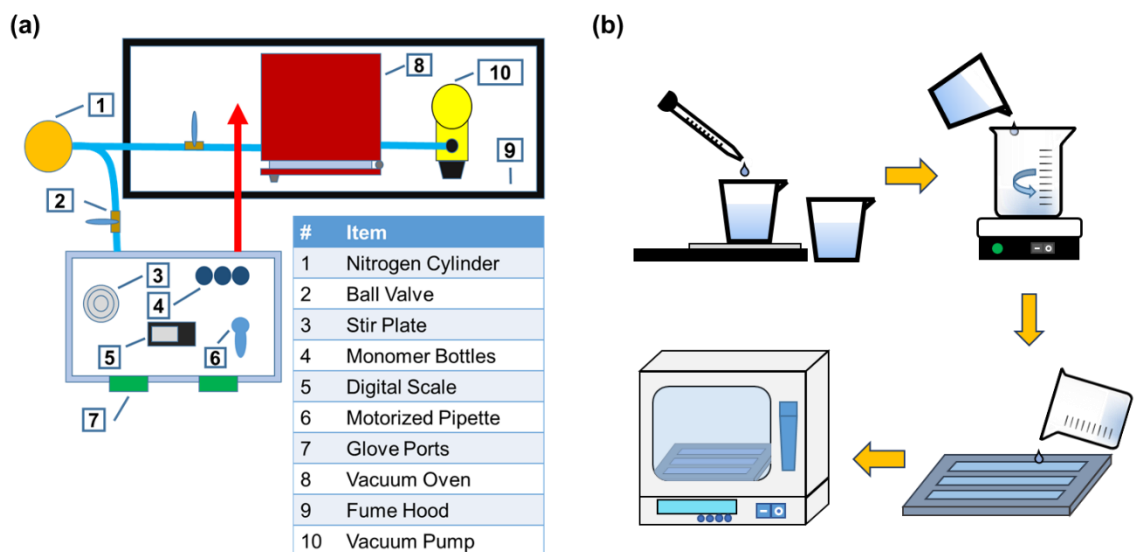


Figure 3.1: (a) Top-view schematic of the in-house equipment used in the shape memory polymer synthesis. (b) An illustration of the synthesis procedure showing specifically (i) the measurement of each monomer, (ii) the mixture of monomers to form the polymer, (iii) the deposition of the mixture into previously cast molds, and (iv) the curing of the mixture in a vacuum oven.

Monomer weighing was performed using a Fisherbrand motorized pipette filler (Thermo Fisher Scientific) and a digital scale (AWS-100, American Weigh Scales). In brief, the HPED and TEA were measured in the same 100 mL glass beaker, while HDI was kept in a separate container until the stirring stage where it was added to the mixture and stirred on a magnetic stirring plate (**Fig. 3.1b**). The mixture was stirred gently to avoid the introduction of gas bubbles into the liquid. Stirring continued until the mixture showed a sudden transition from translucent to uniformly clear. The time required to produce this transition increased as the ratio of HPED in the mixture decreased and the ratio of HDI increased (**Table 3.1**).

The procedures in Wilson *et al.* (2007) [70] suggested including an excess of 1-2% isocyanate (HDI). However, our early synthesis results were unsatisfactory, and the removal of this excess improved the success rate of our syntheses. We also observed a tendency of the mixtures to cure before degassing could take place, leaving large air bubbles in the resulting specimens. Since the mixture of the monomers is an exothermic reaction, we noticed large batches of the mixture could generate adequate heat to act as a catalyst for the curing process. To avoid these scenarios, we limited the size of each batch to 16-18 g, and mixed multiple small batches during a single synthesis procedure, rather than mixing the full volume all at once.

Once the mixture had sufficiently reacted, we quickly removed it from the glovebox and poured the contents into a set of silicone rubber molds—rectangular beams (45 mm x 8 mm x 1 mm) for glass transition-related characterizations and ASTM D638 Type V dog bones for tensile mechanical testing (cf. **Section 2.3** and **Section 2.4**, respectively). Prior to the synthesis, two coats of mold release (Buehler 208186032) were applied to each

specimen mold to minimize bubble generations due to any undesired interactions between the mixed monomers and the silicone rubber during curing. Then, specimen molds were placed in a vacuum oven (Being BOV-20) and 5 vacuuming (-0.8 bar) and nitrogen purging steps were performed to create a nitrogen protected environment in the oven before degassing. A strong vacuum (-0.925 bar) was next induced using a vacuum pump for 10-12 minutes to remove gas bubbles trapped in the mixture (**Fig. 3.1a-b**). For cases where multiple batches of mixture were used, we filled each mold half way with mixture and performed an initial degassing step while mixing the other batch. When the first degassing had finished, we filled the rest of the space of the molds and proceeded with the above-mentioned vacuuming-purging and degassing steps. An “overflow” section was included in our specimen molds to trap bubbles as introduced during the degassing procedure. The top few millimeters of each specimen could be polished off to leave a smooth finishing.

When curing the SMP specimens, we followed the procedure in Wilson *et al.* [70] with several modifications. The specimens were kept at room temperature for one hour, then the temperature was increased at a steady rate to 130 °C, where it was kept for another hour. The heating rate of temperature was proportional to the glass transition temperature (T_g) of the specimen being cured, to ensure each SMP had an equal curing time before reaching its T_g (**Table 3.1**). During the curing process, we observed a slow loss of vacuum potentially caused by the pressure increase associated with the heating. To maintain a consistent vacuum, we resealed the oven in intervals of an increase of 7.5 °C, by reestablishing the vacuum (-0.4 bar) and quickly purging the system with nitrogen. Upon completion of the curing step, the SMP specimens were carefully removed from the molds

and stored in a vacuum desiccator (Bel-Art Lab) to ensure no moisture contamination occurred before subsequent thermomechanical characterization experiments.

3.2.3 Thermomechanical Characterization of the synthesized SMPs

The mechanical properties of shape memory polymers vary according to temperature, especially in the range of their glass transition temperatures. To characterize these temperature-dependent mechanical properties with various polymer compositions, we conducted a series of thermomechanical tests, including the dynamic mechanical analysis, thermogravimetric analysis, differential scanning calorimetry, and uniaxial tensile tests considering failure and cyclic loading conditions, to pinpoint the glass transition temperature of the SMPs and to better understand their thermally-dependent mechanical behaviors.

Dynamic mechanical analysis (DMA)

Dynamic mechanical analysis (TA Q800) was used to measure the mechanical properties of synthesized SMPs. The SMP beam specimens were heated under a nitrogen atmosphere from 20 °C to 120 °C at a heating rate of 5 °C/min and in the tension mode with a cyclic frequency of 1 Hz. DMA studies revealed the significant mechanical and thermal properties of the samples, such as storage modulus, loss modulus and glass transition temperature.

Thermogravimetric analysis (TGA) and differential scanning calorimetry (DSC)

Thermal analysis data were measured by both thermogravimetry (TA Q50, TA Instruments) and differential scanning calorimetry (TA Q20, TA Instruments). All measurements were performed under nitrogen environment. In brief, the thermal

degradation behavior of the samples was recorded with heating from room temperature to 600 °C at a rate of 10 °C/min. An in-house MATLAB (MathWorks) program was used to determine the onset temperature of thermal degradation, which was used as reference for the ensuing DSC measurements. The program performed a linear regression on a section of each specimen's TGA curve below T_g , and another linear regression of the region on the TGA curve between 90% and 85% mass. The intersection of these two lines was determined to be the threshold of thermal stability. DSC measurements were carried out by: (1) heating from 20 °C to 160 °C at a rate of 5 °C/min, (2) cooling to 20 °C at 50 °C/min, (3) maintaining for 3 minutes at 20 °C, and then (4) repeating the above procedures. DSC studies revealed the significant thermal properties of the samples, such as the glass transition temperature. All the DSC data presented in this study were from the second heating cycle.

3.2.4 Mechanical testing for the synthesized SMPs

Before performing tensile and cyclic testing on the SMP dog-bone specimens, the overflow region was removed to produce a clean finish on both sides of the specimen and eliminate imperfections. The samples were polished using a custom designed and 3D printed mount on a rotary polishing machine (LaboPol-5, Struers). Once polished, the width and thickness of the testing region were measured thrice each and averaged. Tensile failure testing was conducted using a uniaxial tensile testing system (Instron 5969, Instron). Double-sided padded tape was applied to both sides of each gripping region before mounting to prevent slippage during testing.

Failure testing was conducted at 10 °C above the T_g of each specimen in a temperature regulated environment on the Instron. The specimens were mounted in three

steps. First, the base of the sample was clamped into the bottom set of grips and allowed to heat up to the temperature of the testing environment. Second, the top section was clamped into the top set of grips, and the distance between the two grips was measured with a caliper. After measuring the distance between the grips, the extension reading on the Instron was zeroed, and as the sample returned to testing temperature the grip positions were adjusted to keep the measured load as close to zero as possible. Finally, both sets of grips were tightened to make up for the relaxation of the SMP past its T_g . Once the sample reached testing temperature and the measured load was returned to zero, the extension measured by the Instron testing machine was added to the previously measured length and the extension was zeroed once again. This value was recorded as the initial length of the specimen. Upon starting the test, the specimens were subjected to a displacement of 2 mm/min until failure. Five failure tests were completed per specimen, and the best three were selected for characterization purposes based on relative consistency of the elastic modulus and failure stress values.

The procedures for cyclic testing closely resembled those for failure testing. Another set of dog-bone specimens were tested at 10 °C above T_g and the same three step mounting procedures were exercised as previously mentioned. For the cyclic tests, each sample underwent three cycles of preconditioning at 25% of the failure strain as determined during failure testing. After the preconditioning step, the samples underwent ten loading and unloading cycles of the previously determined 50% failure strain. Both preconditioning and cycling steps were carried out at the same strain rate of 2 mm/min as the failure tests.

3.2.5 Quantification of shape recovery capability

The shape recovery function of the synthesized SMPs was investigated by bending a straight beam sample at a 180° angle, then measuring the time required for full recovery at various temperatures. We followed a method similar to the recovery tests employed by Lin *et al.* (1998) and Lan *et al.* (2009) [71-73]. In brief, the initial bend was achieved using a 3D-printed mold. The beam was heated above its glass transition temperature, and then placed into the mold where the specimen could cool and maintain its shape at the desired angle. To measure the recovery time, a video camera was placed directly above a beaker of water on a hot plate. The bent sample was held with forceps on a ring stand and swiftly lowered into the heated water bath, where the SMP specimen was fully recovered. The video was analyzed frame by frame to determine the elapsed time between any two specific angles of 45, 90, 135, 165, and 180 degrees. This procedure was conducted using water baths at T_g , $T_g + 5$ °C, and $T_g + 10$ °C for each sample. Three repeated recovery tests were conducted at each of the above temperature levels, resulting in a total of 9 recovery time measurements for each SMP composition.

3.3 Results

3.3.1 DMA results

All SMP compositions showed a single steep transition in their shear storage modulus, each occurring at a different temperature threshold (**Fig. 3.2a**). A $\tan(\delta)$ plot (**Fig. 3.2b**) was used to determine the glass transition temperature of each SMP composition. These values were taken at the peak of the $\tan(\delta)$ plot and decreased monotonically from

SMP1 to SMP12, ranging from 83.2 °C to 32.3 °C (**Table 3.2**). The storage moduli generally increased from SMP1 to SMP12; however, SMP10 exhibited exceptionally large values both above and below its glass transition temperature. Another factor which varied with the SMP composition was the change in the storage modulus from $T_g - 5$ °C to $T_g + 15$ °C. With a few exceptions, the storage modulus of each specimen was reduced by a factor of 20-30 times its value at $T_g - 5$ °C when raised to $T_g + 15$ °C. Shear modulus values at both temperatures tended to be larger for specimens nearer to SMP12, but there was not a consistent increase from one composition to another. A notable outlier is the shear modulus of SMP10 at $T_g + 15$ °C, which is exceptionally large compared to the other compositions.

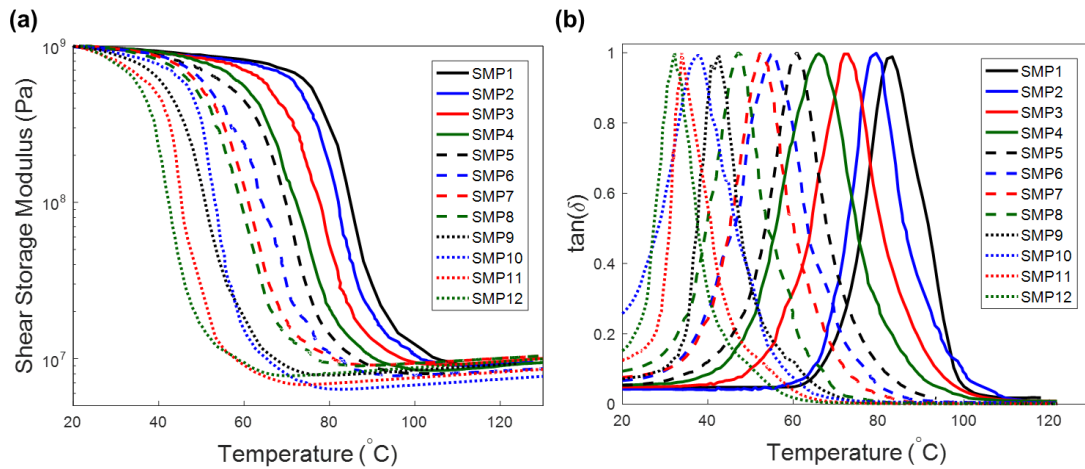


Figure 3.2: (a) Shear storage modulus of all the twelve SMP compositions as directly measured from the DMA tests, and (b) $\tan(\delta)$ curves as derived from the DMA testing results for determining the T_g of each SMP composition.

3.3.2 TGA results

The TGA testing results (**Fig. 3.3**) show two major slopes occurring near 300 °C and 400 °C. The distinction between these two slopes becomes more pronounced for SMP

compositions closer to SMP12 that contain high percentages of the TEA. Values for the onset of thermal degradation were determined for each composition with values, showing no consistent trend, ranging from 268.2 °C to 284.7 °C (**Table 3.2**). We determined the temperature at which each SMP composition degraded to 90% of its original weight. This value varied little between specimens, ranging from 275 °C to 293 °C (**Table 3.2**). Generally, this value increased from SMP1 to SMP12, but with an appreciable variation between individual compositions. The temperature required to degrade the SMPs to 50% weight varied more than the values for 90% degradation, ranging from 356.6 °C to 316.5 °C; however, these values showed a more uniform increase from SMP1 to SMP12 (**Table 3.2**).

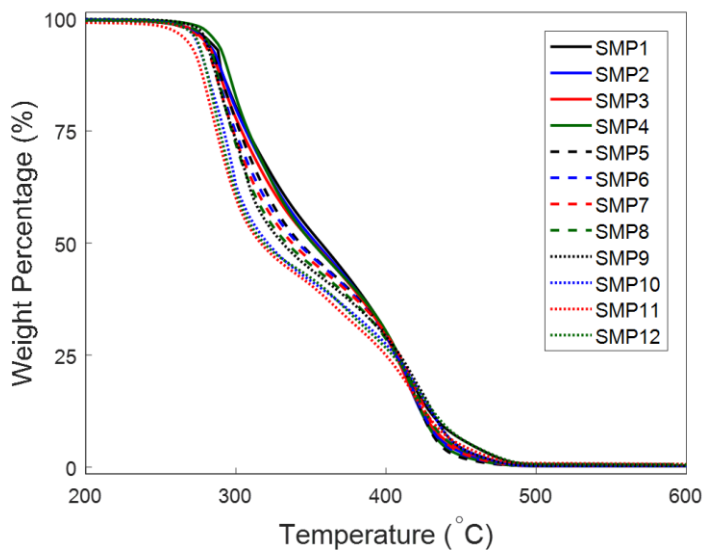


Figure 3.3: TGA results showing the decomposition of the SMP with increasing temperature.

3.3.3 DSC results

The results of the DSC tests were used as a secondary means of determining the T_g of each SMP composition (**Fig. 3.4** and **Table 3.2**). To extract these values, we used the local minimum of the resulting heat flow plots (**Fig. 3.4**), showing a monotonic decrease from SMP1 to SMP12. Such a monotonic decrease is also reflected in the T_g of the SMP compositions, ranging from 87 °C to 33 °C. These T_g values from the DSC testing generally agree with the values determined using the $\tan(\delta)$ plot in the DMA tests (**Fig. 3.2**). However, the T_g values determined using DSC analysis are consistently higher than those from DMA and $\tan(\delta)$ analysis, but the difference is small enough to attribute to differences arising from the method of determination. The same difference was observed in the analysis performed by Wilson *et al.* (2007) [70].

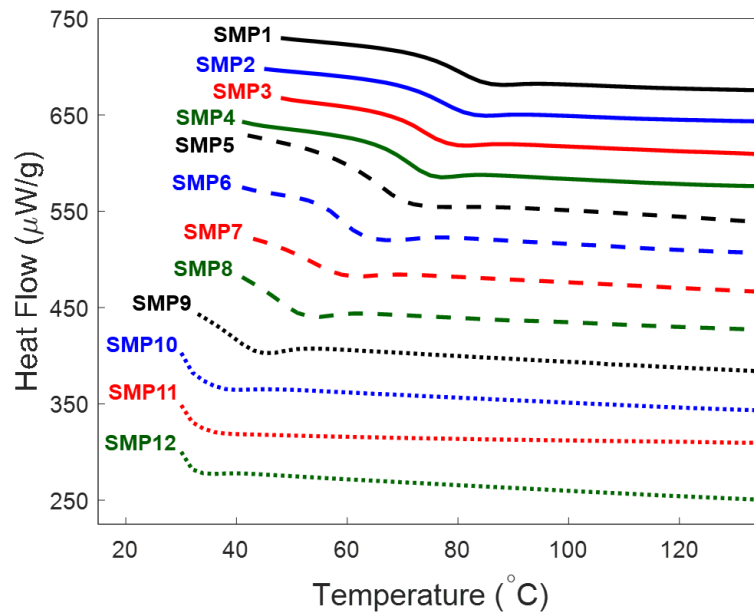


Figure 3.4: DSC results used for determinations of the T_g for each SMP composition.

Table 3.2: Glass transition temperature (T_g) and storage modulus from the DMA tests (cf. **Fig. 3.2**), T_g from the DSC tests (cf. **Fig. 3.4**), and the temperature levels associated with 90% and 50% remaining weights of the SMPs from the TGA tests (cf. **Fig. 3.3**).

	DMA			DSC	TGA		
	T_g (°C)	Storage modulus at $T_g - 5^\circ\text{C}$ (MPa)	Storage modulus at $T_g + 15^\circ\text{C}$ (MPa)	T_g (°C)	Temperature (°C) associated with the onset of thermal degradation	Temperature (°C) associated with 90% remaining weight	Temperature (°C) associated with 50% remaining weight
SMP1	83.2	403.3	13.3	87	276.6	289.5	356.6
SMP2	79.5	442.0	13.4	83	278.2	288.7	353.6
SMP3	72.6	459.4	15.7	76	276.6	286.3	351.4
SMP4	65.7	529.6	19.3	73	284.7	293.5	351.0
SMP5	61.1	563.4	22.4	67	277.5	287.1	342.8
SMP6	55.5	589.8	26.8	63	276.8	285.5	341.2
SMP7	52.5	649.9	23.7	56	275.9	284.5	338.1
SMP8	47.5	759.4	46.0	53	278.4	285.8	333.8
SMP9	42.6	706.4	24.6	45	276.7	284.8	331.0
SMP10	37.2	882.7	142.7	39	270.8	279.2	321.2
SMP11	33.9	830.9	43.8	34	268.2	275.5	316.5
SMP12	32.3	867.7	23.9	33	272.8	279.3	318.7

3.3.4 Uniaxial tensile testing results

Under uniaxial tensile failure tests, the SMPs exhibited a sharp decrease in the failure stress and the failure strain from SMP1 to SMP3 and an increase in both failure stress and failure strain from SMP3 to SMP12 (**Fig. 3.5** and **Table 3.3**). The trends in the data are nonlinear, with large increases near compositions SMP12 and SMP1 (**Fig. 3.5**). The maximum failure stress and strain occur at SMP12 with values of $6.88 \text{ MPa} \pm 0.29 \text{ MPa}$ and $54.4\% \pm 2.97\%$, respectively. The minimum stress and strain occur at SMP3 with values of $3.34 \text{ MPa} \pm 0.16 \text{ MPa}$ and $16.2\% \pm 0.72\%$, respectively. For most of the specimens, we observed a decrease in both failure stress and strain as the HPED content increased in the SMP composition.

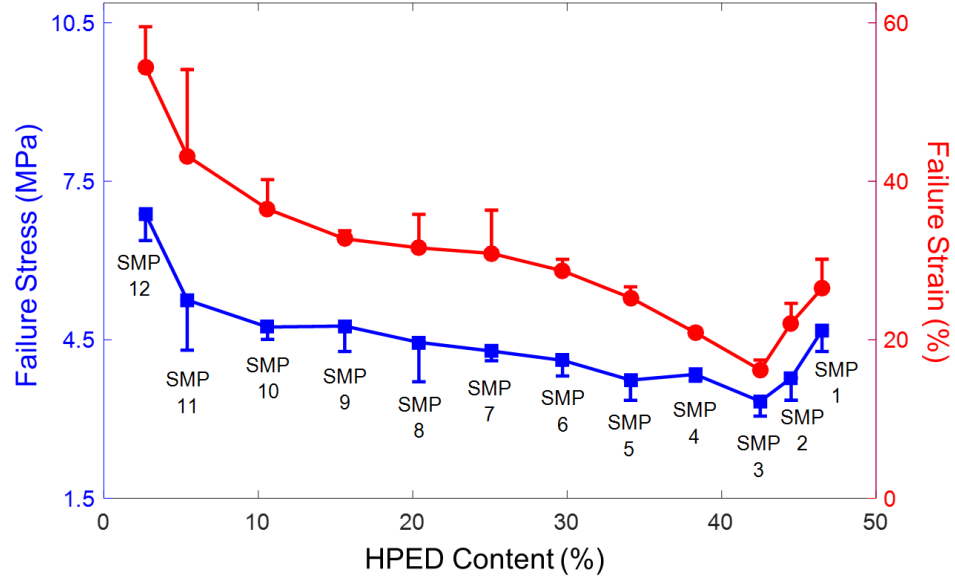


Figure 3.5: Mean \pm SEM of the failure stress (blue filled squares) and failure strain (red filled circles) for all the twelve SMP compositions (n=2) under uniaxial tension testing ($T_g + 10^\circ\text{C}$).

Table 3.3: P-values from 1-way analysis of variance comparing SMP failure strain values (green shading indicates statistically significant).

	SMP 2	SMP 3	SMP 4	SMP 5	SMP 6	SMP 7	SMP 8	SMP 9	SMP 10	SMP 11	SMP 12
SMP 1	0.115	0.010	0.059	0.624	0.376	0.317	0.188	0.077	0.029	0.066	0.002
SMP 2		0.014	0.461	0.106	0.010	0.035	0.013	0.006	0.002	0.012	<0.001
SMP 3			0.004	0.001	<0.001	0.011	0.004	0.004	0.001	0.013	<0.001
SMP 4				0.007	0.001	0.036	0.012	0.009	0.002	0.024	<0.001
SMP 5					0.040	0.166	0.070	0.034	0.008	0.048	0.001
SMP 6						0.555	0.330	0.108	0.028	0.086	0.001
SMP 7							0.865	0.384	0.216	0.157	0.006
SMP 8								0.410	0.204	0.163	0.004
SMP 9									0.730	0.316	0.011
SMP 10										0.375	0.008
SMP 11											0.187

Table 3.4: P-values from 1-way analysis of variance comparing SMP failure stress values (green shading indicates statistically significant).

	SMP 2	SMP 3	SMP 4	SMP 5	SMP 6	SMP 7	SMP 8	SMP 9	SMP 10	SMP 11	SMP 12
SMP 1	0.035	0.009	0.026	0.042	0.120	0.198	0.669	0.516	0.816	0.387	0.004
SMP 2		0.181	0.801	0.905	0.297	0.112	0.185	0.368	0.017	0.037	<0.001
SMP 3			0.046	0.218	0.030	0.008	0.073	0.160	0.003	0.029	<0.001
SMP 4				0.671	0.229	0.027	0.239	0.461	0.004	0.064	0.001
SMP 5					0.255	0.090	0.216	0.397	0.018	0.063	0.001
SMP 6						0.437	0.506	0.784	0.045	0.118	0.001
SMP 7							0.730	0.980	0.057	0.159	0.001
SMP 8								0.804	0.555	0.315	0.010
SMP 9									0.430	0.264	0.012
SMP 10										0.417	0.003
SMP 11											0.058

As for the uniaxial tensile cyclic tests, the SMPs show a noticeable relaxation behavior under cyclic tensile testing. This can be seen in the representative specimen (**Fig. 3.6a**). The relaxation behavior is different depending on the specimen composition, and it generally decreases from SMP1 to SMP12. However, this decrease is not uniform and requires more data collection before any concrete trends relating to composition can be identified. Within individual specimens, the relaxation behavior followed a regular pattern (**Fig. 3.6a**), exhibiting large but decreasing relaxation during the first six cycles and then transitioning to uniform small relaxation during later cycles. The maximum reduction observed at the end of the tenth cycle was $26.9\% \pm 3.93\%$ for SMP1, while the minimum was observed to be $1.15\% \pm 0.04\%$ for SMP9. The elastic moduli of the SMPs were also affected by the cyclic loading, decreasing sharply during the first two cycles but remaining nearly constant after the fourth (**Fig. 3.6c**). The elastic modulus also varies with the SMP composition, with a gradual decrease from SMP1 to SMP12. SMP1 displayed the largest

elastic modulus with a value of $22.58 \text{ MPa} \pm 0.08 \text{ MPa}$, while SMP 12 displayed the smallest, with a value of $13.14 \text{ MPa} \pm 0.31 \text{ MPa}$ (**Table 3.5**).

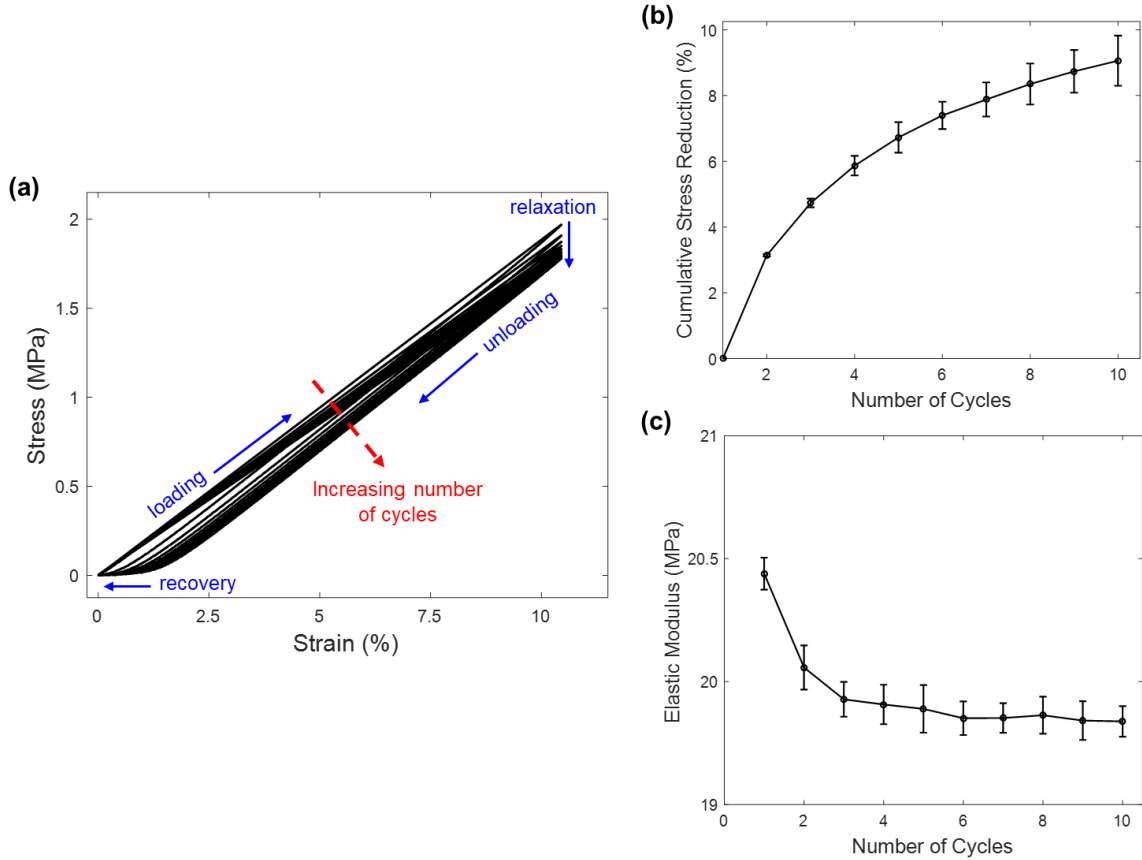


Figure 3.6: Representative cyclic mechanical testing results (SMP3) when tested at 50% of the observed failure strain ($T_g + 10 \text{ }^\circ\text{C}$) showing: (a) the relaxation trend in the peak stress with an increasing number of cycles, (b) the increase in the cumulative stress reduction and (c) the convergence of the elastic modulus with an increasing number of cycles.

Table 3.5: Failure stresses and failure strains from the uniaxial tensile failure testing (cf. **Fig. 3.5**) and the stress reductions and the calculated elastic modulus from the uniaxial cyclic tensile testing (cf. **Fig. 3.6**) for all the twelve SMP compositions. Tensile tests conducted at $T_g + 10$ °C.

	Uniaxial Tensile Failure Test		Uniaxial Cyclic Tensile Test		
	Failure stress (MPa)	Failure strain (%)	Cumulative stress reduction (%)		Elastic modulus at the 10 th cycle (MPa)
			2 nd cycle w.r.t. 1 st cycle	10 th cycle w.r.t. 1 st cycle	
SMP1	4.68 ± 0.23	26.5 ± 2.11	7.66 ± 0.42	26.9 ± 3.93	22.58 ± 0.08
SMP2	3.78 ± 0.21	22.1 ± 1.24	3.36 ± 0.98	7.88 ± 2.16	20.74 ± 0.52
SMP3	3.34 ± 0.16	16.2 ± 0.72	1.83 ± 0.59	9.08 ± 4.58	18.97 ± 0.33
SMP4	3.84 ± 0.07	20.9 ± 0.32	3.14 ± 0.03	9.06 ± 0.54	19.84 ± 0.04
SMP5	3.74 ± 0.22	25.3 ± 0.76	3.30 ± 0.62	8.39 ± 1.66	18.80 ± 0.82
SMP6	4.11 ± 0.17	28.7 ± 0.83	2.79 ± 0.03	6.64 ± 0.49	20.39 ± 1.48
SMP7	4.29 ± 0.11	30.9 ± 3.14	2.28 ± 0.29	5.68 ± 0.37	18.50 ± 0.18
SMP8	4.45 ± 0.43	31.6 ± 2.44	2.26 ± 0.25	6.70 ± 0.24	19.04 ± 0.77
SMP9	4.76 ± 0.28	32.7 ± 0.58	0.41 ± 0.12	1.15 ± 0.04	18.34 ± 2.12
SMP10	4.74 ± 0.14	36.5 ± 2.14	0.51 ± 0.09	7.42 ± 0.03	16.32 ± 0.52
SMP11	5.25 ± 0.55	43.2 ± 6.29	0.80 ± 0.47	1.92 ± 1.36	15.26 ± 0.25
SMP12	6.88 ± 0.29	54.4 ± 2.97	0.93 ± 0.06	3.34 ± 0.85	13.14 ± 0.31

3.3.5 Shape recovery capability

The SMPs showed a consistent temperature dependence in their shape recovery behavior, an example of which is shown in **Figure 3.7**. Among individual specimens, the SMPs showed a slower recovery response between the initiation of the test and the first 45° of recovery, a fast, linear response between 45° and 135°, and a nonlinear deceleration as it approached a full 180° recovery. The results of the recovery tests indicated no significant trends in the recovery time with relation to the SMP composition. There was a tendency for specimens with a high TEA content (closer to SMP12) to recover faster than

those with a high HPED content (closer to SMP1). However, several SMP compositions fell outside of this trend that it cannot be considered significant. **Figure 3.8** shows a direct comparison of the recovery test results at $T_g + 5\text{ }^\circ\text{C}$ among the three selected SMP compositions (SMP3, SMP7, and SMP11).

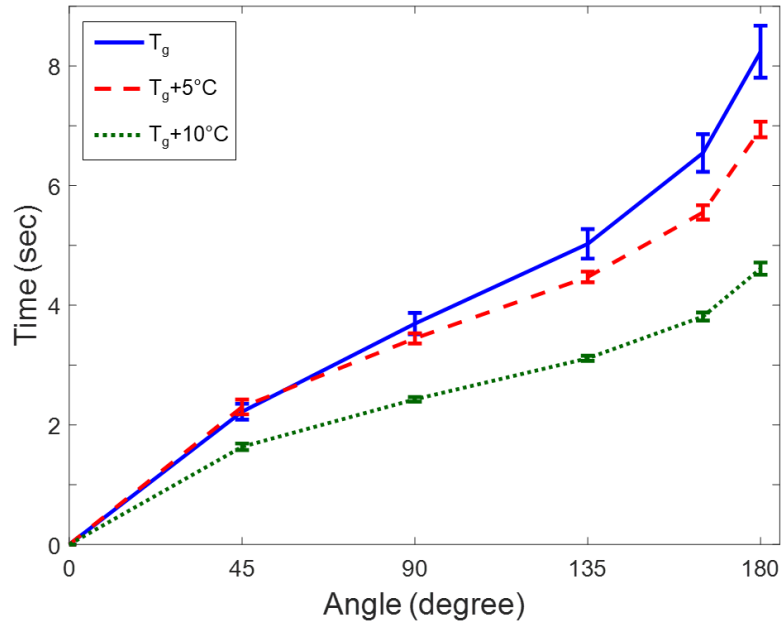


Figure 3.7: Mean \pm SEM of the recovery testing time for a representative SMP composition (SMP3, $n=3$) showing the consistent trend of reduced recovery time with an increased temperature.

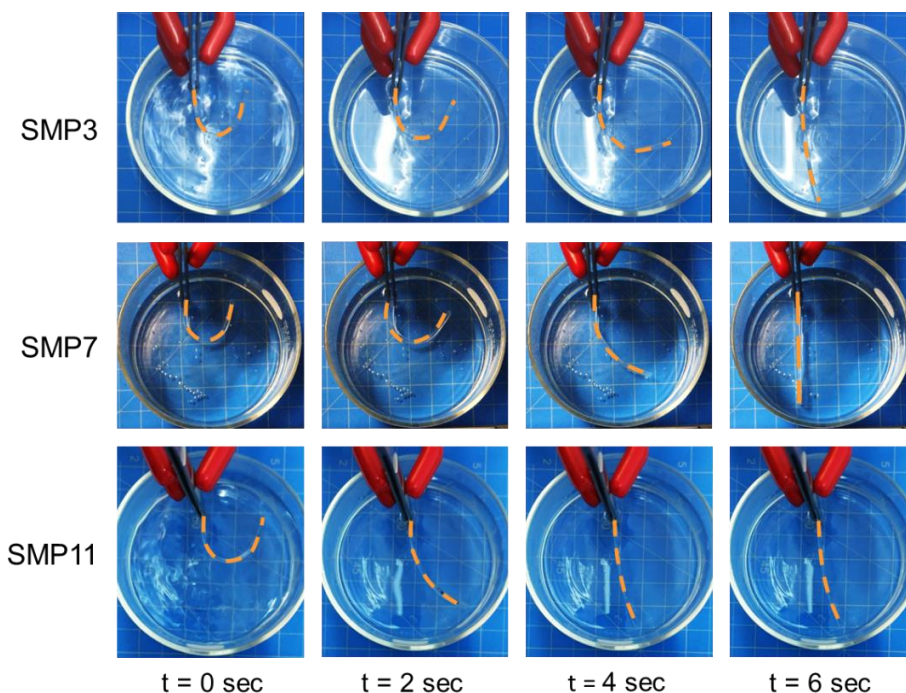


Figure 3.8: Experimental photos of the recovery testing for three representative SMP compositions (SMP3, SMP7, and SMP11) at defined time increments ($t = 0$ sec, $t = 2$ sec, $t = 4$ sec, and $t = 6$ sec), showing the observed trend of a decreasing recovery time with an increasing TEA content.

3.4 Discussion

3.4.1 Overall findings and relevance to endovascular embolization treatment for ICAs

The thermomechanical characterization of the aliphatic urethane SMPs provided a closer look at the shift in material properties that occurs as each SMP reaches its T_g . The DMA results showed a single sharp transition in the shear storage modulus for all compositions (**Fig. 3.2a**). We observed that this transition occurs at different temperature levels depending on the SMP composition, with higher glass transition temperatures corresponding to higher concentrations of HPED. In this study, the glass transition

temperature of the SMP specimen was determined from these transitions with SMP compositions tested, ranging from 83.2 °C to 32.3 °C. In the context of implantable embolic devices, the SMP needs to possess a T_g above body temperature (37 °C) but below the threshold for tissue damage (45 °C) [74]. If the T_g is below body temperature, then the implant would constantly exist in a malleable state and not hold any one specific shape; however, at temperature levels greater than 45 °C, bodily tissues can begin to take damage. This desired threshold falls within our observed T_g values, suggesting that we can synthesize an aliphatic urethane SMP by employing the techniques detailed in this study, which transitions at a temperature suitable for applications in the human body.

Moreover, uniaxial mechanical testing was conducted using the SMPs to determine their material strength and investigate how the strengths varied with composition. The failure test results suggested that higher values for both failure stress and strain occur in compositions with lower HPED contents, but the trend is nonlinear with significant variances at SMP3 (**Fig. 3.5**). Because of its irregular trends, this data will be difficult to use in a predictive manner, but it implies that there may be more complex changes associated with the SMP's composition than we previously expected. With a wider range of compositions and larger sample sizes for each composition, future studies could identify trends which could allow fabrications of SMP-based biomedical devices with specific material strengths.

Cyclic tensile testing was performed to investigate changes in the behavior of the SMP under repeated loading. The two major properties that we investigated were the elastic modulus and the peak stress value at 50% failure strain (**Table 3**). GDC-based coils are designed to be left in the body for the remainder of a patient's lifetime, so it is important

that the SMP materials used for this endovascular embolization application will not relax over time, resulting in the aneurysm recurrence. One behavior that the cyclic testing revealed was a noticeable reduction in the peak stress, with most of the reduction occurring during the first few cycles. This stress reduction reached a maximum value of $26.9\% \pm 3.93\%$ in SMP1 with respect to the first cycle, and the next highest values fell near the range of 8-9% for SMP2-SMP5. The relaxation behavior, which is not a desirable quality in the context of a permanent embolization device, was more pronounced for SMPs containing more HPED contents. The compositions containing large quantities of TEA contents exhibited less relaxation, reaching values as low as $1.15\% \pm 0.04\%$ for SMP9 and $1.92\% \pm 1.36\%$ for SMP11. However, due to a small sample size for our cyclic tests, we were not able to identify any quantitative relationship between the SMP composition and the stress relaxation behavior. In addition, the elastic modulus also varied with cyclic loading, but only during the first few cycles of the test. The elastic modulus values decreased sharply during the first cycle, but quickly reached a constant value around the third or fourth cycle (**Fig. 3.6a**). Even though the changes in elastic modulus are small, it is in our interest to minimize any changes in material properties once the SMP is introduced into the body. Since we were able to observe both the stress relaxation and elastic modulus approaching a stable point in the latter cycles of our tests, we expect that it would be necessary to design the embolization devices to undergo pre-cycling before implantation, minimizing the effects of initial relaxation when the device is administered.

Another important factor in designing an embolic device made from SMPs is the shape recovery behavior which occurs when the polymer transitions from a deformed state to its un-stressed state. The recovery tests conducted in this study focused on the time

required for the SMP to recover its shape. For endovascular embolization of ICAs, short recovery time of the SMP-based device is an important design criterion to avoid the prolonged heating of body tissues during device deployment. We showed the recovery behavior of the SMPs to be temperature dependent, speeding up as temperatures increased past the T_g . At $T_g + 10^\circ\text{C}$, with no composition taking more than 10.3 seconds to fully recover from a 180° bend. There was noticeable variation among different compositions, and it is very likely that a more complex relationship exists between the SMP composition and the polymer's recovery behavior. Such relationships are beyond the scope of this study and could be further investigated in the future. The quick recovery time displayed by all compositions is promising for our continued efforts toward the development of an improved aneurysm embolization device. If a device made using this SMP material could be intravenously moved to its target location and then reconfigured in a matter of seconds, it would have the ability to improve a great number of medical procedures.

3.4.2 Study limitations

This study featured a comprehensive set of thermomechanical characterization experiments, and as a result had a plethora of limiting factors that could have contributed to the variations in our data. The most prominent of these limitations is a relative smaller sample size for our cyclic tensile test, failure test, and recovery test. Two sets of data for each composition were taken during cyclic testing, and three were taken for each composition during failure testing. For the recovery tests, three trials were performed for each temperature point for each composition. The focus of this study was to conduct a broad analysis of aliphatic urethane shape memory polymers with varying SMP compositions. Consequently, we sacrificed the data statistical meaningfulness that comes

with a large sample size to instead survey a wide range of compositions for trends and patterns. As future extensions based on the results of this general characterization, we plan to focus on a single composition range and collect more thorough measurements to quantitatively define the trends observed in this study.

Within the uniaxial failure and cyclic tensile tests, there are several factors that could have affected our results. The samples that we used were all synthesized at the beginning of our testing period, and so it is possible that the ones that were tested later in the study could have changed over time as they were stored (e.g., absorbing moisture). This could be remedied by testing each composition at the same amount of time after synthesis to ensure age is constant. The samples were attached to the uniaxial tester using double sided tape to avoid slippage. Deformations in this tape layer or slight slippages on the adhesive could have resulted in skewed results. However, since all samples were tested the same way, the error due to this mounting method should be consistent. Small imperfections in the samples, such as bubbles or heterogeneity in the monomer mixtures, could have also resulted in differences between samples in a composition. These errors can be reduced as the synthesis procedure is perfected, and researchers should be careful to select only pristine samples for testing.

The recovery tests we conducted had many aspects that can be improved upon. Our measurement method relied on visual inspection to determine the angular position of the sample and the frame at which the position of interest was reached. From the frame analysis, we determined time elapsed. This entire measurement method is subject to human error in multiple places, which is difficult to account for. It would be beneficial to determine a more exact way to measure recovery. Some samples did not return completely

to a straight angle, and others began their deformation at an angle other than 180°. While the recovery times were still useful for our analyses, a study looking to definitively quantify the recovery response of these materials would need to better define the start and end conditions for the tests.

3.5 Concluding Remarks

This study aimed to characterize a range of compositions of aliphatic urethane shape memory polymers for their potential use in the treatment of intracranial aneurysms. In specific, we developed a detailed synthesis procedure for the SMPs to provide our study with a variety of compositions and inform future studies seeking to utilize the same material. We have investigated the thermomechanical properties including the glass transition temperature and thermal stability of each composition, and we have also found that compositions between SMP9 and SMP11 possess transition temperatures between body temperature and the threshold of tissue damage. This is the optimal T_g range for allowing the polymers to remain functionable within the body without causing any tissue damage due to the heating associated with shape change triggering. We have also found that within our desired operating temperatures, all SMP compositions are thermally stable regarding the endovascular embolization procedure. We have also characterized the mechanical properties of the SMPs and identified decreases in both maximum stress and elastic modulus with cyclic loading. Our results showed that in SMPs closer to SMP12, these decreases were not as prominent. Since any changes in material properties during the lifetime of an implanted device are detrimental, the SMP compositions near SMP12 are

more desirable in the context of endovascular embolization treatment for ICAs. Finally, we have tested the recovery time of each polymer and showed that all the SMP compositions are capable of recovering from a 180° bend within 10.3 seconds. Using knowledge from the broad characterization performed in this study, we have identified a range of compositions between SMP9 and SMP11 that most accurately meet our criteria with their great potential for the individualized treatment of intracranial aneurysms, and they will be analyzed further in more detail as a part of future studies.

CHAPTER 4: Shape Memory Polymer Foam Synthesis and Characterization

4.1 Introduction

Polymeric materials with suitable thermo-mechanical properties and functionality, such as biocompatibility, biodegradability, oxidative resistance and shape memory/recovery, are clinically desirable for biomedical applications. In the past decade, the advancement of polymer science has led to the development of shape memory polymers (SMPs) for use in the design of novel biomedical actuators, sensors, devices and smart systems [75-78], among others. SMPs can maintain a temporary shape when they are cooled below their glass transition temperature. Once appropriate thermal, electrical, or environmental conditions are satisfied, SMPs autonomously recover from this temporary shape to their original geometry without any external forces. This phenomenon is commonly referred as *shape memory and shape recovery*. It has been shown that the shape recovery and relaxation features of SMPs are associated with the intrinsic elastic deformation stored in their polymeric networks during prior manipulation [79-81]. In general, SMPs possess many desirable qualities for medical use: the ability to undergo large elastic deformation, low weight, low cost, an easily controllable synthesis procedure, and the potential for biocompatibility.

Several shape recovery activation methods for SMPs, including thermal energy [67, 82, 83], light [84, 85], and moisture [86, 87], have been reported in literature. In particular, thermally-induced shape recovery is the most popular method owing to the simplicity of

generating, applying, and controlling environmental temperature using laboratory equipment or other available heat tools under clinical settings. Vernon and Vernon published the first thermally-induced SMP in 1941, demonstrating that a dental material made of methacrylic acid ester resin possessed good elastic memory and was able to recover to its original shape after enough heat was applied [88]. By now, thermally-induced SMPs include polyurethanes [82, 89], polyetheresters [90, 91], polynorbornene [75, 92], and poly(styrene-block-butadiene) [93, 94]. Nanoparticles, such as carbon nanotubes and graphene oxide, have been dispersed within SMPs to fabricate shape memory nanocomposites for biomedical applications [95-97]. More detailed information about emerging SMP formulations and synthesis methods can be found in recent review papers on SMPs [98-101].

Novel medical devices that take advantage of the unique properties of SMPs have been developed in the last decade that include clot removal devices, intracranial aneurysm (ICA) occlusion devices, and vascular stents [75, 76, 102]. Most reported SMP-based medical devices were thermally activated, either directly through a heating element, or through photo-thermal and electrical-thermal approaches. Aneurysm occlusion devices have been one of the most popular applications for biocompatible SMPs. As the current gold standard of intracranial aneurysm treatment, endovascular embolization using Guglielmi detachable coils (GDCs) aims at complete and lasting occlusion [63, 102, 103]. However, long-term treatment outcomes of the GDC-based neurosurgery have been shown to be less satisfactory than expected: The recurrence rate of completely embolized aneurysms could approach 41% within 3-5 years of initial therapy, with 26% of those requiring retreatment, increasing health care burden [62, 104]. SMP materials could present

an alternative approach to GDC-based endovascular coil embolization, since their unique shape recovery property allows for a similar style of deployment and occlusion. SMP foams in particular are of interest because of their easily controllable porosity, which allows for consistent volume fill ratios, a property that varies for coil embolization [105].

Since a wide variety of materials fall under the SMP label, the current materials under investigation for SMP embolization treatments are quite diverse. Materials, including polypropylene glycol, polyether polyol polyurethane, epoxy, and aliphatic polyurethane, have been used to synthesize SMP foams with varying mechanical properties [106-109]. An open-cell porous polyurethane SMP material referred to as Cold-Hibernated Elastic Memory (CHEM) foam has been investigated for the fabrication of aneurysm occlusion devices. Metcalfe *et al.* reported a series of experimental investigations and an animal study using SMP foams for aneurysm treatment [36]. Their results showed that the open cellular structure of the SMP foams increased the growth of cells in neointima formation. Further biocompatibility studies performed by Farè *et al.* (2005) showed that the material has good compatibility with human fibroblasts despite having a low affinity for platelet adhesion. In addition to aneurysm treatment, Sokolowski *et al.* (2007) suggest that this material could be used for thrombus removal, arterial grafts, braces, splints, prosthetics, implants, and both soft and hard tissue engineering scaffolds. Recently, low-density aliphatic polyurethane SMP foams manufactured with a chemical blowing process have been used to create uniformly-shaped embolization plugs, which demonstrated stable thrombus formation and complete endothelialization of the aneurysm neck within 90 days [35]. The same polyurethane SMPs have been applied as a coating on platinum coils in a modified version of coil embolization, delivering promising results through in in-vitro

experiments and in-vivo animal studies [35, 46, 110]. However, even with SMP-enhanced coils, the risk of coil compaction and aneurysm recanalization still present clinical and technical challenges due to resorption of the polymer coating.

In this Chapter, we present the synthesis procedures and characterization of an SMP foam created using a sugar particle leaching technique. The synthesis method used in this study enables fine control over both the pore size and the density of the synthesized porous foam—a characteristic which could enable tunable mechanical properties such as stiffness and compression ratio for device design applications. The porous microstructure of the SMP foam was characterized using both scanning electron microscopy (SEM) and micro computed tomography (μ -CT). We also report our experimental procedures for the characterization of the foam for a certain range of pore sizes and a single monomer composition. Although the testing in this study was conducted on a single group of identical samples, both the pore size and monomer composition can be judiciously adjusted during synthesis to achieve desired mechanical and thermomechanical properties respectively [111]. The mechanical performance of the synthesized porous SMP was evaluated up to 10 °C above the SMP's glass transition temperature using uniaxial compressive loading. Finally, we demonstrate a potential deployment method using a group of resistively heated carbon fiber filaments within compressed SMP foam to raise its temperature and activate shape recovery.

4.2 Materials and Methods

4.2.1. Materials

In this study, the following three monomers were used to synthesize aliphatic polyurethane shape memory polymers: (i) Hexamethylene diisocyanate (HDI, $\geq 99.0\%$), (ii) N,N,N',N'-tetrakis (hydroxypropyl) ethylenediamine (HPED, $\geq 98.0\%$), (iii) Triethanolamine (TEA, $\geq 99.0\%$). The monomer content percentages by weight of HDI, HPED, and TEA used for all synthesis reactions were 60.7%, 10.6%, and 28.7%, respectively [70, 111]. All the materials were purchased from Sigma Aldrich.

4.2.2. Preparation of solid and porous SMP materials

To synthesize solid, or pristine, SMPs, HDI, HPED, and TEA were first measured in the weight ratio described above and mixed using a high-speed shear mixer for 5-6 minutes, and then cast into their ASTM D638 Type V dog-bone or 45 mm by 8 mm by 1 mm rectangular molds for curing. The materials were degassed three times and protected under a nitrogen environment before and during curing using a vacuum oven (Being BOV-20). The temperature profile was first kept at room temperature for an hour, followed by a ramp of 9.6 °C per hour up to 130 °C, then held for 1 hour at 130 °C, and finally cooled back to room temperature. The fully cured SMP samples were removed from the molds, sealed in vacuum bags, and stored in a vacuum desiccator (Bel-Art Lab, SP Scienceware) to ensure no moisture contamination occurred before subsequent thermomechanical characterization experiments [112].

Novel highly-porous SMP foams were synthesized using a sugar particle leaching method, as depicted in **Figure 4.1**. In brief, sugar templates in the shape of cubes and thin

sheets were first manufactured by compressing an appropriate amount of pure cane sugar (Florida Crystals, Inc.), purchased from local food store, into a silicon rubber mold. The average sugar particle size was measured using scanning electron microscopy and was found to be about 500 μm . A slight amount of water was added with granulated cane sugar to improve the formability and sugar's interfacial bonding. The water was lightly misted onto the surface of a spatula using a spray bottle, and then stirred into the mixture. This step was repeated until the sugar grains were observed to stick to one another when scooped with the spatula. The sugar was then compressed into a mold and dried in a vacuum oven at 130 °C for two hours.

Once the sugar templates were prepared, the 3 monomers with the above-mentioned content percentages were measured and mixed by a high-speed shear mixer for 5-6 minutes. The sugar templates were then merged into the mixed monomer solution and were kept in vacuum in a freezer at -5 °C for 24 hours. The monomers completely infiltrated through the sugar template, partially reacted, and were then post-cured following the heating procedure as previously described for curing the solid SMP specimens. The fully-cured SMP/sugar templates were next merged in de-ionized (DI) water and kept in a bath sonicating for 1 hour to fully dissolve all the cane sugar. The manufactured porous SMP samples were kept in a vacuum oven at 50 °C for 24 hours to fully eliminate all the humidity trapped in the foam, and then stored in a vacuum desiccator before subsequent experiments.

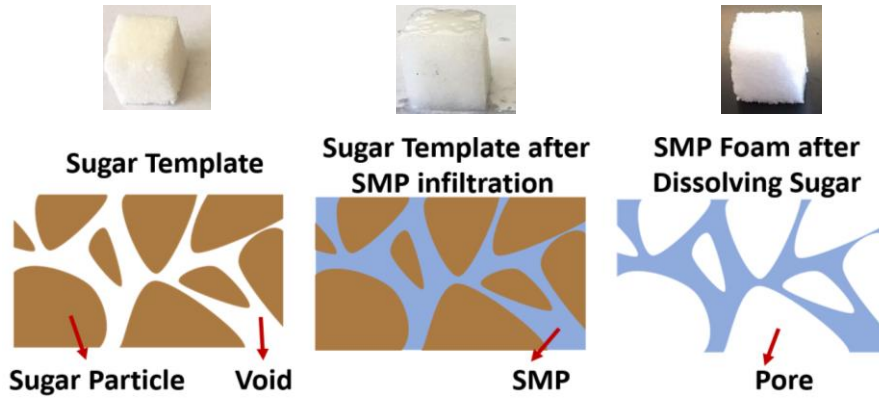


Figure 4.1: Schematic of the sugar particle leaching method for fabrication of the porous SMP foam.

4.2.3. Shape Recovery Characterization

The T_g of the synthesized SMP has been characterized using standard dynamic mechanical analysis (DMA; TA Q800, TA Instruments) and differential scanning calorimetry (DSC; TA Q50, TA Instruments) tests. The detailed DMA and DSC characterization procedure and results have been reported in our previous study [111]. The shape recovery capability of the synthesized porous SMP material was also qualitatively and quantitatively investigated using a direct heating method. The SMP foam sample was first heated on a hot plate at 70 °C for two minutes, compressed, and cooled back to room temperature in air. Then, the sample was placed on a hot plate with a surface temperature of 70 °C again to investigate its shape recovery process.

4.2.4 Investigations of Microstructural Morphology

Following previous studies in literature [113, 114], the porosity of the SMP foam was roughly estimated using Eq. (4.1).

$$Porosity = 1 - \frac{\rho_{porous\ SMP}}{\rho_{solid\ SMP}}, \quad (4.1)$$

where $\rho_{\text{solid SMP}} = M_{\text{solid cube}}/V_{\text{cube}}$ and $\rho_{\text{porous SMP}} = M_{\text{porous cube}}/V_{\text{cube}}$ are the “apparent densities” of the solid SMP cube (10 mm by 10 mm by 10 mm) and the porous SMP cube, respectively. The masses of both the solid and porous SMP specimens were measured by digital scale and the volume was determined based on the dimensions of the cube. Ten samples were measured for both solid and porous SMP to guarantee accuracy and repeatability.

The microstructure, pore size, and porosity of the porous SMP were characterized by a TESCAN SEM system. The synthesized SMP foam was first sputter coated to improve the surface conductivity and prevent charging before taking the SEM images. SEM images were taken from the top surface and the cross-section in the middle of the cubic SMP foam samples. To include enough pores in each SEM images, relatively low magnification of 50-100 times were used for all obtain SEM images. The SEM images were analyzed using ImageJ software (National Institute of Health, Bethesda, MA) to obtain the average pore size at different levels in the foam.

In addition to SEM-based quantification of the microstructure of the manufactured SMP foams, a commercial, high-speed, Quantum FX μ -CT system (Perkin Elmer Co., MA, USA), equipped with a micro focus X-ray tube with tungsten target and a flat panel detector, was used to non-destructively image and quantify the 3D microstructural morphology of the synthesized SMP foam samples. The X-ray tube and the detector at the μ -CT system were placed opposite to each other on a gantry that rotates in a counter clockwise around the bed on which the object was placed.

The samples were scanned with an X-ray power at 90 kV and 200 μ A, a source object distance (SOD) of 265 mm, a distance to patient of 154 mm, an exposure time of

180 seconds, and the field of view (FOV) of 30 mm x 30 mm on the object plane, resulting in a 59 μm resolution with isotropic voxels (512x512). Image segmentation and 3D geometry reconstruction of the acquired DICOM image data was then performed in Amira software (FEI Inc.) to render the 3D morphological structure. A few representative pores from the 3D images obtained in the CT scan were used to estimate pore-size and roughly cross-check results from the SEM imaging but were not used in any quantitative analysis of the pore size.

4.2.5 Electrical Resistance Deployment Investigation

Electrically heated carbon fiber filaments were used to simulate a potential deployment configuration for the SMP (**Fig. 4.2a**). An arbitrarily sized 10 mm by 10 mm by 15 mm SMP sample was synthesized according to the procedures described above and a bundle of carbon fibers was introduced through the center of the sample using a needle, resulting in a foam sample with a simple integrated heating element. The foam was heated above its T_g and compressed manually, and then cooled at room temperature to fix the temporary compressed shape. Direct current (DC) at 0.5, 1.0, 1.5, and 2.0 amperes was applied on the carbon fiber wires to generate the required heat and trigger the shape recovery of the compressed SMP foam, by using an electrical resistance heating method. The electrical heating was current controlled, and due to the high conductivity of the carbon fibers used in this test, applied voltages were 0.2 Volt and 0.8 Volt. The surface temperature was measured using an infrared (IR) camera every 10 seconds, and thermal images were captured at each time point for illustration. The electrical resistance heating speed and magnitude were quantified by controlling the electrical current applied to the porous SMP samples.

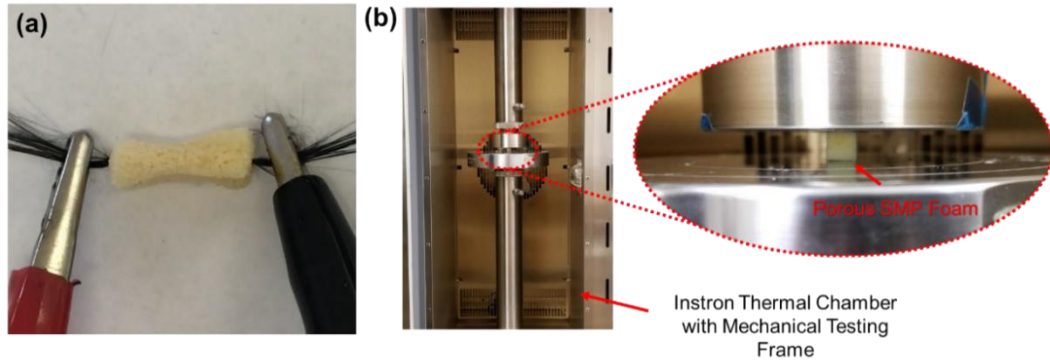


Figure 4.2: (a) Experimental photo of the electrically heated procedure to activate the shape recovery of the SMP foam using carbon fiber wires. (2) Image of the experimental setup in thermal chamber for mechanical characterization of the SMP foam.

The mechanical behavior of the porous SMP samples was characterized using an Instron 5969 dual-column mechanical testing system integrated with an environmental chamber (**Fig. 4.2b**). Cubic SMP foam samples (10 mm by 10 mm by 10 mm) were first tested until failure at room temperature ($n=3$), then the failure strain was used to conduct cyclic compressive testing up to 40% of the failure strain ($\sim 90\%$) at a rate of 2 mm/min. Key mechanical properties were measured under 10 compressive load cycles at room temperature ($25\text{ }^{\circ}\text{C}$, $n=3$), T_g of SMP foam ($39\text{ }^{\circ}\text{C}$, $n=3$), and $T_g + 10\text{ }^{\circ}\text{C}$ ($49\text{ }^{\circ}\text{C}$, $n=3$). All the samples were pre-heated in the environmental chamber at the required temperature for 30 minutes before any mechanical tests.

4.3 Results and Discussions

4.3.1 Shape memory and recovery features of the synthesized SMPs

DMA tests showed the T_g of synthesized SMP was 37.2 °C, and DSC tests showed the T_g was 39 °C. It is typical to see a slight difference between DSC and DMA tests due to the different testing mechanisms. Since the developed SMP is being designed to treat aneurysms as a biomedical device, the obtained T_g slightly above normal body temperature is optimal and appropriate when designing a device that can deploy without causing tissue damage [74, 115].

As shown in **Figure 4.3**, the SMP foam started recovering from the compressed shape after 10 seconds. In 50 seconds, the shape of the SMP foam was completely recovered back to a normal cubic shape. The fast shape recovery demonstrates that the synthesized SMP foam has the potential to quickly recover from a large deformation, making this SMP material a desirable candidate for the design of catheter-deployed embolization devices. When the SMP is placed on a hot plate set to the range of 38-45 °C required for endovascular embolization procedure, we observed that the compressed SMP foam can fully recover to its original shape within two minutes. This simplified test was performed in an open-air lab environment without controls for humidity.

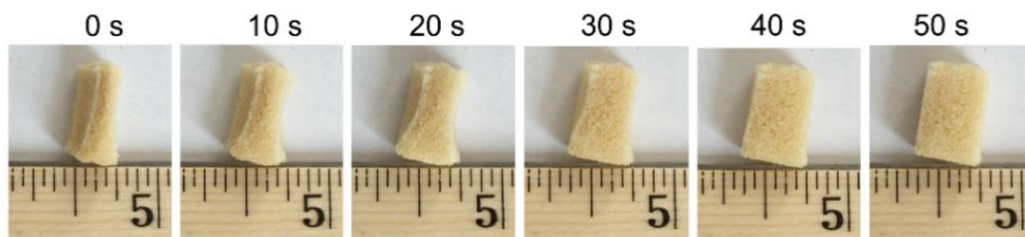


Figure 4.3: Progression of the shape recovery process of the compressed porous SMP foam in response to direct heating above the SMP's T_g .

The shape memory function of solid SMP with the same composition was also investigated. Each straight beam sample was immersed into hot water (5-10 °C above the expected glass transition temperature), bent up to 180°, and cooled back to room temperature while maintaining the bent shape. Then the SMP sample was placed back to hot water and the material was allowed to return to the initial straight form autonomously. Qualitatively, the pristine solid SMP samples were much more compliant in bending than in either tension or compression. The high degree of flexibility in bending is illustrated in **Figure 4.4**. Qualitative analysis showed that the foam samples were more difficult to bend without tearing but exhibited a greatly increased compressibility in comparison with the solid SMP beams.

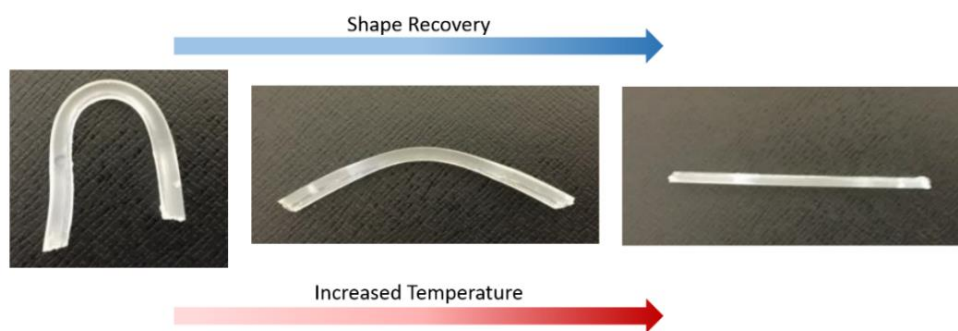


Figure 4.4: Shape recovery of the bent solid SMP beam (temporary shape) into the originally programmed straight shape after heating above the SMP's T_g .

A significant difference in color was observed between the pristine solid SMP and the porous SMP. While the pristine solid SMP was primarily transparent (**Fig. 4.4**), turning white with sanding after synthesis, the SMP foam turned a beige-yellow color during preparation. Yellowing of polyurethane foam is a common occurrence that can result from any combination of three typical causes. The first type of yellowing occurs because of the formation of quinones (yellow in color) after exposure to UV light. This reaction primarily occurs in polyurethanes synthesized with aromatic isocyanates, and ours uses aliphatic isocyanates, so we do not suspect that this reaction is present. The second type of yellowing occurs when the foam is oxidized by gasses (usually nitrogen oxides or ozone), and the third type of yellowing occurs when the foam is exposed to high heat [116].

During synthesis, we noticed a decrease in yellowing when we performed the reactions in a pure nitrogen environment versus air, and when we lowered the temperatures used to dissolve sugar and dry the foam. The yellowing that still occurs is likely due to the heat used during our sugar dissolution and drying procedures, since we do not believe there is a significant source of oxidative gas during synthesis. There is also the possibility of an unforeseen interaction between the SMP monomer and sugar that occurs before curing, contributing to the change of surface color.

4.3.2 Microstructural analysis

Comprehensive microstructural quantification of the synthesized SMP foam was carried out to understand the foam's properties. The fabricated SMP foam was examined using SEM to measure the average size of open pores, which was a critical parameter to evaluate the density and compression capability of the synthesized SMPs foam. More than 10 SEM images were taken from either the top of SMP foam or the cross-section cut in the

middle of SMP foam. The typical SEM images were shown in **Figure 4.5**. The average pore size is about 480 μm . No sugar particles were observed in any of the acquired SEM images, indicating the complete removal of cane sugar during the sonication process.

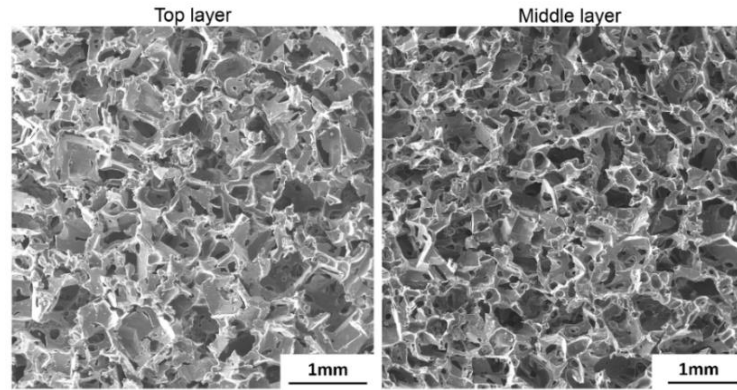


Figure 4.5: SEM images taken from the top layer and the middle layer of the porous SMP foam fabricated using the sugar particle leaching method, showing the open-cell structure of the foam.

On the other hand, representative 2D and 3D $\mu\text{-CT}$ images of entire porous SMP foam are shown in **Figure 4.6**. The 2D $\mu\text{-CT}$ scans were carried out on $x\text{-}y$, $x\text{-}z$, and $y\text{-}z$ plane individually. The typical pore size is shown in the 2D $\mu\text{-CT}$ images, and generally agrees with the measurements obtained through SEM imaging. The slides of 2D $\mu\text{-CT}$ images were compiled to create the 3D $\mu\text{-CT}$ image, as shown in **Figure 4.6c**. The 3D images can be used for future computational modeling and optimization of the porous SMP forms.

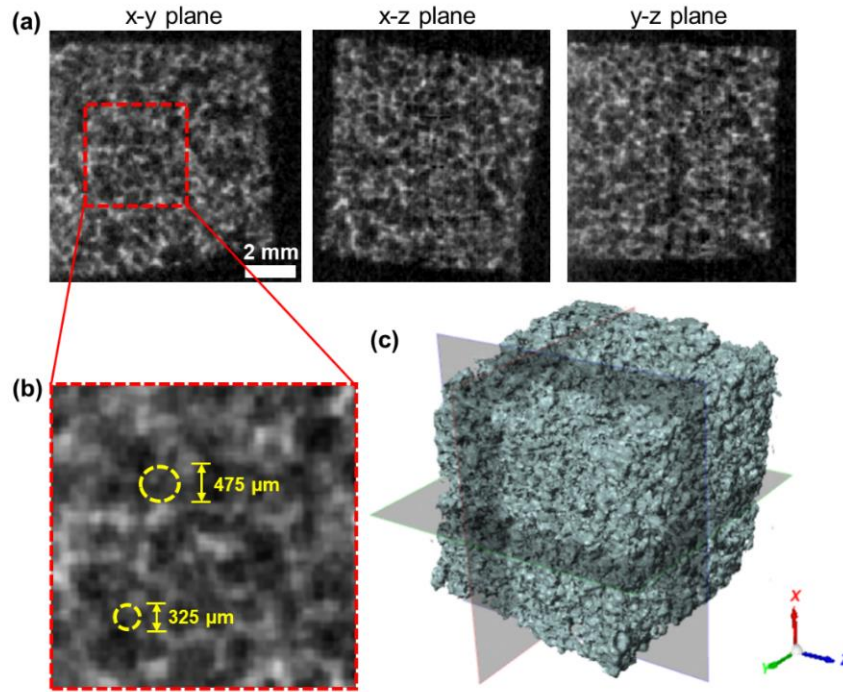


Figure 4.6: μ -CT images showing the microstructure of SMP foam: (a) 2D image slices on orthogonal planes, (b) zoomed-in area of the 2D image slice on the x - y plane, demonstrating the typical pore sizes of the SMP foam, and (c) the visualization of the reconstructed 3D geometry of the cubic SMP foam (10 mm by 10 mm by 10 mm).

The average density of solid SMP was 1.172 g/cm^3 , and the average density of porous SMP foam was 0.168 g/cm^3 . Therefore, the average porosity of the 10 measured SMP foam samples ($n=10$) was 85.7%. It is expected that this high porosity will allow significant elastic deformation of SMP at temperature above T_g , which can allow for the delivery of embolic devices for the treatment of a wider range of aneurysm sizes.

4.3.3 Electrical resistance heating-based SMP triggering method

An appropriate triggering method is necessary to successfully deploy highly compressed SMP foam for aneurysm occlusion application. Electrical resistance heating

was used in this study due to the ease of implementation for the potential surgical applications. Although minimal DC is preferred to improve patient safety in the surgical environment, it is noted that the SMP sample was not able to reach the required T_g when 0.05 A and 0.1 A DC were applied during the electrical resistance heating process, as shown in **Figure 4.7**. The equilibrium temperature measured on the SMP surface was 25.7 °C and 31.3 °C when 0.05 A and 0.1 A DC were applied. Once the applied DC current increased up to 0.15 A, the entire SMP temperature was able to increase above the T_g of the fabricated SMP foam within 120 seconds. The measured equilibrium surface temperature on SMP sample was 43.2 °C and 47.8 °C when 0.15 and 0.2 A DC were applied, respectively. Since human brain can be permanently damaged from short exposure to temperatures above 45 °C [74, 115], the optimal DC is selected to be 0.15 A for this particular test. More detailed fine tuning of the applied DC can be carried out at the stage of *in vitro* study and fine-tuned again before *in vivo* study, so that the required T_g of SMP can be quickly achieved and the deployed SMP temperature is still kept in the safe range for surgical applications. It is worth noting that although the heating element operates with very low voltages, the currents investigated in this demonstration have the potential to seriously harm the patient in a treatment scenario without the proper safety considerations in place. The present demonstrated deployment technique is merely intended to prove the possibility of SMP deployment around a heating element rather than proposing an application-ready prototype. The progression of the SMP's shape recovery during a 0.15 A DC deployment trial is illustrated in **Figure 4.8** along with a visualization of the sample's surface temperature measured using an infrared (IR) camera.

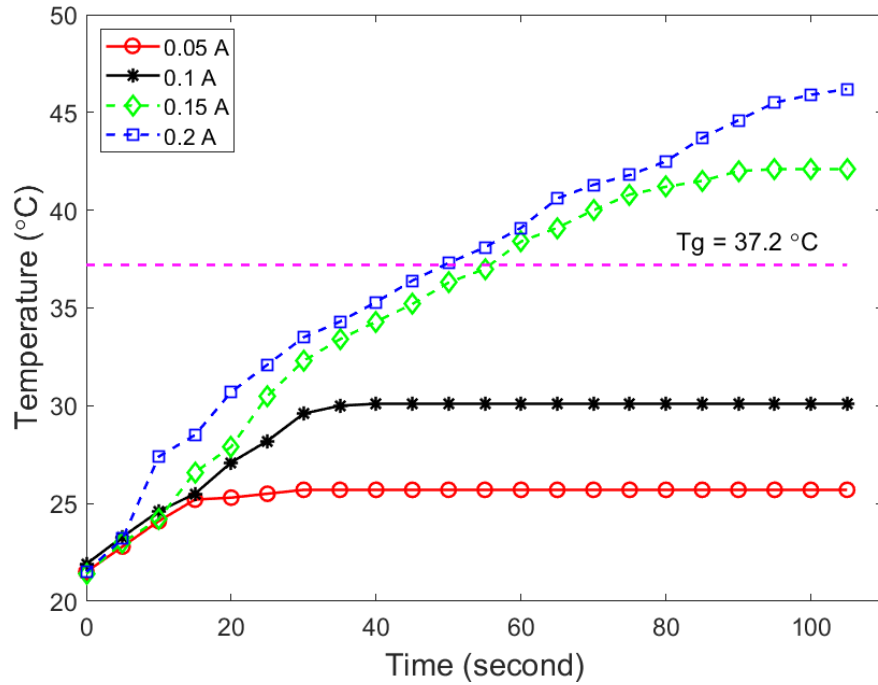


Figure 4.7: Surface temperature of the SMP foam specimen at various applied electric current magnitudes during electrical resistance heating.

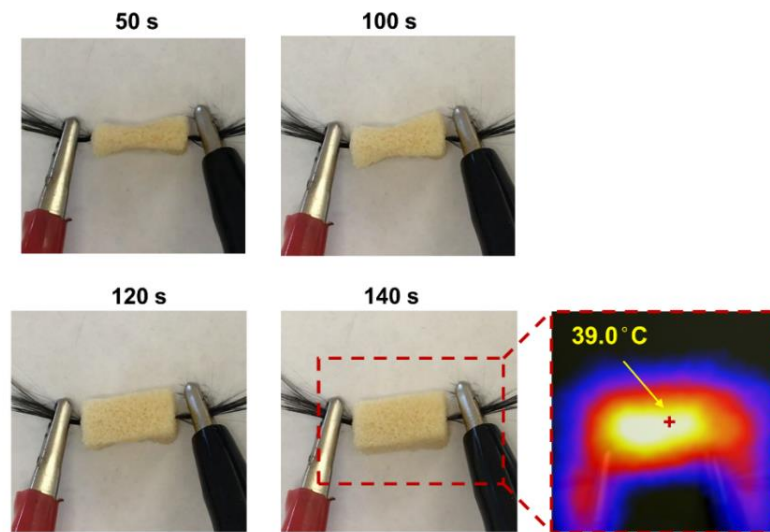


Figure 4.8: Experimental photos of the shape recovery process of the compressed SMP foam under 0.15 A DC, along with the measured surface temperature profile via an IR camera at 140 seconds after the applied electric current.

4.3.4 Mechanical characterization of SMP foam under compressive load

At room temperature (25 °C), the foam samples were compressed until a clear shear fracture appeared near 90% strain. This value was taken as the failure strain, and 35% compressive strain (~40% failure strain) was used for the following cyclic tests. Permanent plastic deformation was observed at room temperature after the loading/unloading compressive tests up to 35% compressive strain, as shown in **Figure 4.9a**. The measured elastic modulus was 2.7 ± 0.12 MPa at room temperature. However, the SMP foam was significantly softened after increasing the polymer's temperature to its T_g or higher. The measured elastic modulus of the SMP foam was 0.23 ± 0.017 MPa and 0.18 ± 0.012 MPa at 39 °C and 49 °C, respectively. This mechanical behavior of the SMP foam is critical to its potential role in aneurysm occlusion because the softened SMP foam has a reduced risk of rupturing the diseased blood vessels during deployment in an endovascular aneurysm embolization treatment. The elastic modulus values for the foam in this study generally agree with the properties of foams made with CHEM polyurethane foam (2.69 MPa at room temp., 0.064 MPa above T_g) and polyether polyol-polyurethane (5 MPa at room temp., 0.1 MPa above T_g) [106, 109]. For both of these other materials, the SMP foams were tested at $T_g + 30$ °C as opposed to $T_g + 10$ °C. This could account for the lower elastic modulus values above T_g .

In addition, cyclic compressive tests were used to evaluate the level of strain recovery for shape memory applications. A comparison of the results from compression testing at T_g and at 10 °C above T_g is shown in **Figure 4.9b-c**. SMP foams tested at these two temperature levels showed initial hysteresis in the first loading/unloading cycle, which could be attributed to residual stress, material relaxation, or the re-arrangement of dangling

chains and side-groups in the polymer. Once the SMP had been fully compressed and relaxed after the first cycle, the hysteresis became relatively insignificant. In addition, the cyclic compressive loading continuously softened the SMP foam, reducing the maximum achievable stress at any given strain. Interestingly, such reduction in the maximum achievable stress was also observed in the cyclic tensile testing of the dog-bone solid SMP specimens from our previous study [111], whereas more nonlinear stress reduction was found in our previous cyclic tensile tests. For example, at 35% applied strain, the measured stress kept reducing after each loading cycle, indicating the potential degradation of mechanical properties of the synthesized SMP foam. This mechanical behavior will be used to guide the future design and fabrication of compressed SMP foam as the core component in the intracranial aneurysm treatment.

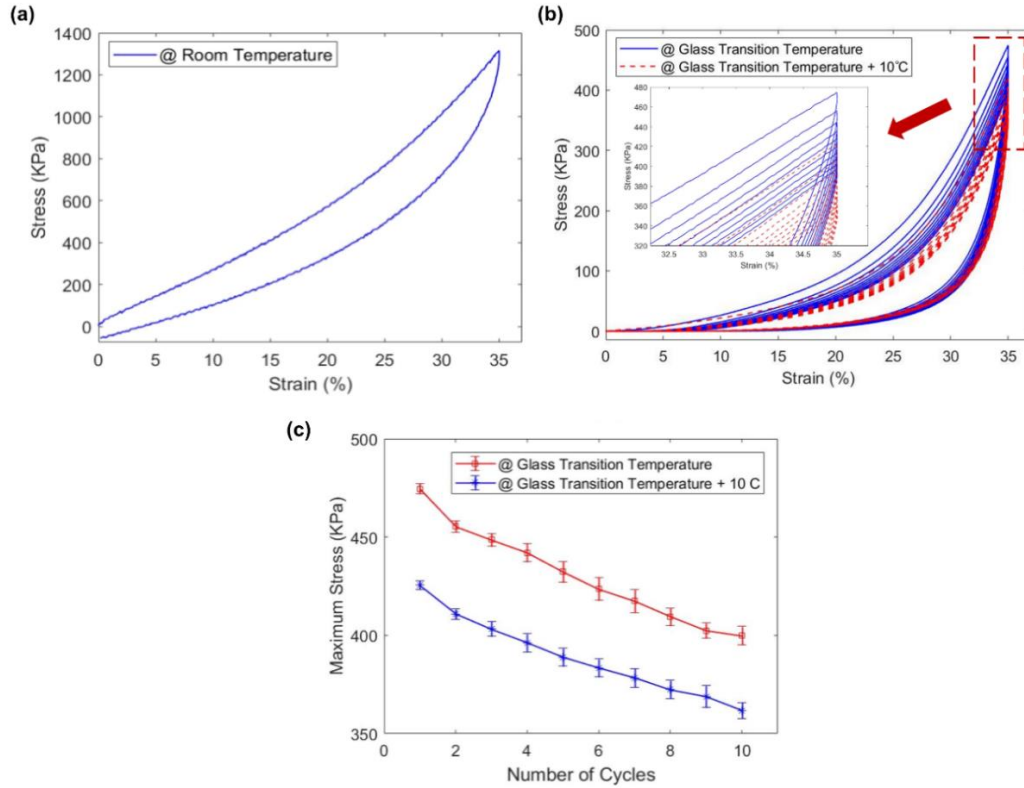


Figure 4.9: Mechanical characterization of the fabricated SMP foam under cyclic compressive load conditions: (a) typical mechanical response of the SMP foam at room temperature, (b) representative mechanical response of the SMP foam at T_g and $T_g + 10^\circ\text{C}$ under cyclic compressive loading, and (c) comparison of the maximum stress at 35% strain for various loading cycles at T_g and $T_g + 10^\circ\text{C}$. Values are reported as mean \pm SEM (standard error of the mean; $n=3$).

4.4 Concluding Remarks and Study Limitations

In this study, a novel SMP foam has been developed using aliphatic polyurethane SMPs, and it has been shown to possess the predicted shape memory function and properties comparable with other similar SMP foam materials. A sugar particle leaching

method has been employed to synthesize the porous SMP foam, introducing a new method for manufacturing a foam using an SMP material that is already of interest for aneurysm treatment applications [30]. Qualitative observations have been made to confirm that the synthesized SMP foam is capable of complete shape recovery within a minute of heating past its T_g . The structural properties, such as the average pore size and porosity, have been characterized and found to be uniform in nature. The three-dimensional structure of the material has been recorded using μ -CT techniques, which can enable future investigations into computational modeling and simulations of the SMP foam's thermo-mechanical and viscoelastic behaviors. Moreover, an electrical resistance heating method has been employed to activate the shape recovery behavior of the polymer. The relationship between the applied DC current and the surface temperature of SMP foam has also been examined for more precise control of the shape recovery behavior. Mechanical property characterization of the synthesized SMP foam both at room temperature and above T_g demonstrates that the material behaves comparably with other polyurethane SMP foams being considered for potential applications in the intracranial aneurysm occlusion. Since fracture was observed at 90% compressive strain, further investigations will need to be conducted to increase the compressibility of the foam if the material is going to be optimized for the design and use in endovascular applications.

There are several assumptions or limitations of this study. First, the monomer content percentages were chosen, according to our previous work [111], to synthesize SMP's with a glass transition temperature of ~ 39 °C which is ideal for endovascular embolization treatment. However, there are many different composition possibilities that result in different T_g values and different mechanical properties. Future investigations

could benefit from characterizations that determine how changes in composition affect the properties of the foam.

Secondly, the grain size of cane sugar used in this study, which predominantly governs the pore size of the fabricated SMP foam, varied from 250 μm to 550 μm . Future investigations may be warranted on the sugar grain size effect and the SMP-sugar ratio to establish a standardized procedure for fabricating SMP foams with tunable thermo-mechanical performance associated with targeted porosity and pore density.

Third, the recommended electric current of 0.15 A, conducted through the carbon fiber wires as a heating element, was determined based on an SMP foam size of 10 mm by 10 mm by 15 mm. A different electric current magnitude may be needed for a different foam size or a different specimen shape, and a more in-depth investigation of heat transfer through the SMP foam may be needed to properly control device deployment. This current was also determined based solely on the heating response it produced outside of a physiological setting without taking patient safety into consideration. Further designs will need to take medical regulations into careful consideration and incorporate safety measures to avoid damaging surrounding tissue via either electric shock or excess heat generation. More refined procedures for deployment are currently under investigation in our labs.

Finally, moisture has been shown to decrease the T_g of polyurethane shape memory polymers, which is an effect that could have major implications for applications in the human body [46]. All the mechanical characterization tests in this study were conducted in a standard lab environment open to the air with efforts taken to minimize moisture uptake between synthesis and testing. The water content of the porous SMP after drying was not quantified, but all drying steps were performed identically to normalize any effects of

residual moisture. Future tests in an environment more representative of endovascular conditions are warranted if this material is to be used in the occlusion of aneurysms. Nevertheless, this work renders a solid foundation to demonstrate the great potential of the developed aliphatic polyurethane SMP foam for the design of novel embolization devices which offer consistent and controllable volume fill ratios during intracranial aneurysm treatment.

CHAPTER 5: Additive Manufacturing Using Polyurethane

Shape Memory Polymers

5.1 Introduction

As computer integrated design processes become more prevalent in industry and research, manufacturing techniques must also evolve to keep pace with the complexity that is allowed by computer-aided design (CAD) software. Manufacturing processes for the 3D models that are typically produced by CAD software can be defined in three categories [117]. The first of these categories is forming, in which a fixed quantity of material is manipulated and deformed to take a desired shape. The second category is subtractive manufacturing, in which mass is removed from a large piece of stock material and the desired part is left behind at the end of the process. Subtractive manufacturing includes many well-known processes that can be observed in a machine shop type of environment such as mill and lathe-based manufacturing methods. Computer integrated CNC mills offer a subtractive manufacturing option that interfaces more directly with models generated using CAD technology. Additive manufacturing encompasses all manufacturing methods that add mass to construct a desired part, and often requires an automated motion component to replicate geometries from the CAD software with enough resolution [118].

Additive manufacturing is often referred to colloquially as 3D printing because of the layer-by-layer printing methods that remain a staple of most additive manufacturing techniques. Since most 3D printing techniques require adhesion between layers of material, the material selection can completely change the technology required to create an object.

While thermoplastic polymers often exhibit low melting temperatures, making heated extrusion a desirable option, most high strength metals exhibit prohibitively high melting temperatures, making a similar process too energy intensive to be practical. A similar problem arises for thermoset polymers, which will degrade before they melt and therefore become difficult to implement in a similar manner to thermoplastics. As the demand for additive manufacturing expands to more industries, the demand for new, potentially problematic materials grows with it. The result of this growing demand is a growing selection of 3D printing technologies that accommodate the manufacture of previously incompatible materials. The present study sought to develop an additive manufacturing device that was compatible with a thermoplastic polyurethane shape memory polymer (SMP) that is being investigated for its applications in medical device design. With this goal in mind, a few of the most popular additive manufacturing methods were selected for consideration.

In today's market, the most common commercially available 3D printing technology is known as fused deposition modeling (FDM) utilizes a filament, most often made from a thermoplastic, and a heat source to deposit material [118, 119]. In this method, the filament is driven through an extruder head using a mechanical feed system. The extruder head is heated above the melting temperature of the material, which exits the head in a viscous state. The extrusion head is positioned in three-dimensional space using one of many types of motor-controlled frames. The most common arrangement for the motion component of an FDM printer uses a cartesian coordinate system with servo-driven belt systems for the X, Y, and Z axes. The extruder head deposits a layer of filament on the X-Y plane, then is raised incrementally in the Z-direction to deposit the next layer of the print

on top of the first. **Figure 5.1** shows a simplified schematic of this type of FDM printing system. The resolution of FDM printers is determined by the height of the Z-axis increments as well as the width of the extruded filament. Smaller increments result in a more detailed print but come at the cost of increased printing time.

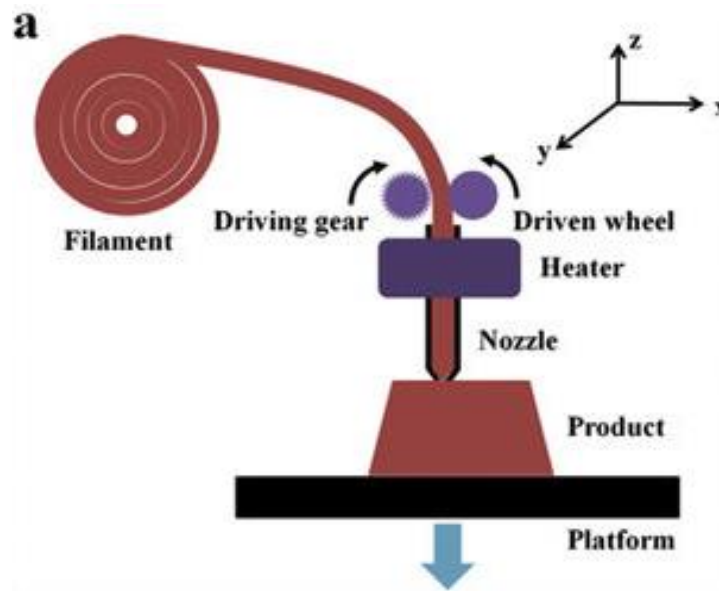


Figure 5.1: Schematic representation of an FDM 3D printer, as adapted from [120].

Another popular 3D printing technology uses a liquid material that polymerizes upon exposure to high intensity light. This method is known as stereolithography (SLA). This method relies on a photo-initiator molecule within the liquid that generates reactive species such as free radicals, cations, or anions that catalyze the polymerization of the monomers in the mixture [117, 118]. This method is more difficult to adapt to suit new materials, since the polymerization reaction must be specifically modified for each specific case. The construction of SLA printers can vary drastically, but always incorporates a build plate that moves along the Z-axis. The object can either be printed on top of the build plate (in a top-down SLA printer) or underneath the plate (in a bottom-up SLA printer, cf. **Fig.**

5.2). The light source for SLA designs can also vary between highly focused lasers, which trace single layer paths like an FDM printer, and high intensity projectors, which broadcast an entire layer at a time onto the liquid. The projection-based printers are often referred to as direct light projection (DLP) printers, and recent models have demonstrated the capability of printing continuously without the need for discrete layer steps. The use of photopolymerization allows these printers to create objects using thermoset polymers that would be incompatible with an FDM device.

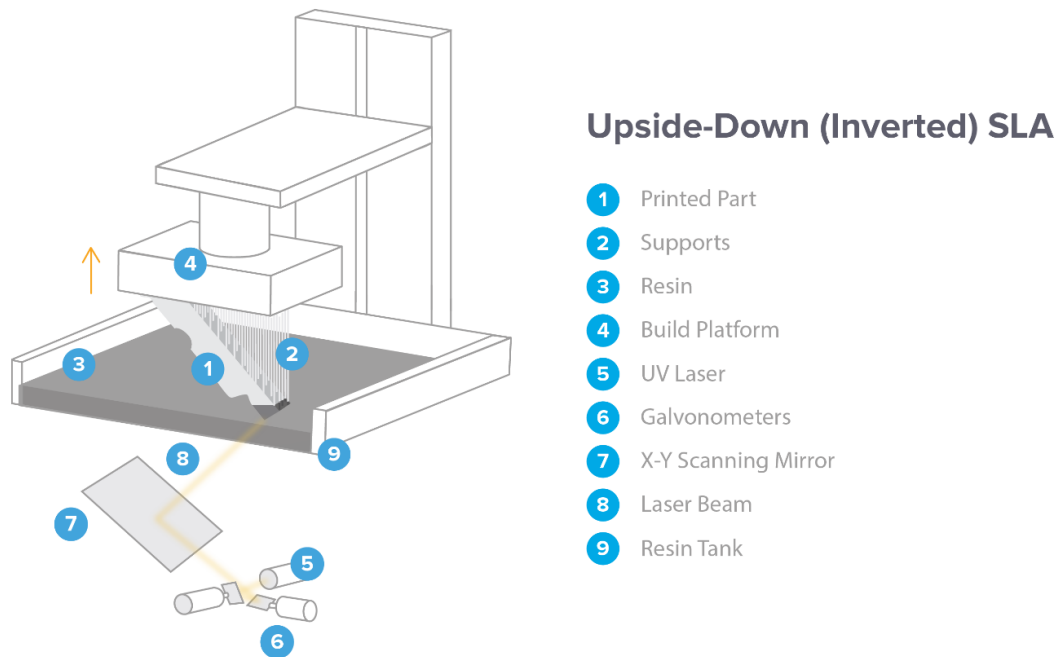


Figure 5.2: Schematic representation of a bottom-up SLA printer. Image courtesy of Formlabs. <https://formlabs.com/blog/ultimate-guide-to-stereolithography-sla-3d-printing/>

Direct ink writing (DIW) technology is less common than either FDM or SLA approaches to additive manufacturing. This method uses a similar extrusion design to that of FDM printers. However, rather than a melted material, a liquid ink is extruded from the

nozzle (**Fig. 5.3**). The liquid ink must have high viscosity and should ideally exhibit shear-thinning behavior to enable high-accuracy printing. There is no single DIW design that is used as a standard configuration. Depending on the material, the ink can be rapidly cured upon extrusion, fixing it in place on the build plate, or if it has enough stability as a liquid, it can be left as a liquid until a post-processing step that cures the entire print at once. One group has demonstrated a DIW printer that uses a laser to cure a copper filament immediately upon exiting the extrusion head [121]. The result is a device that can create three-dimensional geometries in thin air without the need for support materials. This method can be tailored to a wide variety of materials if there is some way to rapidly solidify the liquid phase of the material once it has been deposited. This method has primarily been used to print metallic materials for use in electrical systems and ceramic materials for use in high-strength biomedical applications [122].

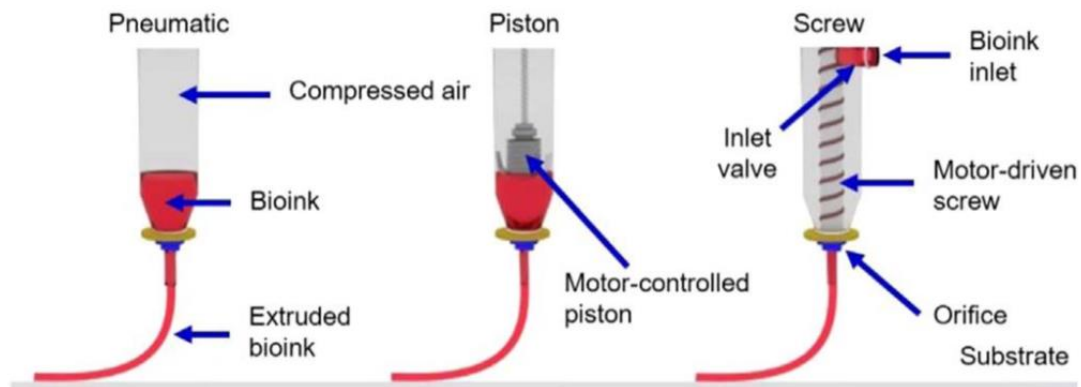


Figure 5.3: Schematic representation of different DIW extrusion methods, as adapted from [123].

This study does not represent the first attempt to adapt additive manufacturing technology for use with SMPs. Since the term shape memory polymer applies to a broad

range of materials with differing mechanical properties, there have been other successful attempts to 3D print using shape memory materials. However, the manufacturing techniques used in these studies are uniquely suited to the type of polymer being used for the print. Zarek *et al.* (2016) successfully printed complex structures (**Fig. 5.4**) made from polycaprolactone (PCL), a thermoplastic polymer, using an SLA method [124]. The liquid resin was created using melted PCL mixed with melted methacrylate, a molecule that polymerizes rapidly in the presence of free radicals. A photo-initiator was added to the resin to provide the free radicals for polymerization upon exposure to UV light. Test prints demonstrated the printer's ability to construct parts with features as small as 600 μm and significant shape memory behavior.

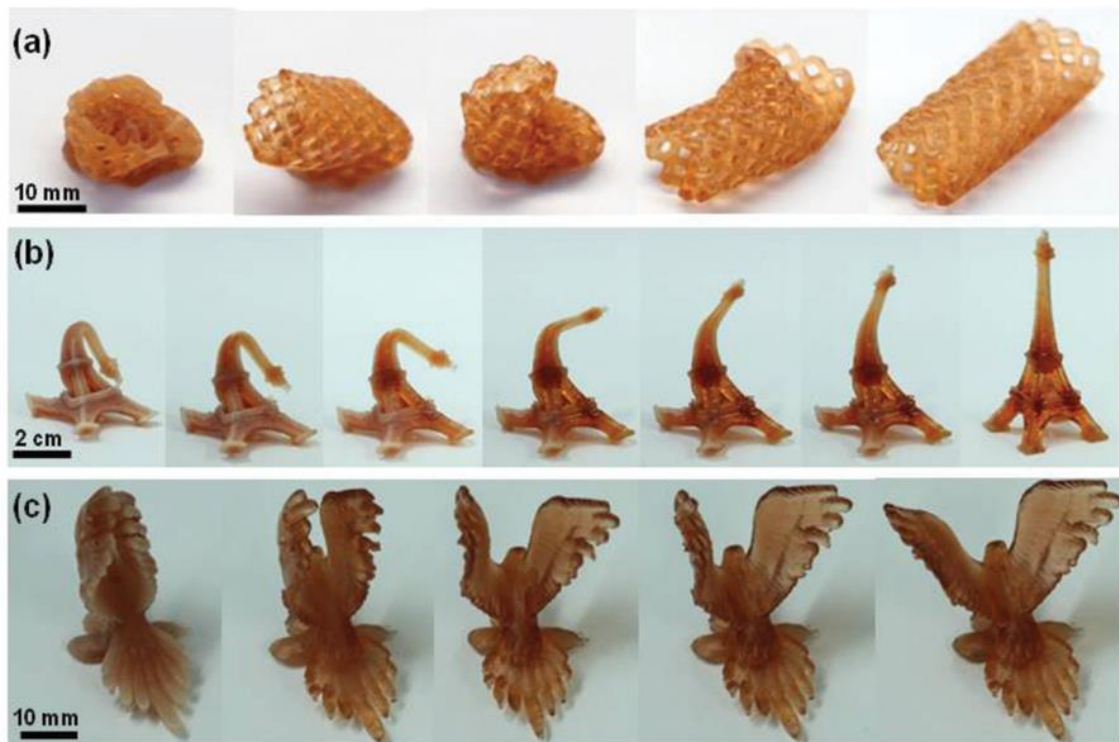


Figure 5.4: Shape recovery demonstrations for fine-resolution SMP objects printed using a viscous oligomer melt and SLA techniques, as adapted from [124].

In another study, Yang *et al.* (2016) successfully created FDM filament using DiAPLEX MM-4520, a commercial thermoplastic SMP [125]. With some slight modifications to a commercial FDM printer to improve part cooling, the group demonstrated FDM printing capabilities with a high dimensional accuracy. Wu *et al.* (2016) utilized the digital material library of a multi-material inkjet printer (Objet260 Connex, Stratasys Inc, Edina, MN, USA) to produce a composite part consisting of a rubbery matrix embedded with two fiber materials with different glass transition temperatures [126]. The shape memory property of this material was achieved by deforming the part at a temperature above the lower T_g and below the higher T_g . This stored energy in the rigid fibers during deformation and secured the deformed shape of the material using the flexible fibers once the part cooled. The nature of the polymers used in the multi-material 3D printer is not entirely clear, since the formula is withheld by the manufacturer. To the best of our knowledge, the only successful SMP 3D printing endeavors have utilized thermoset SMP materials rather than thermoplastics. This means that the thermoset SMP material used by our lab requires a unique additive manufacturing solution.

In this study, we adapted a DIW manufacturing method to accommodate a thermoset aliphatic polyurethane SMP material consisting of an aliphatic isocyanate (HDI), a crosslinking agent (TEA), and a tetraol (HPED). Before selecting a printing method, our group conducted a series of investigations into the relevant material properties for determining viable material manipulation methods. These material properties included the pot life of the polymer, the viscosity of the polymer at different time points during curing, the effect of temperature on the curing rate of the polymer, and the effects of particle

inclusions on the viscosity of the pre-cure polymer mixture. Based on the results of these investigations we were able to eliminate FDM and SLA printing methods and determine a strategy for implementing a DIW printing method using un-cured SMP. After selecting a printer design, we modified a commercial FDM printer to accommodate a large volume liquid extrusion attachment and a more powerful heated bed. The customized printer takes advantage on the heat-dependent curing properties of the aliphatic polyurethane SMP to rapidly cure the polymer on contact with the heated bed. The final printer prototype can create multi-layer prints with a variety of different geometries and shape memory properties consistent with those observed in the solid SMP samples produced in previous studies.

5.2 Materials and Methods

5.2.1 SMP Synthesis and Composition Selection

The SMP used for this study was a thermoset aliphatic polyurethane SMP consisting of an aliphatic isocyanate (HDI), a crosslinking agent (TEA), and a tetraol (HPED). In a previous study, we demonstrated an ability to control the T_g of the resulting SMP by altering the ratios of TEA, HDI, and HPED in the polymer. The composition selected for this study consisted of 60.7% HDI, 10.6% HPED, and 28.7% TEA by weight. This composition was selected because it corresponds to a T_g of 39 °C, making it desirable for use in the human body.

The monomers were vacuum sealed until the synthesis to minimize the risk of moisture absorption. All three components were combined within a nitrogen filled

glovebox in the ratio listed above to further minimize moisture exposure. Once combined, the monomers were mixed for 5-6 minutes using a high-speed shear mixer. A sudden visual shift from cloudy to clear in the mixture was used to confirm successful mixing. Once mixed, the monomers begin to cure, so they were quickly utilized depending on their intended use.

5.2.2 Pre-Cure Hand Extrusion Testing

To test the effects of cure time on the ease of extrusion for the polymer, we prepared square aluminum wafers roughly 5 cm to a side. We marked the sides of the wafers every 0.5cm for scale during extrusion tests. Before starting extrusion testing, we pre-heated a vacuum oven to 40 °C and held the same temperature for the duration of the test. To begin the extrusion testing, we removed the liquid SMP from the glovebox and transferred it into small containers, each of which held no more than 1 gram. To degas the mixture, we placed the containers in a vacuum oven and created a vacuum of -0.8 torr for 1 minute. We purged the oven using nitrogen gas and repeated the degassing process two more times for a total of three degassing cycles. Before the third degassing cycle, we removed a single container from the oven to represent the “0 minute” curing time. After the final vacuuming step, we purged the oven to -0.1 torr where it remained until the containers needed to be removed.

At 30-minute intervals, one container was removed from the oven and emptied into a BD Luer-Lok 3 mL syringe fitted with a 0.9 mm BD blunt fill needle. Vertical lines were deposited on the plate to investigate the spread of the SMP after extrusion, and in later tests, horizontal lines were extruded across the vertical ones to test layer stacking behavior (**Fig. 5.5**). The individual performing the extrusion test qualitatively evaluated the ease of extrusion, and the trials were recorded to investigate material behavior during extrusion at

different time points. At intervals following the first, the extrusion plate from the previous interval was placed in the oven to cure while the next SMP container was retrieved. This procedure was performed starting immediately after synthesis and continued until the material was no longer extrudable as determined by the researcher performing extrusion.

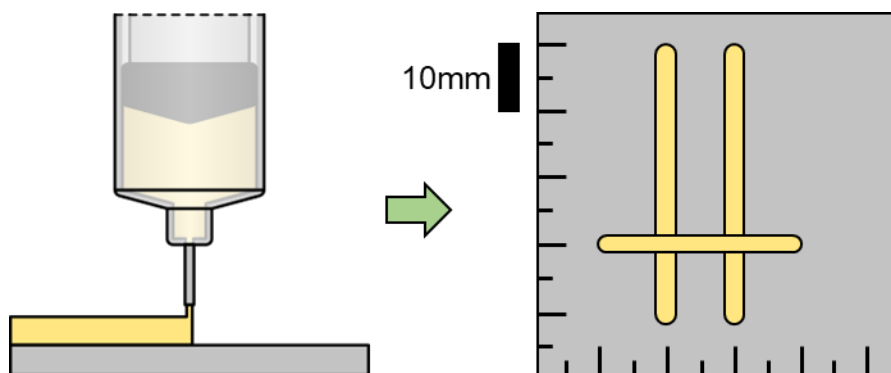


Figure 5.5: Schematic representation of hand extrusion testing protocols. Image courtesy of Ryan Bodlak.

5.2.3 Pre-Cure Hand Extrusion Testing – Salt Inclusion

The procedures described above were repeated with slight modification to accommodate the inclusion of fine salt particles (The Great American Spice Store Co.) with a grain size of roughly 200 μm as measured under a microscope. Salt to SMP ratios of 1:4, 1:2, 3:4, and 1:1 by weight were investigated for each 30-minute interval of pre-cure time. As before, individual containers with 1g of SMP each were stored in the vacuum oven at 40 $^{\circ}\text{C}$ after degassing for three cycles. For these trials, four containers were removed from the oven at each time point, and a pre-measured amount of salt was poured into each container according to the ratios above. Once mixed, each batch was extruded in a vertical line by hand onto an aluminum plate. Like before, the material spread, ease of

extrusion, and material behavior during extrusion were recorded based on observations and recordings from the trials. The trials were repeated until all four Salt-to-SMP ratios in a trial became impossible to extrude.

5.2.4 Rapid Cure Testing

To investigate the effects of temperature on SMP curing time, we prepared 5cm square aluminum plates and marked every 0.5 cm along the side for scale. Heat was provided by a hot plate with automatic temperature control (IKA C-MAG HS 7). The liquid SMP was removed from the glove box and separated into 1g containers to avoid bulk heating effects from the exothermic polymerization reaction. After three cycles of degassing, we pre-cured the mixture for 60 minutes at 40 °C. We removed all SMP containers from the oven after pre-curing and filled BD Luer-Lok 5 mL syringe, fitted with a 1.2 mm BD blunt fill needle, with liquid SMP. We set the hot plate temperature to 100 °C and set an aluminum plate on the surface for long enough to reach equilibrium with the hot plate (~5 min). Once the aluminum plate reached the desired temperature, we extruded 0.05 mL of liquid SMP in a dot on the plate surface in the pattern shown in **Figure 5.6**. We used a steel pin as a probe to determine the point at which the dot became entirely solid. The time required for complete curing was recorded, and the same dot extrusion procedure was repeated four more times for a total of five trials at each temperature point. This extrusion procedure was performed from 100 °C to 200 °C with intervals of 10 °C between any two sets of data.

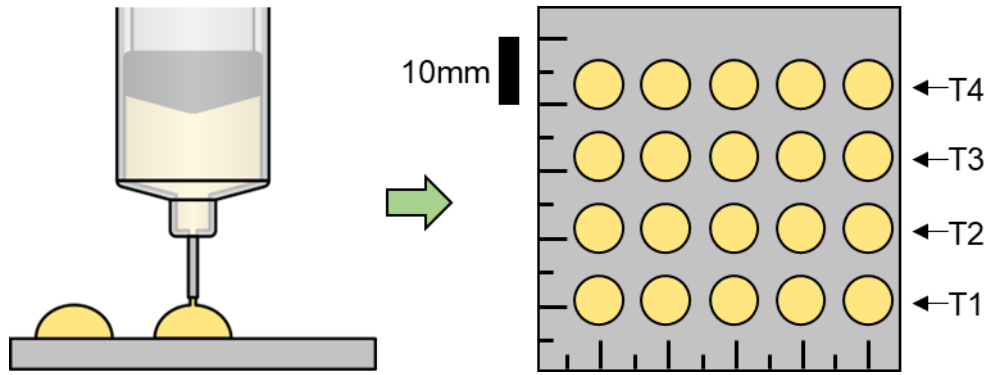


Figure 5.6: Schematic representation of rapid cure testing protocols. Image courtesy of Ryan Bodlak.

5.2.5 Printer Design and Construction

The DIW printer prototype was based on a modified Creality CR-10s FDM printer. The filament extruder was removed and replaced with a syringe-based large volume extrusion attachment. This extrusion device was created using 3D printed components, a BD Luer-Lok 60 mL syringe, and a stepper motor, based on the design published by Pusch *et al.* (2018) [127]. To achieve the temperatures necessary for rapid SMP curing, the stock bed heating element had to be removed from the CR-10s and replaced with a more powerful substitute. The replacement heating element was a KEENOVO 120V silicone heating bed, which required a conversion from DC power to AC power. The wiring modifications added to the printer were performed according to the schematic in **Figure 5.7**. In this case, the input signal came from the control board of the CR-10s, the load was the silicone heating bed, and the power source was a cable attached to the wall outlet. **Figure 5.8** shows the final CAD model of the prototype printer alongside the completed system.

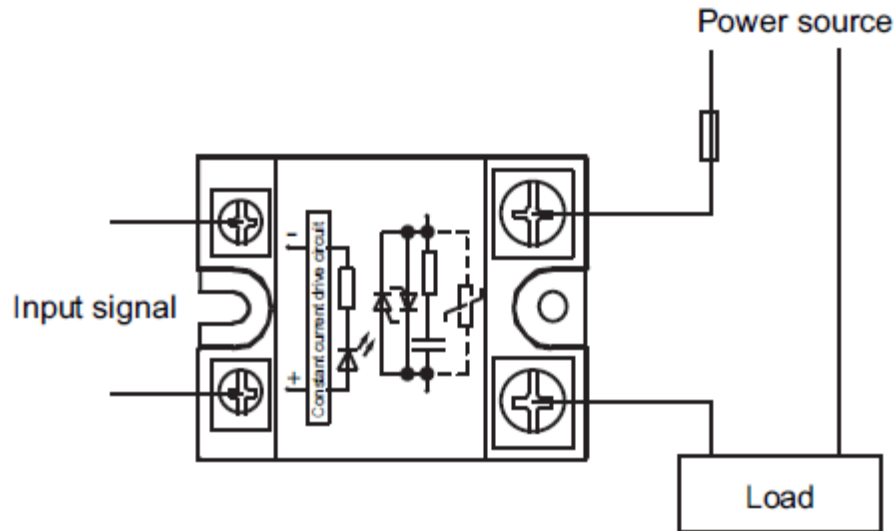


Figure 5.7: Wiring diagram for a solid-state relay. In this scenario, the wall outlet is the power source, the input signal is received from the Creality temperature control board, and the load is the KEENOVO silicone heated bed. Image courtesy of:

<https://electronics.stackexchange.com/questions/323877/two-way-wiring-using-ssr>.

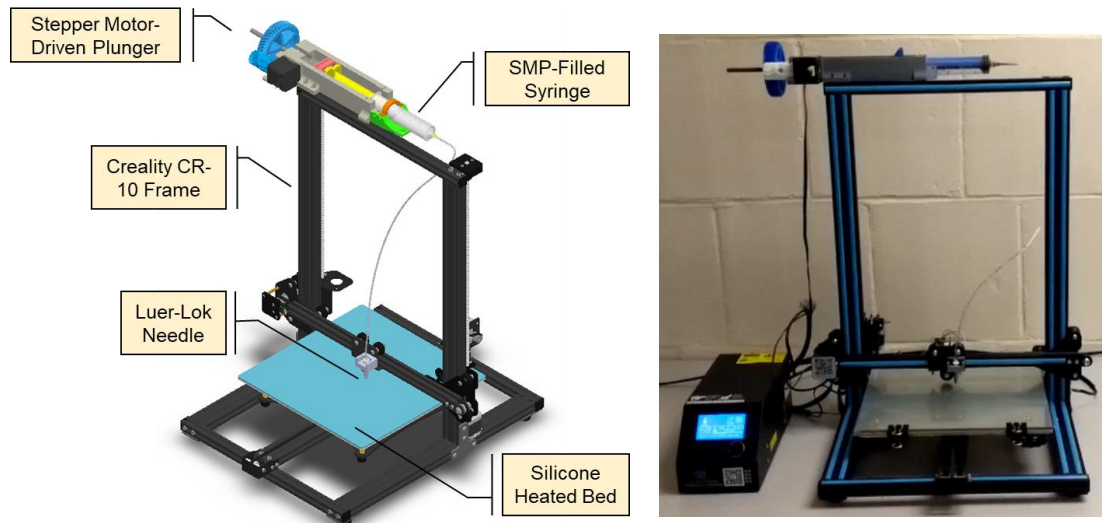


Figure 5.8: CAD rendering of the prototype DIW printer (*left*), and photo of completed prototype DIW printer (*right*).

5.2.6 SMP Printing Procedures

Once the prototype printer was constructed, our group selected a few basic geometries to use as test prints while we investigated the printing parameters required for effective DIW printing. The shapes selected for test printing included single-pass straight lines, thin-walled cylinders, thin-walled squares, and a replica of the University of Oklahoma logo. All geometries were designed in SolidWorks CAD software and sliced using Cura, the default software for interfacing with the Creality CR-10s printer. Before each print, a batch of SMP was synthesized according to the procedures listed above. No more than 15 g of SMP was synthesized at one time to avoid rapid curing within the large volume extruder due to exothermic heating effects. The syringe in the large volume extruder was detachable, allowing us to load the liquid SMP material from within the nitrogen glove box, limiting the polymer's exposure to moisture. The syringe was then affixed to the large volume extruder, and any air was purged from the extrusion tubing. Any excess pressure from purging was allowed bleed out of the line, and a small container was placed underneath the extrusion needle to collect any droplets of SMP. Once the dripping finished, the print was started normally using the control console on the CR-10s.

5.2.7 Extrusion Volume Calibration

We discovered quickly that the volume of SMP extruded by the large volume extruder was not corresponding to the correct volume required to create our parts. The disagreement between the volume required for the print and the volume supplied by the extruder was traced back to a parameter called "Flow" in the Ultimaker Cura software that controlled the feed rate of the stepper motor on the large volume extruder. To properly calibrate the prototype printer, we needed to find a new value for this parameter. We

performed a calibration test by creating a CAD model with a volume of exactly 1mL and slicing the model in Ultimaker Cura. We theorized that we could print this model using the prototype printer and compare the “actual” extruded volume with the “expected” extrusion volume (1 mL), then adjust the “Flow” parameter accordingly.

The specific variable controlled by the “Flow” parameter was set to a value of 93 with unknown units. The “Flow” parameter in Ultimaker Cura took the form of a percentage set by default to 100%. Any changes to this percentage would increment the variable by the user-specified percent. We used the default values of these parameters as the starting point of our calibration tests. When the print finished, we used the graduations on the side of the extruder syringe to measure the actual extrusion volume. If the value was different than the expected volume, we modified the “Flow” parameter accordingly and performed the test again. This process, illustrated in **Figure 5.9**, was repeated until the actual extrusion volume matched the expected volume.

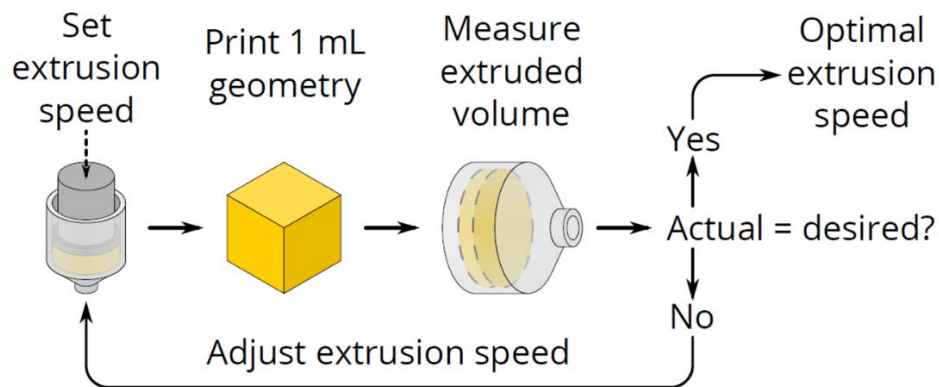


Figure 5.9: Flow chart representation of extrusion speed calibration process. Image courtesy of Ryan Bodlak.

Test prints were performed while the large volume extruder was filled with air, water, and glycerin to rule out any differences caused by material type. Test prints were also performed for differing amounts of each material to rule out any effects that may affect printing for large versus small material reservoirs. Finally, test prints were performed with different values entered in the “layer height” (Z-axis step size) and “print speed” (X-Y translation speed) fields to ensure that there was no interdependence between these parameters and “Flow” programmed into the Ultimaker Cura software.

5.3 Results and Discussion

5.3.1 Pre-Cure Hand Extrusion Testing

It was clear shortly after beginning the hand extrusion trials that any quantitative results would be unreliable due to the high degree of variability in manual extrusion techniques. However, the results of these tests still provided useful qualitative information that helped to inform our design of the prototype DIW printer. Sample results from each time point are shown in **Figure 5.10**. At $t = 0$ minutes, the polymer was extremely runny, with a consistency similar to that of water. The extruded line did not hold its shape and spread to a width of 2 cm immediately after extrusion. The liquid tended to form droplets at the end of the needle before flowing onto the plate, making it difficult to create a uniform linear extrusion.

At $t = 30$ minutes, the polymer was noticeably more viscous, this time resembling glycerin during extrusion. The liquid was easier to deposit in a straight line and did not

form as many droplets at the end of the syringe. The resulting line of polymer spread to a width slightly greater than 0.75 cm immediately after extrusion.

At $t = 60$ minutes, the polymer still behaved like a liquid, but increased in viscosity once again. The material at this point behaved like a syrup and formed a very uniform line upon extrusion. The line had a width of 0.5 cm immediately following extrusion and spread to a width of 0.75 cm after 10 minutes.

At $t = 90$ minutes, the polymer began to exhibit gel-like properties and held a slightly cylindrical shape after exiting the syringe. At this point, the polymer was still easy to extrude, but there was a noticeable resistance to extrusion that had not been present in a significant way before. Lines created with this polymer started at a width of 0.25 cm and expanded to a width of 0.5 cm after 30 minutes.

At $t = 120$ minutes, the polymer became even more gel-like and extrusion became difficult. The polymer held a clearly cylindrical shape upon exiting the syringe, and threads of polymer stuck with the needle when it was pulled away from the plate. The lines from this round of extrusion were slightly less than 0.25 mm wide and expanded to 0.25 mm after 30 minutes.

At $t = 150$ minutes, the polymer behaved almost like taffy and took a great deal of effort to extrude from the syringe. Mostly due to a lack of control on the human end of this trial, these lines were wider than the previous time point, measuring almost exactly 0.25 cm wide. They did not experience significant slumping after 30 minutes. The syringe was damaged in the process of extruding material at the 150-minute marker, prompting us to declare the material un-extrudable by hand past this time point.

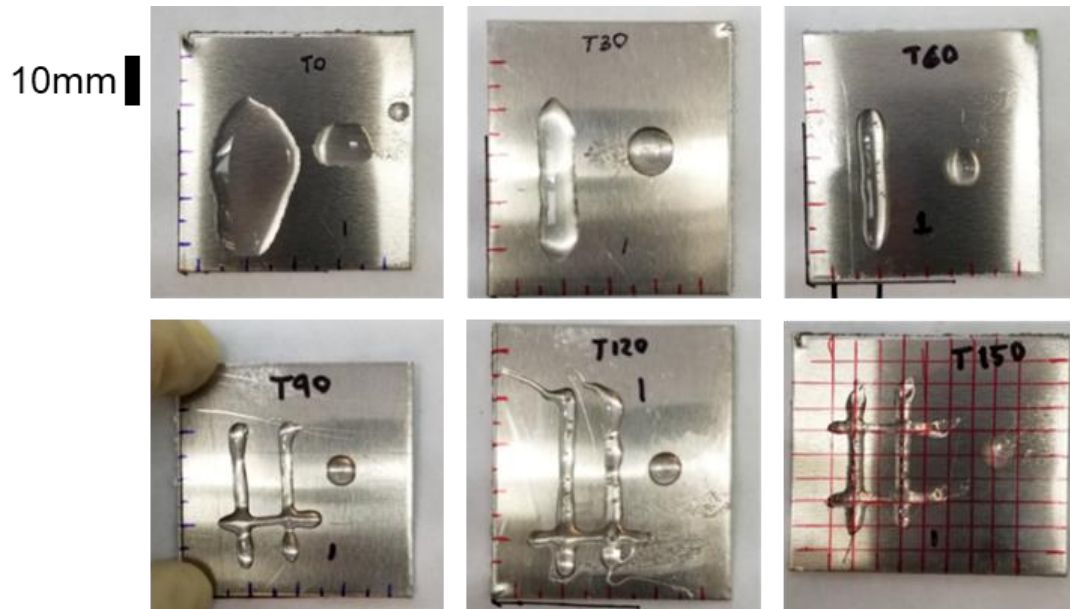


Figure 5.10: Hand extrusion testing results.

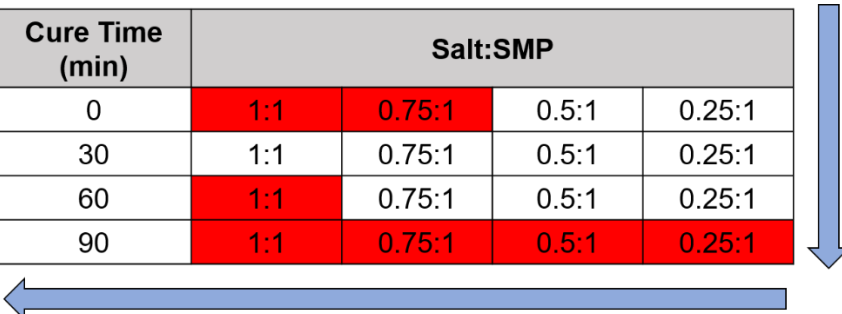
5.3.2 Pre-Cure Hand Extrusion Testing – Salt Inclusion

The primary objective of the hand extrusion tests was identifying an ideal Salt:SMP ratio and a corresponding pre-cure time that would minimize spreading while also allowing for easy extrusion. A few trends emerged from this study. Within the same time step, a greater amount of salt in the mixture resulted in a more viscous mixture and required a higher pressure for extrusion. With the salt:SMP ratio held constant, a greater pre-cure time resulted in a more viscous mixture and required a higher pressure for extrusion for every time step except $t = 0$ minutes. At $t = 0$ minutes, extrusion was inhibited by the settling of salt in the nozzle of the syringe. Since the liquid SMP had such a low viscosity at this time point, the salt would not stay suspended in the mixture, causing frequent clogs in the syringe as it piled up to block the nozzle.

At $t = 30$ minutes and beyond, the mixture was viscous enough to suspend salt particles during extrusion, and clogs were much less frequent. The observational results of the salt extrusion tests are described in **Table 5.1**. An unusual effect that resulted from the addition of salt particles was a pronounced foaming behavior. When salt particles were added to the pre-cured SMP, the resulting mixture took on a “fluffy” texture that was compared to marshmallow or meringue during the investigation. The foaming could be observed in the extruded material as well, giving the resulting lines a “puffed-up” appearance (**Fig. 5.11**). One theory is that the sub-millimeter salt particles facilitate a significant introduction of gas into the mixture during hand mixing. The material did not appear to expand at all after mixing or during extrusion, suggesting that the gas in the mixture was introduced physically instead of being produced by some chemical reaction in the material.

Table 5.1: Hand extrusion testing - salt inclusion results. Red cells indicate an inability to extrude material.

Cure Time (min)	Salt:SMP			
0	1:1	0.75:1	0.5:1	0.25:1
30	1:1	0.75:1	0.5:1	0.25:1
60	1:1	0.75:1	0.5:1	0.25:1
90	1:1	0.75:1	0.5:1	0.25:1



Increasing Extrusion Pressure, Thicker Paste

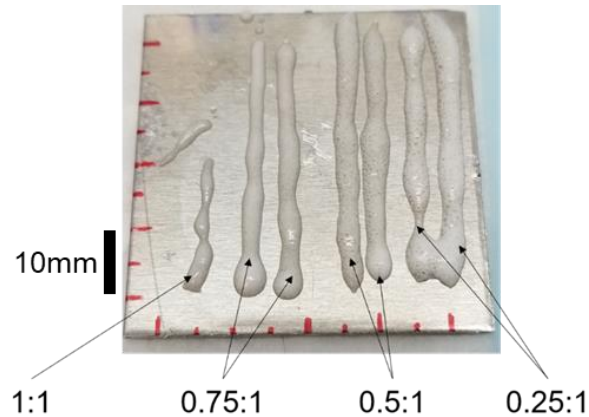


Figure 5.11: Hand extrusion - salt inclusion results. Samples shown were extruded at $t = 60$ minutes.

5.3.3 Rapid Cure Testing

The rapid curing tests showed a strong relationship between the temperature of the extrusion surface and the cure time of the liquid SMP. A 0.05 mL droplet of liquid SMP cured within 200 seconds on average when placed on an aluminum plate heated to 100 °C. With increasing temperature, the cure time decreased exponentially, leveling off at a cure time of slightly less than 30 seconds. When the plate temperature was increased to 200 °C, that cure time was decreased to 22.6 seconds on average. As shown in (Figs. 5.12a-b), temperature increases begin to have diminished returns around 150 °C, where the cure time reaches a value of 31.2 °C. At temperatures above 180 °C, the SMP became discolored, taking on a yellow to burnt orange hue. The discolored SMP also became very brittle, and many samples cracked or chipped as they were removed from the aluminum plates. It became clear that any printing applications should avoid heating samples above 180 °C to prevent thermal degradation in the part. We selected 150 °C as a target temperature for any

rapid curing applications since it provides a curing time of 31.2 seconds, only a few seconds longer than the minimum achievable cure time and keeps the material well below the onset of thermal degradation. Based on the success of the rapid curing tests, we elected to proceed with a DIW printer design that utilizes a heated bed at 150 °C to solidify the liquid SMP as it is deposited.

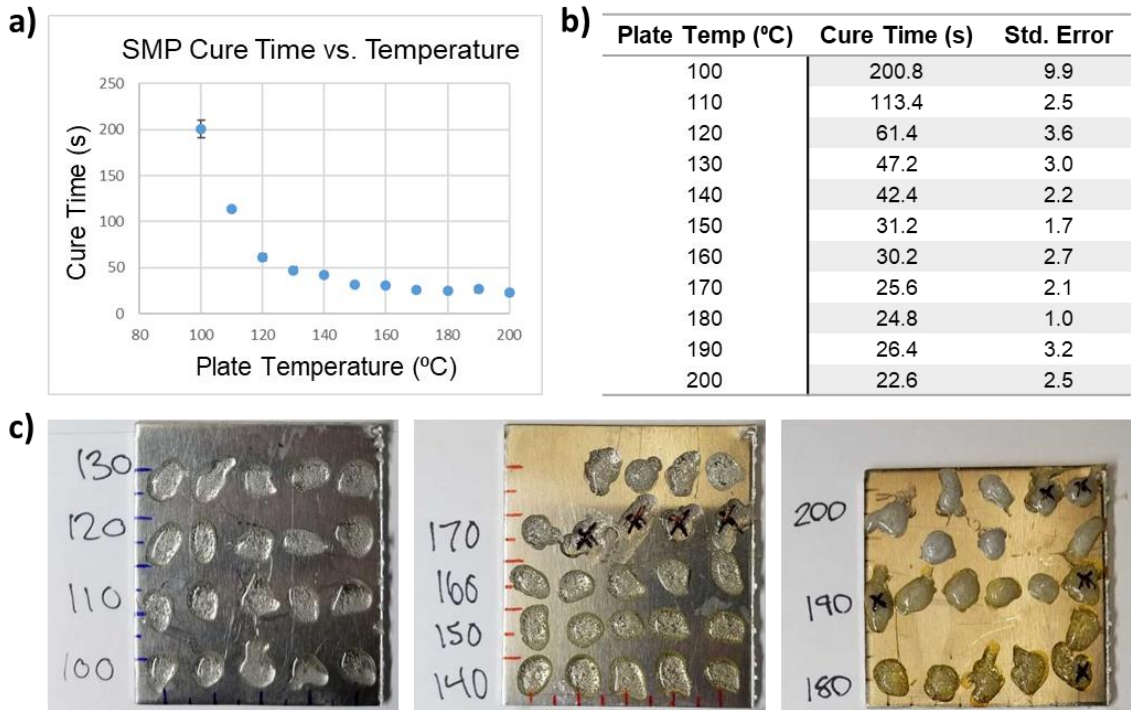


Figure 5.12: a) Plot of cure time as a function of plate temperature, showing a sharp decrease in cure time which levels out near 150 °C. b) Numerical values for cure time as a function of plate temperature. c) SMP samples synthesized during rapid cure testing. Note that the SMP at 180 °C and 190 °C show yellowing due to prolonged exposure to high heat. Distance between long marks = 10 mm.

5.3.4 Extrusion Volume Calibration

The calibration tests for the “Flow” parameter showed that the parameter was independent of all variables tested. The glycerin, water, and air tests all resulted in the same value regardless of how full the syringe was. The parameter also did not change for different values in the “print speed” and “layer height” categories. The parameter value that resulted in an agreement between actual and expected extrusion volume was 39.4%. Since this parameter does not vary with differences in material, other parameter values, or amount of material, we can hold this value constant for all our future prints unless another modification is made to the large volume extruder.

5.3.5 Printing Parameter Refinement

After the printer had been assembled and calibrated properly, a variety of guidelines were produced based on test prints. The first of these relates to the print speed (X - Y translation speed) setting in the Ultimaker Cura software. When printing small geometries, we discovered that each layer would finish printing before the first had cured. The result of this issue was excessive material slump and loss of part height, which caused further problems once the needle was far enough from the print to allow for droplet formation. To avoid this, we determined that the print speed must be kept below 10 mm/s for prints that are small enough to fit within a 10 mm circle. For prints larger than this, the print speed can increase to any value below 20 mm/s and still achieve accurate results. We also investigated the effects of layer height on print quality. The best results were achieved with a layer height between 0.100 and 0.05 mm. In general, the smaller the layer height we were able to use, the better the resulting print looked. This obviously came with the downside of an increased print time, but for small prints this was not much of an issue.

Figure 5.13 shows a comparison between an early test print before calibration and parameter tuning and a later multi-layer print that was produced after the printing parameters had been adjusted.

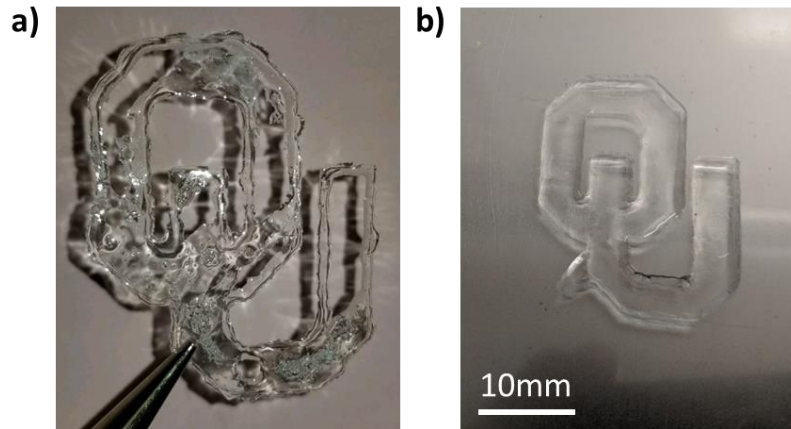


Figure 5.13: Comparison between an early SMP test print and a refined SMP test print. a) First successful test print using DIW printer, showing signs of un-calibrated extrusion speed and slow SMP curing. b) Later multi-layer SMP print with refined extrusion speed and proper cure temperature.

One of this system's major weaknesses that we observed is the limited working time for the SMP material within the syringe. As our parameter studies discovered, the best ways to improve the quality of parts produced by this system also extend the duration of the print. We have already shown that the liquid SMP material becomes un-workable within 150 minutes when kept in a 40 °C environment, but the behavior of the material begins to change well before that time. Testing procedures were only able to last for 1-1.5 hours before extrusion was halted by the viscosity of the SMP. This means that some balance needs to be struck between print quality and total printing time. It also means that the printer may be limited to the production of small objects until a method of extending the working time of the material is discovered.

Another limitation of the printer that was observed during testing is the decrease in temperature as the height of the print increases and the curing plane moves farther from the heated plate. The reduced heat flow creates a scenario where each layer of the print takes longer to cure than the previous one, much like the case described above in which the printer moved too quickly and began extruding the second and third layers of the print before the first layer could cure. The result in both cases is an increase in material slump and incremental height loss, which can both be observed in **Figure 5.14**. Once test prints began reaching heights of 5mm, the top layers were observed to be sticky to the touch at the end of the print. This suggests that the material may not be fully curing at all for the upper layers of tall prints.

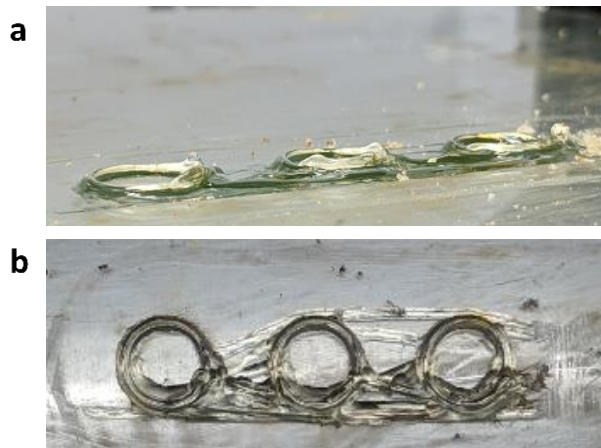


Figure 5.14: Messy print showcasing many persistent shortcomings of the printer. a) Inconsistency at the upper layers of the print and material slump are clear from a side view. b) Poor extrusion control (due to residual pressure after the extrusion ends) can be seen between these individual rings.

5.4 Concluding Remarks

5.4.1 Summary of Findings

In this study, we successfully identified a printing method compatible with a thermoset aliphatic polyurethane SMP. After performing extrusion tests with both pure SMP and SMP containing salt crystals as a stabilizing additive as well as rapid curing investigations with pure SMP, we selected a DIW approach. We modified a Creality CR-10s FDM printer to accommodate a large volume syringe extruder and a much more powerful bed heating element. The final system demonstrated that the liquid SMP could be extruded through a small, blunt-tipped needle onto a plate held at a high temperature to produce solid objects with shape memory properties. Our rapid curing tests identified an ideal curing temperature of 150 °C for use during the printing process. The extrusion tests predicted a maximum working time of 90 minutes before the material began to exhibit gel-like properties, inhibiting extrusion. We identified the current limitations of our printing technology, which govern the accuracy of our printed geometries and the maximum length of a given print. High accuracy could be achieved with small print geometries as long as the layer height was kept between 0.100 and 0.05 mm, and the print speed was kept below 5-10 mm/s. Accuracy comes as a tradeoff with print length, meaning that accurate prints must be kept small, or else SMP curing will become an issue during the print. Print height also cannot progress far above 5 mm at the current date without causing issues with material curing.

5.4.2 Future Extensions

While this study shows that a DIW printer which creates objects by thermally curing thermoset polymers is possible, there are still many improvements to print quality that need to be implemented. One area that can be improved drastically in future iterations of this design is the heat source used during printing. At the moment, all heat is supplied by a heated plate at the bottom of the print. Alternative heating methods that could more directly affect material as it is extruded include optical heating using a laser, focused radiative heating using a heating element mounted near the extruder, and a sealed, uniformly heated build environment coupled with a cooled extruder to avoid curing in the system's nozzle. Future efforts to improve the system will include detailed investigations into the most efficient heat delivery mechanisms to allow for taller prints without the fear of material slump. Another topic that should be investigated in future studies is a method for delaying the natural curing process of the liquid SMP until it is exposed to the heated printing environment. Complicating this task is the fact that the addition of heat simply speeds up the natural curing process of the material, so any curing inhibitors may also inhibit material curing after extrusion. Since the curing method used in the design of this printing system doesn't chemically modify the polymer in any way, we don't expect any differences in the shape memory properties or strength of the material. However, future studies could investigate the thermo-mechanical properties of printed material in comparison with pristine SMP material cast as beams to confirm these suspicions.

CHAPTER 6: Conclusions and Future Studies

6.1 Summary of Findings

This series of experimental investigations characterized an aliphatic polyurethane shape memory polymer with a focus on its use in the development of a novel treatment for intracranial aneurysms. The polymer was synthesized in solid beam and dog-bone specimens using twelve different ratios of its monomer components, Hexamethylene Diisocyanate (HDI), Triethanolamine (TEA), and N,N,N',N'-Tetrakis-2(Hydroxypropyl)ethylenediamine (HPED). Thermomechanical characterization was carried out using both DSC and DMA. The results of both DMA and DSC were used to identify the range of glass transition temperatures (T_g) based on variations in the monomer composition of the polymer. Both methods, in agreement with one another, indicated a range of T_g values between 87 °C and 33 °C. The mechanical properties of each composition were investigated using both uniaxial failure and uniaxial cyclic testing. From the results of these tests, the failure stress, failure strain, elastic modulus, and stress relaxation behavior, were reported for each composition. Preliminary testing of the shape memory properties of the material was used to identify a relationship between material recovery rate and temperature above T_g . Based on the findings of this study, a polymer composition with a T_g in a desirable range for use in the human body was selected for more detailed investigation as the primary component in a novel aneurysm treatment device.

The selected polymer composition was then manufactured as a foam using a sugar particle leaching technique. The sugar leaching technique was shown to produce an open-cell geometry with a regular pore size and pore distribution using both μ -CT and SEM

imaging methods. The foam demonstrated good shape recovery properties, returning to its home configuration in under a minute after it was raised above its T_g . After being tested using a uniaxial compressive loading protocol, the foam was shown to have elastic modulus values both above and below T_g that are comparable to other SMP foams being investigated for medical uses. Failure was observed at 90% compressive strain, indicating that more efforts are likely necessary to reduce the foam density before it can compress to small enough sizes for medical use. Compression ratio aside, the results of this investigation make a strong argument for the potential of this foam in the design of an SMP foam embolization device.

In the interest of exploring new manufacturing options for the SMP, we developed a direct ink writing (DIW) 3D printer that is compatible with thermoset polymers. The printer takes advantage of the thermally dependent curing properties of the SMP to rapidly cure a liquid monomer mixture as it is extruded onto a heated print bed. During the development of the printer, experiments were conducted to investigate how the properties of the liquid SMP change as the polymer cures. The maximum working time for the SMP was found to be roughly 150 minutes based on observations from hand extrusion testing. The addition of salt shortens the working time for the SMP but helps to stabilize the extruded liquid at lower pre-cure times and prevent material spreading. The effects of temperature on curing were investigated, and an optimal cure temperature of 150 °C was identified. A prototype of the DIW SMP printer was constructed from a Creality CR-10S fused deposition modeling (FDM) printer modified to accommodate a large volume syringe extruder and a more powerful silicone heating bed. Objects printed from the prototype have high accuracy in the x and y dimensions but suffer from material slump and incomplete

material curing as the print becomes taller. In light of the prototype printer's shortcomings, we identified several key improvements that should be made in future design iterations including a more uniform heating method independent of part height and a method for inhibiting passive material curing inside the reservoir of the large volume extruder.

6.2 Future Investigations

6.2.1 Investigate the biocompatibility of solid SMP and SMP foam materials

Although the biocompatibility of this material has been investigated by Rodriguez *et al.* (2014) with promising results, the materials produced using this study's synthesis procedures have not been tested [35]. Even if a material is found to be biocompatible on its own, different manufacturing processes can introduce sources of cytotoxicity. Since multiple manufacturing methods are being investigated as a part of this ongoing research, it is important that a reliable series of biocompatibility tests is developed to verify that any new manufacturing techniques have not changed the way the material interacts with the body. The use of a mammalian cell culture with an extract solution from the material in question is a promising first stage for biocompatibility testing [128]. The effects of the material extract can be quantified using an MTT assay, which produces violet pigment in the presence of living cells [129]. Cell death can be determined by analyzing absorbance measurements once the MTT has been added to the culture.

6.2.2 *Identify a suitable SMP triggering mechanism and evaluate its efficacy*

The polymer investigated in this research is a thermally activated SMP with a T_g that can be temporarily lowered with the absorption of water [130]. Since this material will eventually be used in an implantable medical device, a triggering mechanism must be identified that can be used to remotely activate the material's shape recovery behavior. Candidate triggering mechanisms include a central electric heating element, wavelength-specific light absorption, passive deployment (T_g lowered past 37 °C), and magnetic induction [47, 48, 131, 132]. Important factors to observe during testing will be the speed at which the polymer recovers its shape, the ability to control the temperature of the SMP device, and the ease of implementation (magnetic heating would require exterior equipment).

6.2.3 *Design a micro-catheter delivery system that incorporates a shape recovery triggering mechanism for SMP deployment*

If this material is going to be delivered to a cerebral artery via endovascular means, a delivery system will need to be designed that is compatible with a micro-catheter platform. Based on recommendations from our clinical collaborators, the device would need to be compatible with a catheter no larger than 4.4F (or 1.47mm I.D.). The design of this catheter system would depend on the results of the shape recovery triggering investigations described above, since different deployment methods would obviously require different devices. In addition to designing a deployment device affixed to a microcatheter, these studies should include investigations into reliable compression methods to use when preparing the SMP device for delivery. Consistently deforming the SMP into a form with a

comparable diameter to the microcatheter and securely attaching it to the catheter tip are crucial steps in the design of this aneurysm treatment device. Previous studies have successfully used heated crimping devices to compress the SMP around a solid core fixed to the catheter, but the associated equipment would need to be customized to be compatible with the design of the rest of the delivery device [47, 131].

6.2.4 *Develop an in-vitro testing environment to evaluate device performance in a simulated aneurysm*

A test environment capable of simulating the fluid behavior within an intracranial aneurysm is necessary if the effectiveness of a treatment device is going to be evaluated. With the variety of manufacturing techniques introduced in this research, a potential SMP aneurysm treatment device could take many different forms. An *in vitro* test environment would allow for a direct comparison of the effectiveness of different device designs based on the effect they have on fluid flow within the aneurysm body. With this application in mind, development of a test environment began in parallel with the research presented in this study. This effort was the focus of a senior design capstone in Spring 2018. At the conclusion of the project, the design featured a flow loop fed by an elevated reservoir, fed by a peristaltic pump [pump brand] in parallel with a non-programmable submerged pump [pump brand]. The head provided by the reservoir drove fluid flow through a simplified aneurysm phantom cast from Sylgard 184, where fluid behavior was observed using a particle image velocimetry (PIV) system (TSI Incorporated). **Figure 6.1** shows the completed flow loop from the Spring 2018 Capstone

project. Later investigations showed that the flow loop did not provide enough control over flow behavior to successfully mimic the flow properties of the internal carotid artery.

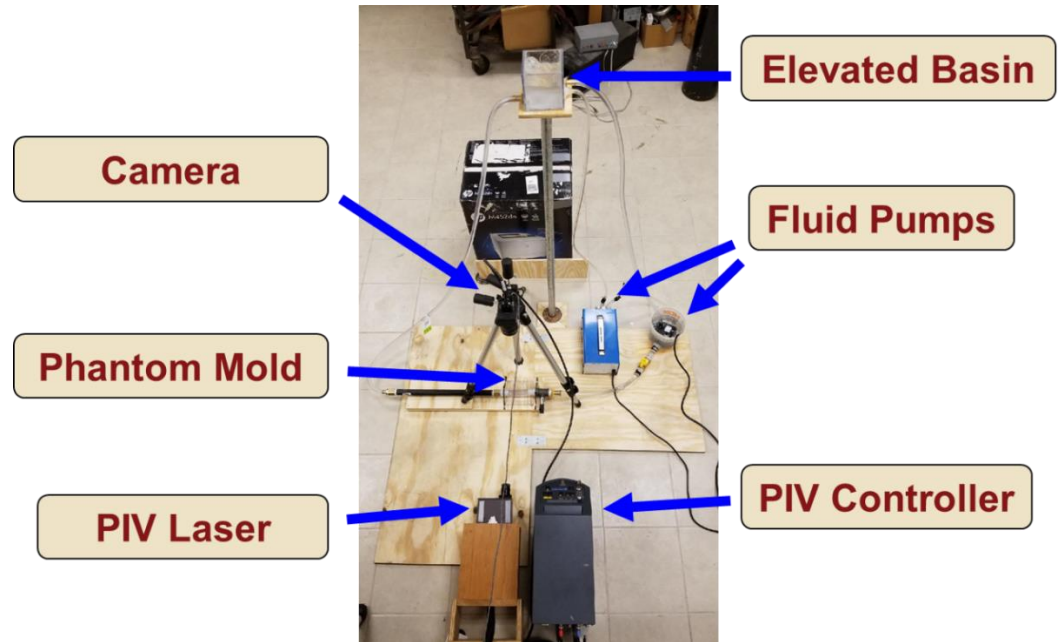


Figure 6.1: First iteration of the PIV flow loop design, created from the Spring 2018 Capstone project.

The flow loop has been re-designed through more recent efforts to allow for more accurate simulation of physiological blood flow conditions. The current design of the test environment (**Fig. 6.2**) is a flow loop driven by a peristaltic pump with an adjustable volume flow rate and a resistance controlled using a ball valve placed immediately before the fluid recirculates into the system's reservoir. Volumetric flow rate is measured using a clamp-on ultrasonic flow meter, and pressure measurements are recorded at both the inlet and outlet of the aneurysm phantom using catheter-based pressure transducers. Ongoing development of this system

will focus on ordering the sensor components of the system, assembling the flow loop, and performing validation tests to ensure the accuracy of all sensing components.

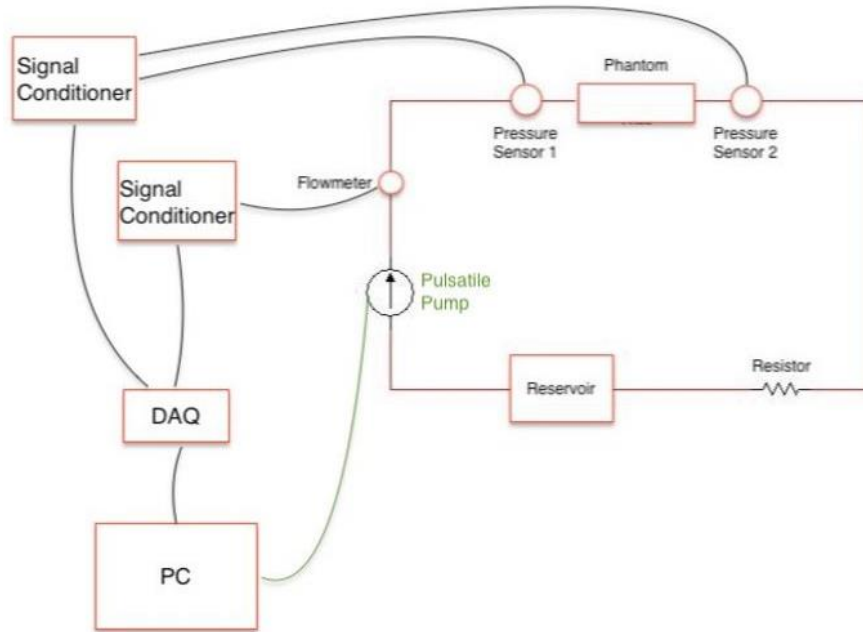


Figure 6.2: Schematic for the revised flow loop design, currently in development.

Future iterations of this design should eventually incorporate pulsatile flow to mimic physiological waveforms taken from measurements in the internal carotid artery. Many pumps designed to produce physiological waveforms are cost-prohibitive, meaning that research into designing and constructing a computer-controlled pumping device with enough accuracy to mimic blood flow waveforms may be necessary. Another development that would add value to the system is the development of aneurysms with finite wall thickness. At the moment, the aneurysms used with the system are cast in a block of Sylgard, resulting in a fixed-wall assumption for our measurements. Artery tissue in the human body deforms

with the pulsing of the blood pressure. Research into the creation of thin-walled phantoms that can mimic the expansion and contraction of cranial arteries would eliminate the error associated with a fixed-wall assumption.

6.2.5 *Develop and validate a computational simulation framework for blood flow within an aneurysm to aid in device design*

While experimental means are useful for determining the effectiveness of a device when its form has already been determined, optimization of the device's form can be difficult if each iteration of the design requires the production and testing of a new prototype. If a computational model could be used instead to simulate the change in blood flow within the aneurysm as a result of device deployment, the need for experimental iteration could be eliminated. To produce a computational model, a method of experimental validation is necessary, which could take the form of the *in vitro* flow loop in this case. Patient aneurysm geometries could be acquired from medical CT imaging data and converted to STL format using an image segmentation software. These geometries could also be replicated as Sylgard phantoms and incorporated into the flow system, where the flow within them could be investigated experimentally using PIV or a similar technique. A computational model of fluid flow in the aneurysm could be developed and then subsequently validated using the experimental flow data. Even more sophisticated simulations could use a fluid-structure interaction framework to simulate an entire treatment procedure. The mechanical characterization performed in this study could be used to inform the behavior of the SMP material, and in the case of a foam material, the μ -CT imaging performed on foam samples in Chapter 4 could provide

the geometry. This type of simulation could also incorporate the motion of the vessel wall if the flow loop could be equipped with finite-walled phantoms for validation. If a computational model that can simulate device deployment can be established and validated, the optimal form/shape for the SMP device will be much simpler to investigate.

Appendix 1: SMP Foam Synthesis Procedures

A1.1 System Setup

The nitrogen tank should be connected to both the inlet of the glove box (top hose connection) and the inlet of the vacuum oven (hose barb, should be be labeled) according to the blue connections in **Fig. A1.1**. Make sure the ball valves on the tubing are all set to the “open” position. An outlet hose, shown in red in **Fig. A1.1**, should be attached to the bottom hose connection on the glove box, and its end should be fixed in place at a high point in the fume hood (this way no one breathes any harmful vapors and we don't fill the room with nitrogen). The vacuum connection on the oven should be attached to the yellow vacuum pump, which should be stored in the fume hood during operation.

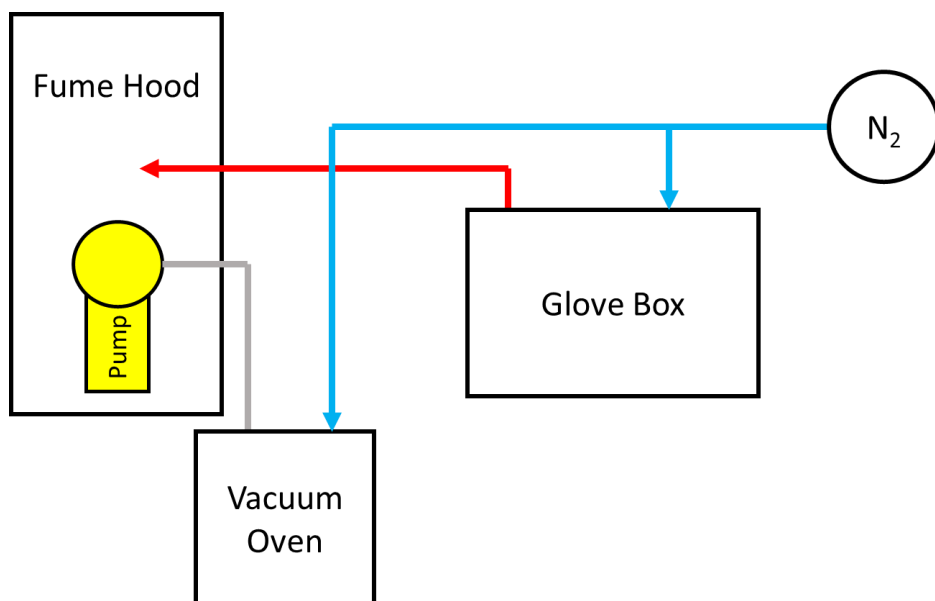


Figure A1.1: Workspace layout for SMP synthesis procedures.

A1.2 SMP Synthesis

Before beginning a synthesis reaction, it is important to make sure all the necessary materials are placed in the glove box since it will be problematic to add items once nitrogen is flowing. The items needed are as follows:

- Digital scale
- Magnetic stir plate with stir bar and stir bar retrieval tool
- Glass beaker for mixing monomers
- Disposable plastic containers for measuring out monomers
- HPED, TEA, and HDI containers
- Motorized pipette controller and disposable glass pipettes (at least 2 for each synthesis batch)
- Kim wipes
- Waste container

Also, make sure appropriate personal protective equipment is worn:

- Disposable gloves
- Surgical mask
- Eye goggles

1. Ensure that the lid of the glove box is clamped down and sealed on the sides.
2. Turn on the nitrogen flow to the glove box.
3. Measure the calculated mass of HPED into the glass beaker using the digital scale.

- HPED is the most viscous of the monomers, and so this will be the least accurate measurement. This is why we wait to measure the mass of the other monomers.
 - This can usually be poured out of the bottle, but you may want to use a stir rod to better control the stringy, viscous flow when you are ready to stop pouring.
 - Try to avoid getting this on the side of the beaker, since it will be difficult to stir into the rest of the mixture later in the synthesis.
4. Set the glass beaker aside and measure the calculated mass of HDI into a disposable plastic container using the digital scale.
- HDI is the least viscous of the monomers, with a consistency close to water. HDI reacts with HPED, so we wait until the end to mix these two.
 - This can be poured directly from the bottle, but it will come out very quickly if the bottle is tipped too much and can run down the sides of the bottle if it is tipped too little. A motorized pipette should be used to add the last 1-2 grams of HDI.
 - The pipette will leak HDI quickly, so apply slight suction when transferring liquid to avoid spilling before reaching the scale.
 - When finished with the pipette, dispose of it in the waste container.
5. Set the plastic container aside and place the glass beaker on the scale again. Measure the calculated mass of TEA into the beaker.
- TEA has a viscosity between HPED and HDI. It has a consistency close to that of glycerin.

- TEA can be poured from the bottle, but a pipette should be used for the last 1-2 grams of the monomer to ensure accuracy. Typically, the amount of TEA needed is small, so pouring may not be necessary.
 - TEA is not sucked into the pipette easily. It also does not stay in the pipette very reliably.
6. Take the glass beaker off the scale and set the scale to the side. Bring the stir plate to the middle of the box where you can easily reach it.
 7. Set the glass beaker on the center of the stir plate and place the stir bar into the beaker.
 8. Add the HDI to the HPED and TEA in the glass beaker and begin stirring the mixture slowly.
 - Since the HPED is so viscous, the stir bar will take a while to really begin moving. Don't crank the speed all the way up right off the bat because once the bar starts moving it will splash everywhere.
 - Try to avoid turbulence in your mixture as much as possible. This mixes gas bubbles into the SMP.
 9. Start a timer and wait for the mixture to become completely clear.
 - This transition happens after a pretty regular amount of time for each composition, so you can use the timer to confirm that things are proceeding correctly.
 10. When the mixture becomes clear, stop stirring and remove the stir bar. The SMP is now ready to pour into the prepared container or mold.

A1.3 Casting a solid sugar block

1. Select sugar with a desirable grain size.
2. Measure an appropriate amount of sugar for filling your molds. For the large, square blocks (1.5 x 1.5 x 0.4 in.) used in Chapter 4, 20g per block is appropriate.
3. Use a spray bottle filled with water to lightly wet a small spatula and stir the moisture into the sugar.
4. Repeat Step 3, adding small increments of moisture to the sugar until it takes on a crumbly texture and holds its shape (**Fig. A1.2**) when scooped with the spatula.



Figure A1.2: Example of proper sugar crystal texture and adhesion.

5. Place the silicone molds onto a flat aluminum plate and add the sugar, packing it tightly with the back of the spatula.
6. When the molds have been filled slightly above the top of the silicone, place another aluminum plate on top of the molds and place the sandwich into a compressor.
7. Apply pressure until the plates are no longer able to move, and then apply slightly more. Leave the plates under pressure for roughly one minute.

8. Remove the plates from the compressor and remove the top plate from the molds. Test the sugar to make sure it is properly compacted by lifting one edge of each silicone mold and observing whether the sugar inside moves or stays in place. If the sugar stays in place, the molds are clear to move onward to baking.
9. Pre-heat an oven to 130 °C and then add the silicone molds and sugar on a small aluminum plate.
10. Bake the blocks for exactly one hour, then retrieve them from the oven and allow to cool.
11. Gently remove the sugar blocks from their molds, attempting to preserve definition on the edges as much as possible. **Fig. A1.3** shows a well-preserved block.



Figure A1.3: Finished sugar block

12. If not used immediately, store the cubes by wrapping them in paper towels and placing in a dry area away from humidity or any sources of moisture. (Fume hood in a Ziplock bag is a good option).

A1.4 Solid SMP Casting (For thermo-mechanical testing)

1. Once the appropriate amount of SMP has been synthesized, pour the clear mixture into the silicone beam or dog bone molds.

2. Place the molds into the vacuum oven and vacuum to at least -0.8 torr and hold the vacuum for 3 minutes.
3. Purge using nitrogen gas back down to -0.1 torr and hold for 1 minute.
4. Repeat Steps 2 and 3 for five cycles to remove gas bubbles from SMP. The importance of this step is illustrated in **Fig. A1.4**.
 - We refer to these steps as the “degassing procedure.”

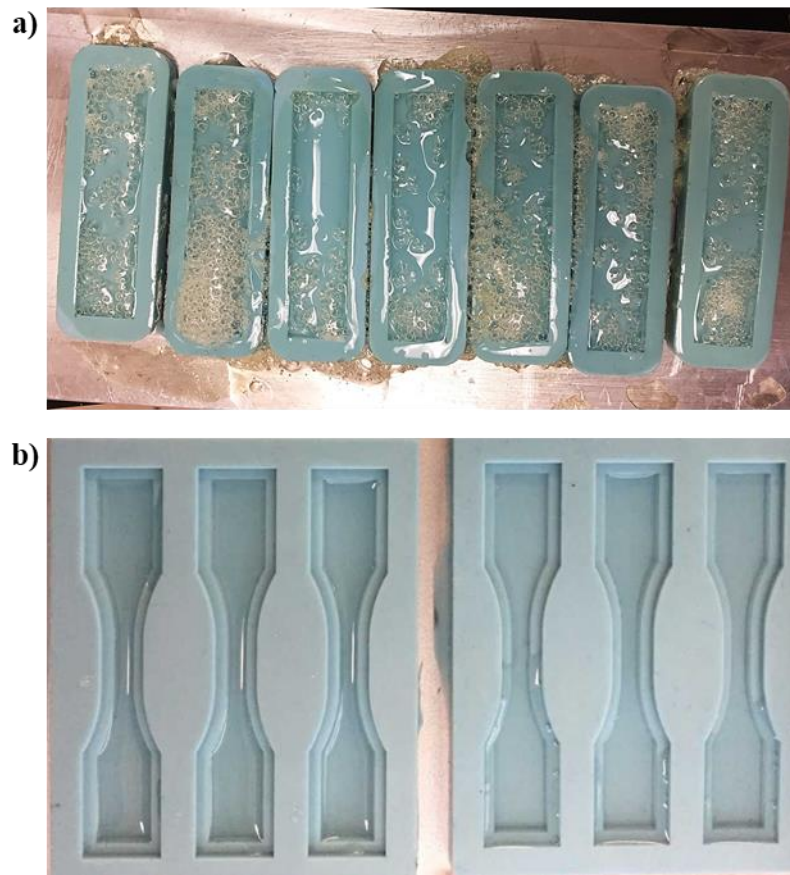


Figure A1.4: a) Beam specimens synthesized without the degassing procedure b) Dog bone specimens synthesized using the degassing procedure.

5. Hold the vacuum at -0.1 torr and heat according to the following heating protocol:
 - Remain at room temperature for 1 hour.

- Heat from room temperature to 130 °C according to the constant heating rate in the composition table.
 - Remain at 130 °C for 1 hour.
6. During heating, gasses will expand and reduce the vacuum seal in the oven. Return to the lab and restore the vacuum to -0.1 torr for every increase of 10 °C. The time between resealing can be calculated using the heating rate.
 7. At the end of the baking process, the SMP samples should be fully cured. Store them in a sealed container away from moisture.

A1.5 SMP Foam Casting (Sugar Block)

1. Prepare a sugar block by placing it in a plastic weigh boat, sitting flat on the bottom and lined up as accurately as possible to be parallel with the sides of the container
2. For a single sugar block, roughly 25 g of SMP is needed.
3. Once an appropriate amount of the desired SMP composition has been mixed, pour the clear mixture over the sugar block in the weigh boat. The mixture should be enough to cover the top of the block.
4. Place the weigh boat in a vacuum food container and establish a vacuum seal. Place the container in the freezer for 24 hours to allow the SMP to completely penetrate the sugar block.
5. Remove the container from the freezer and heat to 40 °C (still under vacuum) until the SMP block is solid. The block should look like those shown in **Fig. A1.5**.
 - Skip this step, if the SMP block is already solid at room temperature.



Figure A1.5: Cured SMP cast around a sugar scaffold in the shape of a weigh boat

6. When the SMP is solid, you should be able to easily peel off the weigh boat from the SMP block. When the weigh boat is removed, place the SMP block into a programmable oven and bake according to the following heating procedure:
 - Pre-heat the oven to 70 °C.
 - Place the SMP block in the oven and bake at 70 °C for 1 hour
 - With SMP still in the oven, heat to 130 °C.
 - Bake at 130 °C for 1 hour.
7. When the SMP has cooled from baking, use a band saw to cut away all excess SMP material and leave only the sugar block (**Fig. A1.6**).
 - It is recommended to use a back light to locate and mark the edges of the sugar for cutting.
 - It is better to remove a little excess sugar than to leave non-foam SMP on the outside of the block.



Figure A1.6: Same SMP blocks from **Fig. A1.5** with all excess polymer trimmed away.

8. Place the sugar block into a sealed container filled with water and place in a heated water bath at 40 °C to dissolve the sugar.
 - Change the water every 2 hours if possible to promote quicker dissolution.
9. Continue dissolving sugar until SMP becomes uniformly colored. If the foam has uneven coloring (**Fig. A1.7**), more dissolving time is needed. The ideal time for completely dissolving sugar is uncertain, but synthesis procedures performed using a 24-hour dissolving period have produced good results.



Figure A1.7: Same SMP block from **Fig. A1.6** showing partial sugar dissolution. Note that the dark shading in the center indicates the presence of remaining sugar.

10. Place SMP foam (now filled with water) in an oven on a small plate. Bake at 60 °C under a nitrogen atmosphere until all water is evaporated from specimen.

- It is easily discernable when the specimen is dried by taking it out at 1-hour intervals and recording mass. When the mass stops changing, the sample is dry.

11. Once dry, the SMP foam should be ready for use. Store in a sealed container away from moisture.

A1.6 SMP Foam Casting (Loose Sugar)

1. Begin by selecting a Sugar-to-SMP ratio that you want to use for the foam synthesis.

- This value can vary, and we're still not sure what is optimal. Various Sugar-to-SMP ratios are shown in **Figure A1.8**.
- A 4:1 ratio is typically used for medium particles (400-500 μ m) and a 3:1 ratio for large particles (1250-1500 μ m).

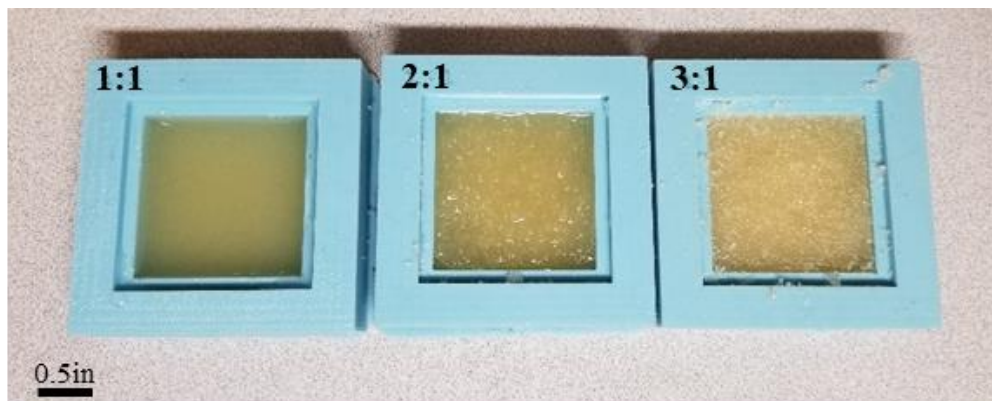


Figure A1.8: SMP molds filled with varying Sugar-to-SMP ratios.

2. The large, square molds used in the foam casting procedures that utilize the sugar block hold roughly 20g each. Divide the 20g according to your selected Sugar-to-SMP ratio.
 - For example, a 3:1 ratio would be 15g sugar and 5g SMP.
3. Synthesize the corresponding amount of SMP using the SMP synthesis procedures described above.
4. Add the sugar to a glass beaker, using a digital scale to confirm the weight.
5. Add the liquid SMP to the same beaker, using a digital scale to confirm the weight.
6. Mix the SMP and sugar thoroughly using a spatula.
7. Transfer the mixture to the square silicone mold and use the flat end of the spatula to pack the mixture tightly (**Fig. A1.9**).
 - Pay special attention to the sides and corners of the mold, since these areas tend to resist packing.

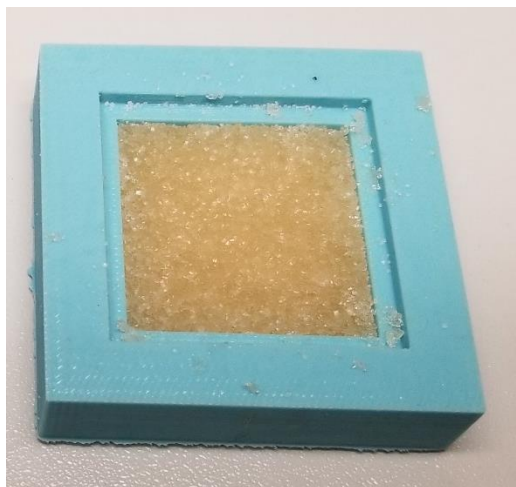


Figure A1.9: Well-packed sugar/SMP mixture in a 1.5 x 1.5 x 0.4 in. mold.

8. Place the mold into the oven and heat according to the heating curve used in solid SMP synthesis.

9. When finished curing, remove the SMP and sugar block from the mold and submerge in distilled water at 80 °C for 12 hours, changing the water every 2 hours if possible.
 - The water changes are important, since the water can easily become saturated and reduce the effectiveness of the dissolution.
10. Dry foam samples in a vacuum oven under a nitrogen environment at 50 °C for 24 hours, opening the oven every 4 hours if possible to remove condensation and re-establish the vacuum seal.
11. Store samples under a vacuum seal or in a moisture-free environment (such as a desiccator) to prevent moisture uptake from the atmosphere.

Appendix 2: Standard Operating Procedures for Prototype

SMP 3D Printer

A2.1 Preparing the 3D Printer



The 3D printer's power button is located on the back of the control box. Interactions with the printer come through a small screen on the control box and a dual button/dial that can be pressed in to select items and spun to scroll.

Caution: The printer's button will often select the wrong item, even when you think you have selected the right option. To minimize this, press directly in the center of the button.

Leveling the Bed

Mount a blue 22-gauge (inner diameter = 0.41 mm) needle onto the printer. It is imperative that this particular needle is used for leveling, since all needles, while within manufacturing tolerances, are slightly different lengths.

1. Screw the 22-gauge needle into a Luer lock adapter.
2. Push the Luer lock adapter into the needle holder. The fit should be tight; removing the adapter by hand should be very difficult. This ensures that the needle does not shift while printing.
3. Use an Allen wrench to attach the needle holder to the printer. The bolts used to do so will keep the Luer lock and needle still during the print, even if the fit between it and the needle holder is not perfectly tight.

On the printer, select  > **Prepare > Auto home**. This will move the printhead to its home position. Next, disable the stepper motors so the print bed can be manually moved ( > **Prepare > Disable steppers**).

Slide a piece of paper underneath the needle. Adjust the leveling screws underneath the print bed until the needle just scratches the paper. Turning the screws counterclockwise from above, corresponding to tightening the screws, lowers the bed. At a minimum, perform bed leveling at all four corners and the center of the bed. Remove the paper and verify that the needle does not catch anywhere on the bed by moving the printhead back and forth. If the bed has not been levelled in a while or if the screws have been turned significantly since the last bed levelling, check every corner multiple times to ensure proper levelling.

Heating the Bed

○ > **Control** > **Temperature** > **Bed**. Scroll to the desired temperature and click the dial again. Returning to the home screen, the bed temperature setpoint should be shown at the top of the screen. It is important to do this at least 15 minutes before starting a print to allow the top surface of the bed reaches its maximum temperature.

Caution: The print bed gets extremely hot. Use heat gloves when working with the heated print bed.

Loading and Verifying the G-Code

It is a good idea to verify that the G-code is doing what you would expect before beginning the print with the SMP.

1. Insert the SD card into the slot on the side of the printer (**Fig. A2.1**).



Figure A2.1: Location of the SD card slot on the printer control box.

2. ○ > **Print from SD**; scroll to find the file.
3. Click the button to start the print.
4. Once you have observed that the printhead is making the correct movements, abort the print by selecting ○ > **Stop print**.
5. It is important that the needle is not in contact with the heated print bed. Once you have stopped the print, lift the needle off the bed (50 mm is a fine distance) by selecting ○ > **Prepare > Move axis > Move Z**.

Caution: Due to the button's tendency to select the wrong file, always make sure to verify that the right print is running by checking the name displayed on the home screen during the print.

A2.2 Preparing the LVE

Setting up the LVE is relatively simple, but crucial to proper operation of the device.

LVE Geometry

Below are CAD images of the LVE (**Fig A2.2** and **Fig A2.3**).

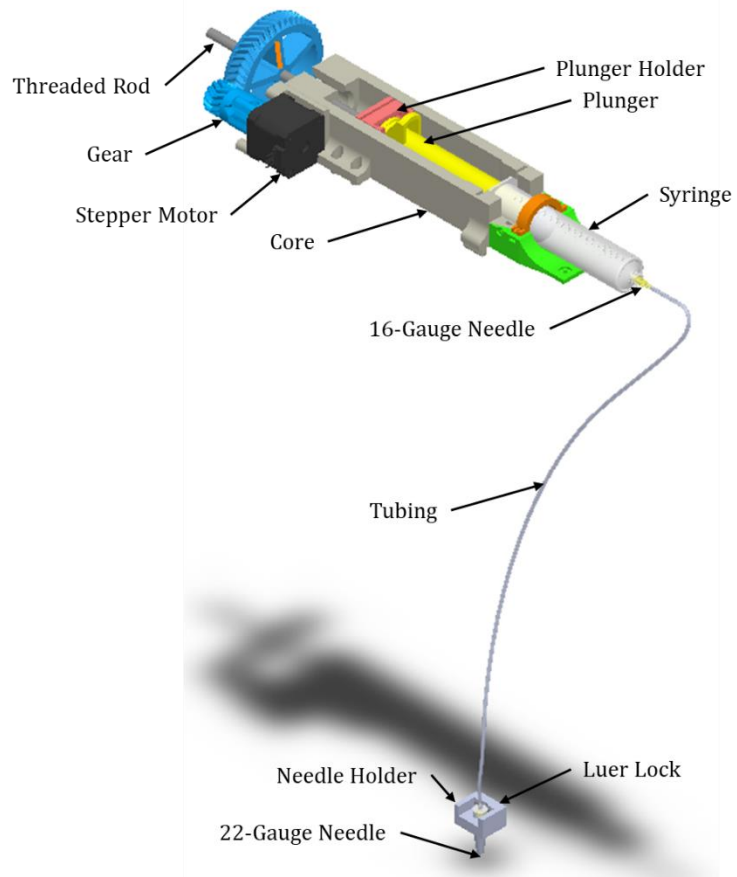
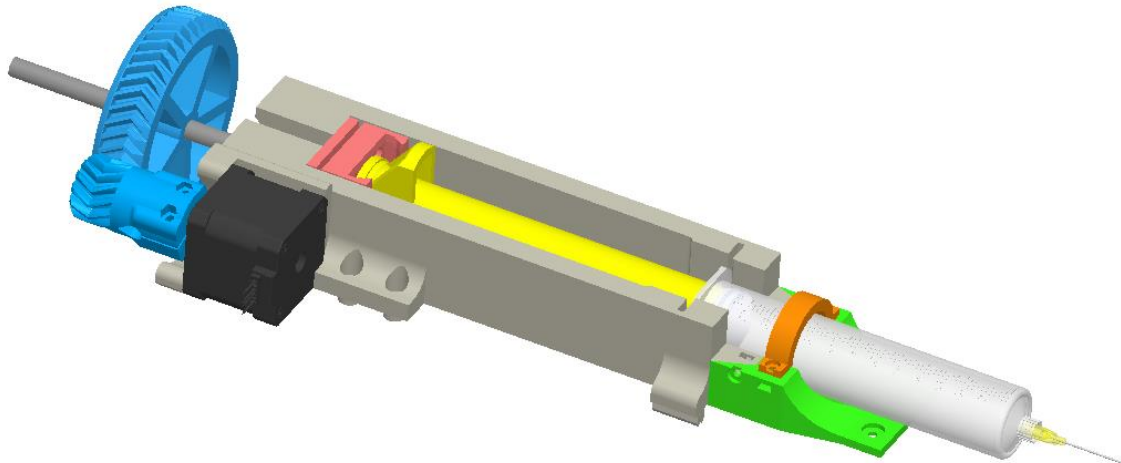
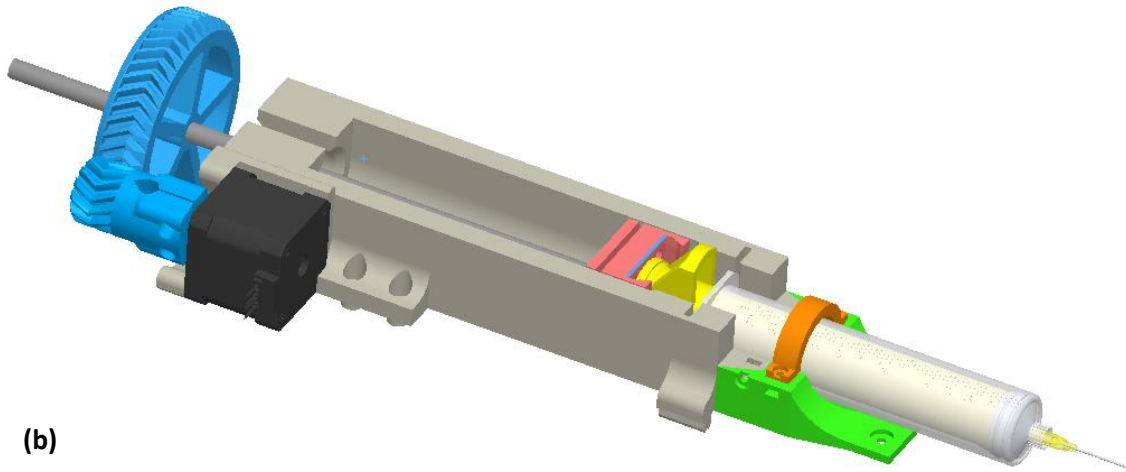


Figure A2.2: 3D model of the full LVE system.



(a)



(b)

Figure A2.3: LVE system (a) fully retracted and (b) fully extended.

Assembly

1. Open a new syringe.
2. Remove the plunger.
3. Place the rubber plunger tip on the LVE's plunger.
4. Screw a gray 16-gauge needle onto the tip of the syringe.

5. Cut an appropriate length of tubing off the roll. Appropriate indicates that the line can comfortably reach any point to which the printhead may travel (roughly 20-25 inches).
6. Force the tubing onto the 16-gauge needle.

For now, leave the plunger outside the syringe. It will be inserted after SMP is poured into the syringe in the next step. Finally, note that the other end of the tubing will be forced onto the Luer lock adapter in the final installation of the LVE.

A2.3 SMP Synthesis

Caution: Do not synthesize more than around 5-7 grams of SMP. Making more will cause the material to cure within the syringe in less than an hour, making it difficult to complete print tests.

Follow the instructions in Appendix A1.1 and Appendix A1.2 to prepare a liquid SMP mixture. For use in printing applications, the needle and syringe are placed inside the glove box. This allows the extrusion reservoir to be filled under a nitrogen environment, limiting bubble formation in the printing line. Gently pour the SMP into the syringe and insert the plunger. Advance the plunger until SMP barely begins to enter the tubing at the syringe tip.

A2.4 Printing

Loading the LVE

1. ○ > **Prepare > Motion > Move axis > Move Z** to lift the needle. This keeps SMP from curing in the needle by ensuring it is not in contact with the bed when SMP is forced through the line.

2. Rotate the threaded rod so the plunger holder is at the proper position for loading the syringe.
3. Insert the syringe into the holder, making sure to lock the plunger into the plunger holder on the threaded rod (see LVE Geometry above).
4. Attach the tubing to the Luer lock adapter that is already inside the needle mount.
5. Spin the gear until SMP travels through the entire line and just begins to slowly drip from the needle.

Caution: Make sure that there are no bubbles in the line or syringe before starting the print. Additionally, ensure that the LVE system is not placed directly above the printer, as this leads to premature curing of the material.

Starting the Print

○ > **Print from SD**. Click **Refresh** if necessary. Select your file and click the dial.

If the bed has not been heated to the proper temperature (see **Error! Reference source not found.**), the printer's screen will say *Bed heating* until the desired temperature is reached. Once this occurs, the print will start, and the name of the print will be displayed on the screen.

Verifying Proper Printing

Verification of printing is done in two ways: observing the print and ensuring that the parameters displayed on the control box are correct. First, the printing of the skirt lines should be observed to ensure the extrusion pressure has been made consistent. This will be apparent by an even extrusion line which closely resembles the needle inner diameter. After the skirt lines, the print should be further observed to ensure there are no gaps in the print or areas of significant over-extrusion (globes on the print bed). Second, the printing

parameters can be verified on the printer control box, namely that the printing file name is correct. If for any reason the print is not performing correctly, abort the print using the control box (○ > **Stop Print**).

Caution: SMP will cure in the needle if it remains in contact with the heated plate for too long. Minimize this by lifting the needle whenever possible (○ > **Prepare** > **Move axis** > **Move Z**).

A2.5 Removing the Print

Once the print has finished, it can be removed with a razor blade. Removing a print can be a long process; just be patient and you will get the prints off the print bed without any problem.

Typically, we allow the bed to cool until it is safe to touch before removing the print. The print is more likely to stay intact at lower temperatures, and accidental burns are less likely. Be careful around the heated bed and do not leverage the still-pliable print too much. Alternatively, you can leave the previous print on the bed and print in a different area, but remember that it may begin to degrade (**Fig. A2.4**) if exposed to heat for too long.

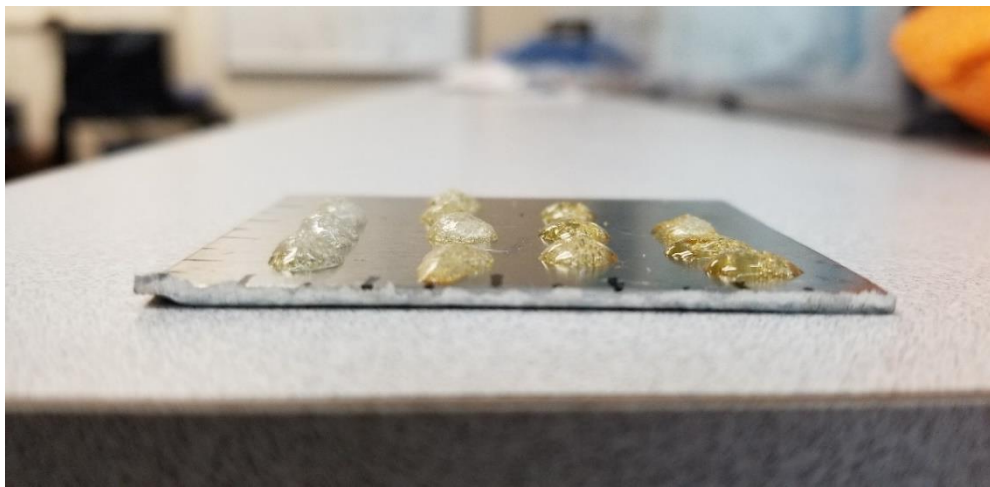


Figure A2.4: Degraded SMP with a distinctive amber tint.

Caution: The razor blade heats up rapidly when in contact with the bed. Avoid burns by wearing the heat gloves.

While removing the print, start at the thickest part of the print. Keep the razor blade as horizontal as possible and avoid lifting up on the print as much as possible to avoid bending and possibly tearing the print. Instead, slowly slide the razor blade under the print, and wiggle it back and forth or use a gentle ramming motion to work the blade further underneath the print until it is free.

A2.6 Preparing for Another Print

If you plan on printing another part immediately after a previous print, remember to immediately turn the heated bed back on (○ > **Control** > **Temperature** > **Bed**) and lift the needle (○ > **Prepare** > **Move axis** > **Move Z**). The heated bed shuts off automatically at the end of any print, including aborted prints.

Printer Cleaning

A razor blade can be used to remove cured SMP from the glass bed. It is easiest to remove the excess cured SMP by first heating the bed slightly (about 70 °C) and then removing the SMP with the razor blade. Further cleaning of the print bed can be performed at a lower temperature by using paper towels and ethanol, carefully scrubbing the surface.

References

1. Yang, S., Leong, K.-F., Du, Z., and Chua, C.-K., *The design of scaffolds for use in tissue engineering. Part i. Traditional factors*. Tissue Engineering, 2001. **7**(6): pp. 679-689.
2. Guan, J., Fujimoto, K.L., Sacks, M.S., and Wagner, W.R., *Preparation and characterization of highly porous, biodegradable polyurethane scaffolds for soft tissue applications*. Biomaterials, 2005. **26**(18): pp. 3961-3971.
3. De Nardo, L., Bertoldi, S., Cigada, A., Tanzi, M.C., Haugen, H.J., and Farè, S., *Preparation and characterization of shape memory polymer scaffolds via solvent casting/particulate leaching*. Journal of Applied Biomaterials & Functional Materials, 2012. **10**(2): pp. 119-126.
4. Metzger, M.F., Wilson, T.S., Schumann, D., Matthews, D.L., and Maitland, D.J., *Mechanical properties of mechanical actuator for treating ischemic stroke*. Biomedical Microdevices, 2002. **4**(2): pp. 89-96.
5. Small, W., Wilson, T.S., Buckley, P.R., Benett, W.J., Loge, J.M., Hartman, J., and Maitland, D.J., *Prototype fabrication and preliminary in vitro testing of a shape memory endovascular thrombectomy device*. IEEE Transactions on Biomedical Engineering, 2007. **54**(9): pp. 1657-1666.
6. Wiebers, D.O. and Investigators, I.S.o.U.I.A., *Unruptured intracranial aneurysms: Natural history, clinical outcome, and risks of surgical and endovascular treatment*. The Lancet, 2003. **362**(9378): pp. 103-110.
7. Rinkel, G.J.E., Djibuti, M., Algra, A., and Van Gijn, J., *Prevalence and risk of rupture of intracranial aneurysms: A systematic review*. Stroke, 1998. **29**(1): pp. 251-256.

8. Caranci, F., Briganti, F., Cirillo, L., Leonardi, M., and Muto, M., *Epidemiology and genetics of intracranial aneurysms*. European Journal of Radiology, 2013. **82**(10): pp. 1598-1605.
9. Bederson, J.B., Connolly, E.S., Batjer, H.H., Dacey, R.G., Dion, J.E., Diringer, M.N., Duldner, J.E., Harbaugh, R.E., Patel, A.B., and Rosenwasser, R.H., *Guidelines for the management of aneurysmal subarachnoid hemorrhage a statement for healthcare professionals from a special writing group of the stroke council, american heart association*. Stroke, 2009. **40**(3): pp. 994-1025.
10. Connolly, E.S., Rabinstein, A.A., Carhuapoma, J.R., Derdeyn, C.P., Dion, J., Higashida, R.T., Hoh, B.L., Kirkness, C.J., Naidech, A.M., and Ogilvy, C.S., *Guidelines for the management of aneurysmal subarachnoid hemorrhage: A guideline for healthcare professionals from the american heart association/american stroke association*. Stroke, 2012. **43**(6): pp. 1711-1737.
11. Etminan, N. and Rinkel, G.J., *Unruptured intracranial aneurysms: Development, rupture and preventive management*. Nature Reviews Neurology, 2016. **12**(12): p. 699.
12. Meng, H., Tutino, V.M., Xiang, J., and Siddiqui, A., *High wss or low wss? Complex interactions of hemodynamics with intracranial aneurysm initiation, growth, and rupture: Toward a unifying hypothesis*. American Journal of Neuroradiology, 2014. **35**(7): pp. 1254-1262.
13. Zhou, S., Dion, P.A., and Rouleau, G.A., *Genetics of intracranial aneurysms*. Stroke, 2018. **49**(3): pp. 780-787.
14. Kissela, B.M., Sauerbeck, L., Woo, D., Khoury, J., Carrozzella, J., Pancioli, A., Jauch, E., Moomaw, C.J., Shukla, R., Gebel, J., Fontaine, R., and Broderick, J., *Subarachnoid hemorrhage*. Stroke, 2002. **33**(5): pp. 1321-1326.
15. Hassane, S., Claij, N., Leeuwen, I.S.L.-v., Munsteren, J.C.V., Lent, N.V., Hanemaaijer, R., Breuning, M.H., Peters, D.J.M., and DeRuiter, M.C., *Pathogenic*

- sequence for dissecting aneurysm formation in a hypomorphic polycystic kidney disease 1 mouse model. Arteriosclerosis, Thrombosis, and Vascular Biology, 2007. 27(10): pp. 2177-2183.*
16. Turjman, A.S., Turjman, F., and Edelman, E.R., *Role of fluid dynamics and inflammation in intracranial aneurysm formation. Circulation, 2014. 129(3): pp. 373-382.*
 17. Kulcsár, Z., Ugron, Á., Marosfői, M., Berentei, Z., Paál, G., and Szikora, I., *Hemodynamics of cerebral aneurysm initiation: The role of wall shear stress and spatial wall shear stress gradient. American Journal of Neuroradiology, 2011. 32(3): pp. 587-594.*
 18. Thompson, B.G., Brown, R.D., Amin-Hanjani, S., Broderick, J.P., Cockcroft, K.M., Connolly, E.S., Duckwiler, G.R., Harris, C.C., Howard, V.J., Johnston, S.C., Meyers, P.M., Molyneux, A., Ogilvy, C.S., Ringer, A.J., and Torner, J., *Guidelines for the management of patients with unruptured intracranial aneurysms. Stroke, 2015. 46(8): pp. 2368-2400.*
 19. Lai, L.T. and O'Neill, A.H., *History, evolution, and continuing innovations of intracranial aneurysm surgery. World Neurosurgery, 2017. 102: pp. 673-681.*
 20. Pai, B.S. and Muralimohan, S., *Intraoperative angiography in aneurysm surgery: An initial experience. Neurology India, 2010. 58(4): p. 571.*
 21. Molyneux, A. and Group, I.S.A.T.C., *International subarachnoid aneurysm trial (isat) of neurosurgical clipping versus endovascular coiling in 2143 patients with ruptured intracranial aneurysms: A randomised trial. Lancet, 2002. 360(9342): pp. 1267-1274.*
 22. Horowitz, M.B., Levy, E., Kassam, A., and Purdy, P.D., *Endovascular therapy for intracranial aneurysms: A historical and present status review. Surgical Neurology, 2002. 57(3): pp. 147-158.*

23. Raymond, J., Guilbert, F., Weill, A., Georganos, S.A., Juravsky, L., Lambert, A., Lamoureux, J., Chagnon, M., and Roy, D., *Long-term angiographic recurrences after selective endovascular treatment of aneurysms with detachable coils*. *Stroke*, 2003. **34**(6): pp. 1398-1403.
24. Mascitelli, J.R., Moyle, H., Oermann, E.K., Polykarpou, M.F., Patel, A.A., Doshi, A.H., Gologorsky, Y., Bederson, J.B., and Patel, A.B., *An update to the raymond–roy occlusion classification of intracranial aneurysms treated with coil embolization*. *Journal of Neurointerventional Surgery*, 2014: p. neurintsurg-2014-011258.
25. Cloft, H.J. and Kallmes, D.F., *Aneurysm packing with hydrocoil embolic system versus platinum coils: Initial clinical experience*. *American Journal of Neuroradiology*, 2004. **25**(1): pp. 60-62.
26. Leng, B., Zheng, Y., Ren, J., Xu, Q., Tian, Y., and Xu, F., *Endovascular treatment of intracranial aneurysms with detachable coils: Correlation between aneurysm volume, packing, and angiographic recurrence*. *Journal of NeuroInterventional Surgery*, 2014. **6**(8): pp. 595-599.
27. Hu, J., *1 - Introduction*, in *Shape memory polymers and textiles*, J. Hu, Editor. 2007, Woodhead Publishing. pp. 1-27.
28. Hu, J., *2 - Preparation of Shape Memory Polymers*, in *Shape memory polymers and textiles*, J. Hu, Editor. 2007, Woodhead Publishing. pp. 28-61.
29. Xie, T., *Tunable polymer multi-shape memory effect*. *Nature*, 2010. **464**: p. 267.
30. Singhal, P., Rodriguez, J.N., Small, W., Eagleston, S., Van de Water, J., Maitland, D.J., and Wilson, T.S., *Ultra low density and highly crosslinked biocompatible shape memory polyurethane foams*. *Journal of Polymer Science Part B: Polymer Physics*, 2012. **50**(10): pp. 724-737.
31. Janik, H. and Marzec, M., *A review: Fabrication of porous polyurethane scaffolds*. *Materials Science and Engineering: C*, 2015. **48**: pp. 586-591.

32. Kim, J. and Hollinger, J.O., *Recombinant human bone morphogenetic protein-2 released from polyurethane-based scaffolds promotes early osteogenic differentiation of human mesenchymal stem cells*. *Biomedical Materials*, 2012. **7**(4): p. 045008.
33. Gorna, K. and Gogolewski, S., *Preparation, degradation, and calcification of biodegradable polyurethane foams for bone graft substitutes*. *Journal of Biomedical Materials Research Part A*, 2003. **67A**(3): pp. 813-827.
34. De Nardo, L., Bertoldi, S., Tanzi, M.C., Haugen, H., and Fare, S., *Shape memory polymer cellular solid design for medical applications*. *Smart Materials and Structures*, 2011. **20**(3): p. 035004.
35. Rodriguez, J.N., Clubb, F.J., Wilson, T.S., Miller, M.W., Fossum, T.W., Hartman, J., Tuzun, E., Singhal, P., and Maitland, D.J., *In vivo response to an implanted shape memory polyurethane foam in a porcine aneurysm model*. *Journal of Biomedical Materials Research Part A*, 2014. **102**(5): pp. 1231-1242.
36. Metcalfe, A., Desfaits, A.-C., Salazkin, I., Yahia, L.H., Sokolowski, W.M., and Raymond, J., *Cold hibernated elastic memory foams for endovascular interventions*. *Biomaterials*, 2003. **24**(3): pp. 491-497.
37. Zdrahala, R.J. and Zdrahala, I.J., *Biomedical applications of polyurethanes: A review of past promises, present realities, and a vibrant future*. *Journal of Biomaterials Applications*, 1999. **14**(1): pp. 67-90.
38. Yang, C.-S., Wu, H.-C., Sun, J.-S., Hsiao, H.-M., and Wang, T.-W., *Thermo-induced shape-memory peg-pcl copolymer as a dual-drug-eluting biodegradable stent*. *ACS Applied Materials & Interfaces*, 2013. **5**(21): pp. 10985-10994.
39. Wischke, C. and Lendlein, A., *Shape-memory polymers as drug carriers—a multifunctional system*. *Pharmaceutical Research*, 2010. **27**(4): pp. 527-529.

40. Ge, Q., Sakhaei, A.H., Lee, H., Dunn, C.K., Fang, N.X., and Dunn, M.L., *Multimaterial 4d printing with tailorable shape memory polymers*. Scientific Reports, 2016. **6**: p. 31110.
41. Fattori, R. and Piva, T., *Drug-eluting stents in vascular intervention*. The Lancet, 2003. **361**(9353): pp. 247-249.
42. Xue, L., Dai, S., and Li, Z., *Synthesis and characterization of elastic star shape-memory polymers as self-expandable drug-eluting stents*. Journal of Materials Chemistry, 2012. **22**(15): pp. 7403-7411.
43. Beecher, J.S. and Welch, B.G., *Chapter 156 - Surgical and Endovascular Management of Patients with Giant Cerebral Aneurysms*, in *Primer on cerebrovascular diseases (second edition)*, L.R. Caplan, et al., Editors. 2017, Academic Press: San Diego. pp. 818-823.
44. Wehman, J.C., Hanel, R.A., Levy, E.I., and Hopkins, L.N., *Giant cerebral aneurysms: Endovascular challenges*. Neurosurgery, 2006. **59**(5): pp. S3-125.
45. Boyle, A.J., Wierzbicki, M.A., Herting, S., Weems, A.C., Nathan, A., Hwang, W., and Maitland, D.J., *In vitro performance of a shape memory polymer foam-coated coil embolization device*. Medical Engineering & Physics, 2017. **49**: pp. 56-62.
46. Boyle, A.J., Landsman, T.L., Wierzbicki, M.A., Nash, L.D., Hwang, W., Miller, M.W., Tuzun, E., Hasan, S.M., and Maitland, D.J., *In vitro and in vivo evaluation of a shape memory polymer foam-over-wire embolization device delivered in saccular aneurysm models*. Journal of Biomedical Materials Research Part B: Applied Biomaterials, 2016. **104**(7): pp. 1407-1415.
47. Maitland, D.J., Small, W., Ortega, J.M., Buckley, P.R., Rodriguez, J., Hartman, J., and Wilson, T.S., *Prototype laser-activated shape memory polymer foam device for embolic treatment of aneurysms*. Journal of Biomedical Optics, 2007. **12**(3): pp. 030504-030504-030503.

48. Hwang, W., Singhal, P., Miller, M.W., and Maitland, D.J., *In vitro study of transcatheter delivery of a shape memory polymer foam embolic device for treating cerebral aneurysms*. Journal of Medical Devices, 2013. **7**(2): pp. 020932-020932-020932.
49. Schievink, W.I., *Intracranial aneurysms*. New Engl J Med, 1997. **336**(1): pp. 28-40.
50. Rinkel, G.J., Djibuti, M., Algra, A., and Van Gijn, J., *Prevalence and risk of rupture of intracranial aneurysms*. Stroke, 1998. **29**(1): pp. 251-256.
51. King Jr, J.T., *Epidemiology of aneurysmal subarachnoid hemorrhage*. Neuroimaging Clinics of North America, 1997. **7**(4): p. 659.
52. Sacco, R.L., Wolf, P.A., Bharucha, N.E., Meeks, S.L., Kannel, W.B., Charette, L.J., McNamara, P.M., Palmer, E.P., and D'Agostino, R., *Subarachnoid and intracerebral hemorrhage natural history, prognosis, and precursive factors in the framingham study*. Neurology, 1984. **34**(7): pp. 847-847.
53. Naval, N.S., Chang, T., Caserta, F., Kowalski, R.G., Carhuapoma, J.R., and Tamargo, R.J., *Impact of pattern of admission on outcomes after aneurysmal subarachnoid hemorrhage*. Journal of Critical Care, 2012. **27**(5): p. 532. e531-532. e537.
54. Lantigua, H., Ortega-Gutierrez, S., Schmidt, J.M., Lee, K., Badjatia, N., Agarwal, S., Claassen, J., Connolly, E.S., and Mayer, S.A., *Subarachnoid hemorrhage: Who dies, and why?* Critical Care, 2015. **19**(1): p. 309.
55. Wardlaw, J. and White, P., *The detection and management of unruptured intracranial aneurysms*. Brain, 2000. **123**(2): pp. 205-221.
56. Molyneux, A.J., Kerr, R.S., Yu, L.-M., Clarke, M., Sneade, M., Yarnold, J.A., Sandercock, P., and Group, I.S.A.T.C., *International subarachnoid aneurysm trial (isat) of neurosurgical clipping versus endovascular coiling in 2143 patients with ruptured intracranial aneurysms: A randomised comparison of effects on survival,*

- dependency, seizures, rebleeding, subgroups, and aneurysm occlusion. The Lancet, 2005. 366(9488): pp. 809-817.*
57. Guglielmi, G., Viñuela, F., Dion, J., and Duckwiler, G., *Electrothrombosis of saccular aneurysms via endovascular approach: Part 2: Preliminary clinical experience. J Neurosurg, 1991. 75(1): pp. 8-14.*
 58. Campi, A., Ramzi, N., Molyneux, A.J., Summers, P.E., Kerr, R.S., Sneade, M., Yarnold, J.A., Rischmiller, J., and Byrne, J.V., *Retreatment of ruptured cerebral aneurysms in patients randomized by coiling or clipping in the international subarachnoid aneurysm trial (isat). Stroke, 2007. 38(5): pp. 1538-1544.*
 59. Molyneux, A.J., Kerr, R.S., Birks, J., Ramzi, N., Yarnold, J., Sneade, M., Rischmiller, J., and collaborators, I., *Risk of recurrent subarachnoid haemorrhage, death, or dependence and standardised mortality ratios after clipping or coiling of an intracranial aneurysm in the international subarachnoid aneurysm trial (isat): Long-term follow-up. The Lancet Neurology, 2009. 8(5): pp. 427-433.*
 60. Taha, M.M., Nakahara, I., Higashi, T., Iwamuro, Y., Iwaasa, M., Watanabe, Y., Tsunetoshi, K., and Munemitsu, T., *Endovascular embolization vs surgical clipping in treatment of cerebral aneurysms: Morbidity and mortality with short-term outcome. Surgical Neurology, 2006. 66(3): pp. 277-284.*
 61. Hope, J.A., Byrne, J.V., and Molyneux, A.J., *Factors influencing successful angiographic occlusion of aneurysms treated by coil embolization. American Journal of Neuroradiology, 1999. 20(3): pp. 391-399.*
 62. Tateshima, S., Murayama, Y., Gobin, Y.P., Duckwiler, G.R., Guglielmi, G., and Viñuela, F., *Endovascular treatment of basilar tip aneurysms using guglielmi detachable coils: Anatomic and clinical outcomes in 73 patients from a single institution. Neurosurgery, 2000. 47(6): pp. 1332-1342.*
 63. Vallée, J.-N., Aymard, A., Vicaut, E., Reis, M., and Merland, J.-J., *Endovascular treatment of basilar tip aneurysms with guglielmi detachable coils: Predictors of*

- immediate and long-term results with multivariate analysis—6-year experience.* Radiology, 2003. **226**(3): pp. 867-879.
64. Xu, J., Shi, W., and Pang, W., *Synthesis and shape memory effects of si–o–si cross-linked hybrid polyurethanes.* Polymer, 2006. **47**(1): pp. 457-465.
65. Gunes, I.S., Cao, F., and Jana, S.C., *Effect of thermal expansion on shape memory behavior of polyurethane and its nanocomposites.* Journal of Polymer Science Part B: Polymer Physics, 2008. **46**(14): pp. 1437-1449.
66. Huang, H.-Y.S., Balhouse, B.N., and Huang, S., *Application of simple biomechanical and biochemical tests to heart valve leaflets: Implications for heart valve characterization and tissue engineering.* Proceedings of the Institution of Mechanical Engineers. Part H: Journal of Engineering in Medicine, 2012. **226**(11): pp. 868-876.
67. Lendlein, A. and Langer, R., *Biodegradable, elastic shape-memory polymers for potential biomedical applications.* Science, 2002. **296**(5573): pp. 1673-1676.
68. Maitland, D.J., Metzger, M.F., Schumann, D., Lee, A., and Wilson, T.S., *Photothermal properties of shape memory polymer micro-actuators for treating stroke.* Lasers in Surgery and Medicine, 2002. **30**(1): pp. 1-11.
69. Wache, H., Tartakowska, D., Hentrich, A., and Wagner, M., *Development of a polymer stent with shape memory effect as a drug delivery system.* Journal of Materials Science: Materials in Medicine, 2003. **14**(2): pp. 109-112.
70. Wilson, T., Bearinger, J., Herberg, J., Marion, J., Wright, W., Evans, C., and Maitland, D., *Shape memory polymers based on uniform aliphatic urethane networks.* Journal of Applied Polymer Science, 2007. **106**(1): pp. 540-551.
71. Lin, J. and Chen, L., *Study on shape-memory behavior of polyether-based polyurethanes. I. Influence of the hard-segment content.* Journal of Applied Polymer Science, 1998. **69**(8): pp. 1563-1574.

72. Lin, J. and Chen, L., *Study on shape-memory behavior of polyether-based polyurethanes. Ii. Influence of soft-segment molecular weight*. Journal of Applied Polymer Science, 1998. **69**(8): pp. 1575-1586.
73. Lan, X., Liu, Y., Lv, H., Wang, X., Leng, J., and Du, S., *Fiber reinforced shape-memory polymer composite and its application in a deployable hinge*. Smart Materials and Structures, 2009. **18**(2): p. 024002.
74. Wang, H., Wang, B., Normoyle, K.P., Jackson, K., Spitler, K., Sharrock, M.F., Miller, C.M., Best, C., Llano, D., and Du, R., *Brain temperature and its fundamental properties: A review for clinical neuroscientists*. Frontiers in Neuroscience, 2014. **8**: p. 307.
75. Small, W.I., Singhal, P., Wilson, T.S., and Maitland, D.J., *Biomedical applications of thermally activated shape memory polymers*. Journal Materials Chemistry, 2010. **20**(17): pp. 3356-3366.
76. Lendlein, A., Behl, M., Hiebl, B., and Wischke, C., *Shape-memory polymers as a technology platform for biomedical applications*. Expert Review of Medical Devices, 2010. **7**(3): pp. 357-379.
77. Sun, L., Huang, W.M., Ding, Z., Zhao, Y., Wang, C.C., Purnawali, H., and Tang, C., *Stimulus-responsive shape memory materials: A review*. Materials & Design, 2012. **33**: pp. 577-640.
78. Hu, J., Zhu, Y., Huang, H., and Lu, J., *Recent advances in shape-memory polymers: Structure, mechanism, functionality, modeling and applications*. Progress in Polymer Science, 2012. **37**(12): pp. 1720-1763.
79. Sokolowski, W., Metcalfe, A., Hayashi, S., Yahia, L.H., and Raymond, J., *Medical applications of shape memory polymers*. Biomedical Materials, 2007. **2**(1): p. S23.
80. Leng, J., Lan, X., Liu, Y., and Du, S., *Shape-memory polymers and their composites: Stimulus methods and applications*. Progress in Materials Science, 2011. **56**(7): pp. 1077-1135.

81. Mather, P.T., Luo, X., and Rousseau, I.A., *Shape memory polymer research*. Annual Review of Materials Research, 2009. **39**: pp. 445-471.
82. Tobushi, H., Hara, H., Yamada, E., and Hayashi, S., *Thermomechanical properties in a thin film of shape memory polymer of polyurethane series*. Smart Materials & Structures, 1996. **5**(4): pp. 483-491.
83. Mohr, R., Kratz, K., Weigel, T., Lucka-Gabor, M., Moneke, M., and Lendlein, A., *Initiation of shape-memory effect by inductive heating of magnetic nanoparticles in thermoplastic polymers*. Proceedings of the National Academy of Sciences, 2006. **103**(10): pp. 3540-3545.
84. Lendlein, A., Jiang, H., Jünger, O., and Langer, R., *Light-induced shape-memory polymers*. Nature, 2005. **434**(7035): p. 879.
85. Jiang, H., Kelch, S., and Lendlein, A., *Polymers move in response to light*. Advanced Materials, 2006. **18**(11): pp. 1471-1475.
86. Du, H. and Zhang, J., *Solvent induced shape recovery of shape memory polymer based on chemically cross-linked poly (vinyl alcohol)*. Soft Matter, 2010. **6**(14): pp. 3370-3376.
87. Huang, W., Yang, B., An, L., Li, C., and Chan, Y., *Water-driven programmable polyurethane shape memory polymer: Demonstration and mechanism*. Applied Physics Letters, 2005. **86**(11): p. 114105.
88. Vernon, L.B. and Vernon, H.M., *Process of manufacturing articles of thermoplastic synthetic resins*. 1941, Google Patents.
89. Kim, B.K., Lee, S.Y., and Xu, M., *Polyurethanes having shape memory effects*. Polymer, 1996. **37**(26): pp. 5781-5793.
90. Booth, C.J., Kindinger, M., McKenzie, H.R., Handcock, J., Bray, A.V., and Beall, G.W., *Copolyterephthalates containing tetramethylcyclobutane with impact and ballistic properties greater than bisphenol a polycarbonate*. Polymer, 2006. **47**(18): pp. 6398-6405.

91. Feng, Y., Lu, J., Behl, M., and Lendlein, A., *Degradable depsipeptide-based multiblock copolymers with polyester or polyetherester segments*. The International Journal of Artificial Organs, 2011. **34**(2): pp. 103-109.
92. Sakurai, K., Kashiwagi, T., and Takahashi, T., *Crystal structure of polynorbornene*. Journal of Applied Polymer Science, 1993. **47**(5): pp. 937-940.
93. Sakurai, K., Shirakawa, Y., Kashiwagi, T., and Takahashi, T., *Crystal transformation of styrene-butadiene block copolymer*. Polymer, 1994. **35**(19): pp. 4238-4239.
94. Takahashi, T., Takimoto, J.-i., and Koyama, K., *Uniaxial elongational viscosity of poly (styrene-block-butadiene-block-styrene) melts*. Journal of the Society of Materials Science, 1998. **47**(6Appendix): pp. 97-102.
95. Wang, J., Chowdhury, S., Liu, Y., Bohnstedt, B., and Lee, C.-H. *Development of thermally-activated shape memory polymers and nanocomposites for biomedical devices*. in *ASME 2017 International Mechanical Engineering Congress and Exposition*. 2017. American Society of Mechanical Engineers.
96. Gall, K., Dunn, M.L., Liu, Y.P., Finch, D., Lake, M., and Munshi, N.A., *Shape memory polymer nanocomposites*. Acta Materialia, 2002. **50**(20): pp. 5115-5126.
97. Thakur, S. and Karak, N., *Bio-based tough hyperbranched polyurethane-graphene oxide nanocomposites as advanced shape memory materials*. RSC Advances, 2013. **3**(24): pp. 9476-9482.
98. Liu, C., Qin, H., and Mather, P., *Review of progress in shape-memory polymers*. Journal Materials Chemistry, 2007. **17**(16): pp. 1543-1558.
99. Meng, H. and Li, G.Q., *A review of stimuli-responsive shape memory polymer composites*. Polymer, 2013. **54**(9): pp. 2199-2221.
100. Zhao, Q., Qi, H.J., and Xie, T., *Recent progress in shape memory polymer: New behavior, enabling materials, and mechanistic understanding*. Progress in Polymer Science, 2015. **49-50**: pp. 79-120.

101. Hager, M.D., Bode, S., Weber, C., and Schubert, U.S., *Shape memory polymers: Past, present and future developments*. Progress in Polymer Science, 2015. **49-50**: pp. 3-33.
102. Murayama, Y., Nien, Y.L., Duckwiler, G., Gobin, Y.P., Jahan, R., Frazee, J., Martin, N., and Viñuela, F., *Guglielmi detachable coil embolization of cerebral aneurysms: 11 years' experience*. Journal of Neurosurgery, 2003. **98**(5): pp. 959-966.
103. Molyneux, A.J., Kerr, R.S., Yu, L.-M., Clarke, M., Sneade, M., Yarnold, J.A., Sandercock, P., and Group, I.S.A.T.C., *International subarachnoid aneurysm trial (isat) of neurosurgical clipping versus endovascular coiling in 2143 patients with ruptured intracranial aneurysms: A randomised comparison of effects on survival, dependency, seizures, rebleeding, subgroups, and aneurysm occlusion*. Lancet, 2005. **366**(9488): pp. 809-817.
104. Chalouhi, N., Bovenzi, C.D., Thakkar, V., Dressler, J., Jabbour, P., Starke, R.M., Teufack, S., Gonzalez, L.F., Dalyai, R., and Dumont, A.S., *Long-term catheter angiography after aneurysm coil therapy: Results of 209 patients and predictors of delayed recurrence and retreatment: Clinical article*. Journal of Neurosurgery, 2014. **121**(5): pp. 1102-1106.
105. Mascitelli, J.R., Moyle, H., Oermann, E.K., Polykarpou, M.F., Patel, A.A., Doshi, A.H., Gologorsky, Y., Bederson, J.B., and Patel, A.B., *An update to the raymond-roy occlusion classification of intracranial aneurysms treated with coil embolization*. Journal of Neurointerventional Surgery, 2015. **7**(7): pp. 496-502.
106. Sokolowski, W.M., Chmielewski, A.B., Hayashi, S., and Yamada, T. *Cold hibernated elastic memory (chem) self-deployable structures*. in *Smart Structures and Materials 1999: Electroactive Polymer Actuators and Devices*. 1999. International Society for Optics and Photonics.

107. Di Prima, M., Lesniewski, M., Gall, K., McDowell, D., Sanderson, T., and Campbell, D., *Thermo-mechanical behavior of epoxy shape memory polymer foams*. Smart Materials and Structures, 2007. **16**(6): p. 2330.
108. Kang, S., Lee, S., and Kim, B., *Shape memory polyurethane foams*. Express Polymer Letters, 2012. **6**(1): pp. 63-69.
109. Tobushi, H., Okumura, K., Endo, M., and Hayashi, S., *Thermomechanical properties of polyurethane-shape memory polymer foam*. Journal of Intelligent Material Systems and Structures, 2001. **12**(4): pp. 283-287.
110. Baer, G.M., Small, W., Wilson, T.S., Bennett, W.J., Matthews, D.L., Hartman, J., and Maitland, D.J., *Fabrication and in vitro deployment of a laser-activated shape memory polymer vascular stent*. Biomedical Engineering Online, 2007. **6**(1): p. 43.
111. Kunkel, R., Laurence, D., Wang, J., Robinson, D., Scherrer, J., Wu, Y., Bohnstedt, B., Chien, A., Liu, Y., and Lee, C.-H., *Synthesis and characterization of bio-compatible shape memory polymers with potential applications to endovascular embolization of intracranial aneurysms*. Journal of the Mechanical Behavior of Biomedical Materials, 2018. **88**: pp. 422-430.
112. Yang, B., Huang, W.M., Li, C., and Li, L., *Effects of moisture on the thermomechanical properties of a polyurethane shape memory polymer*. Polymer, 2006. **47**(4): pp. 1348-1356.
113. Zhang, J., Wu, L., Jing, D., and Ding, J., *A comparative study of porous scaffolds with cubic and spherical macropores*. Polymer, 2005. **46**(13): pp. 4979-4985.
114. Gibson, L.J. and Ashby, M.F., *Cellular solids: Structure and properties*. 1999: Cambridge University Press.
115. Kiyatkin, E.A., *Brain temperature homeostasis: Physiological fluctuations and pathological shifts*. Frontiers in Bioscience, 2010. **15**: pp. 73-92.
116. DeMassa, J. *Polyol stabilization and the introduction of a new pur slabstock foam antioxidant*. in *Polyurethanes 2011 Technical Conference*. 2011. Nashville, TN.

117. Stansbury, J.W. and Idacavage, M.J., *3d printing with polymers: Challenges among expanding options and opportunities*. Dental Materials, 2016. **32**(1): pp. 54-64.
118. Yang, S., Leong, K.-F., Du, Z., and Chua, C.-K., *The design of scaffolds for use in tissue engineering. Part ii. Rapid prototyping techniques*. Tissue Engineering, 2002. **8**(1): pp. 1-11.
119. Chang, H.W., Jeong, D.S., Cho, Y.H., Sung, K., Kim, W.S., Lee, Y.T., and Park, P.W., *Tricuspid valve replacement vs. Repair in severe tricuspid regurgitation*. Circulation Journal, 2017. **81**(3): pp. 330-338.
120. Jia, Y., He, H., Geng, Y., Huang, B., and Peng, X., *High through-plane thermal conductivity of polymer based product with vertical alignment of graphite flakes achieved via 3d printing*. Composites Science and Technology, 2017. **145**: pp. 55-61.
121. Skylar-Scott, M.A., Gunasekaran, S., and Lewis, J.A., *Laser-assisted direct ink writing of planar and 3d metal architectures*. Proceedings of the National Academy of Sciences, 2016. **113**(22): pp. 6137-6142.
122. Lewis, J.A., Smay, J.E., Stuecker, J., and Cesarano, J., *Direct ink writing of three-dimensional ceramic structures*. Journal of the American Ceramic Society, 2006. **89**(12): pp. 3599-3609.
123. Lepowsky, E., Muradoglu, M., and Tasoglu, S., *Towards preserving post-printing cell viability and improving the resolution: Past, present, and future of 3d bioprinting theory*. Bioprinting, 2018: p. e00034.
124. Zarek, M., Layani, M., Cooperstein, I., Sachyani, E., Cohn, D., and Magdassi, S., *3d printing of shape memory polymers for flexible electronic devices*. Advanced Materials, 2016. **28**(22): pp. 4449-4454.
125. Yang, Y., Chen, Y., Wei, Y., and Li, Y., *3d printing of shape memory polymer for functional part fabrication*. The International Journal of Advanced Manufacturing Technology, 2016. **84**(9): pp. 2079-2095.

126. Wu, J., Yuan, C., Ding, Z., Isakov, M., Mao, Y., Wang, T., Dunn, M.L., and Qi, H.J., *Multi-shape active composites by 3d printing of digital shape memory polymers*. Scientific Reports, 2016. **6**: p. 24224.
127. Pusch, K., Hinton, T.J., and Feinberg, A.W., *Large volume syringe pump extruder for desktop 3d printers*. HardwareX, 2018. **3**: pp. 49-61.
128. Morrison, C., Macnair, R., MacDonald, C., Wykman, A., Goldie, I., and Grant, M., *In vitro biocompatibility testing of polymers for orthopaedic implants using cultured fibroblasts and osteoblasts*. Biomaterials, 1995. **16**(13): pp. 987-992.
129. Van Meerloo, J., Kaspers, G.J., and Cloos, J., *Cell sensitivity assays: The mtt assay, in Cancer cell culture*. 2011, Springer. pp. 237-245.
130. Yu, Y.-J., Hearon, K., Wilson, T.S., and Maitland, D.J., *The effect of moisture absorption on the physical properties of polyurethane shape memory polymer foams*. Smart Materials and Structures, 2011. **20**(8): p. 085010.
131. Landsman, T.L., Bush, R.L., Glowczwski, A., Horn, J., Jessen, S.L., Ungchusri, E., Diguette, K., Smith, H.R., Hasan, S.M., and Nash, D., *Design and verification of a shape memory polymer peripheral occlusion device*. Journal of the Mechanical Behavior of Biomedical Materials, 2016. **63**: pp. 195-206.
132. Buckley, P.R., McKinley, G.H., Wilson, T.S., Small, W., Bennett, W.J., Bearinger, J.P., McElfresh, M.W., and Maitland, D.J., *Inductively heated shape memory polymer for the magnetic actuation of medical devices*. IEEE Transactions on Biomedical Engineering, 2006. **53**(10): pp. 2075-2083.